Alma Mater Studiorum · Università di Bologna

Scuola di Scienze
Corso di Laurea Magistrale in FISICA
Ind. Fisica Nucleare e Subnucleare

Proposal of a Continuous Read-Out Implementation in the ALICE - TOF Detector

Relatore
Prof.ssa Gilda SCIOLI

Correlatore
Dr. Pietro ANTONIOLI

Candidato
Mattia FANÌ

Sessione II

Anno Accademico 2014/15

Compendio

Il plasma di quark e gluoni (QGP), riprodotto sperimentalmente e osservato per la prima volta all'interno del collisionatore SPS presso il CERN nell'anno 2000, costituisce il quarto stato della materia finora conosciuto.

Si ritiene che tale stato sia presente in natura in condizioni estreme di pressione e/o temperatura come ad esempio all'interno dei nuclei delle stelle di neutroni e che abbia costituito una delle fasi dell'universo primordiale, alcuni microsecondi dopo il Big Bang. Tuttavia, lo stato di QGP è riproducibile in laboratorio mediante esperimenti di collisione di ioni pesanti a energie ultrarelativistiche.

L'esperimento ALICE, situato al CERN, è stato progettato per lo studio di tali collisioni per energie nel centro di massa fino a $\sqrt{s_{\mathrm{NN}}} = 5.5\ TeV$ per coppia di nucleoni, mediante l'utilizzo di tutte le tecniche di rivelazione di particelle finora conosciute. Nella regione di momento intermedia, (fino a 2.5 GeV/c per π/K e 4 GeV/c per K/p), l'identificazione delle particelle prodotte nella collisione viene effettuata dal rivelatore di Tempo di Volo (TOF), basato su Multi-gap Resistive Plate Chamber (MRPC) ad alta efficienza e velocità di risposta e con risoluzione temporale intrinseca migliore di 40 ps.

Nel 2012, la Collaborazione ALICE ha presentato per l'esperimento un programma di aggiornamento che permettesse di sfruttare al meglio l'aumento delle luminosità previsto all'interno del collisionatore di particelle LHC per collisioni *Pb-Pb* dopo la seconda lunga sosta (LS2) delle attività che avrà termine nel 2020. I principali obiettivi di fisica che ci si attende di poter perseguire richiedono misure di segnali estremamente rari per cui è necessario ottenere la più grande statistica possibile. All'aumento delle luminosità segue un aumento della produzione di particelle conseguenti agli urti. Deve però fare seguito anche una capacità da parte del rivelatore di rivelare una quantità consistente di tali dati.

Il presente lavoro di tesi, sviluppato all'interno del gruppo di ALICE-TOF dell'Università di Bologna, è parte del lavoro effettuato per l'adattamento del rivelatore ai requisiti richiesti a partire dal 2020. Sono stati effettuati dei test sulla praticabilità del passaggio ad una lettura continua dei dati per il rivelatore TOF per quanto riguarda le collisioni pp rispetto alla modalità attuale basata su un sistema di trigger. Questa possibilità era stata inizialmente non considerata dalla Collaborazione in quanto avrebbe dovuto comportare una sostituzione di gran parte dell'elettronica con conseguente ingente aumento dei costi. Così facendo, però, il rivelatore TOF sarebbe limitato ad una massima frequenza di presa dati di 250 kHz, appena un quarto rispetto alla massima frequenza di interazione potenzialmente raggiungibile in ALICE per collisioni pp di 1 MHz.

Nel lavoro di tesi che presento, viene discusso un diverso sistema di lettura dei dati che permette di leggere i dati in maniera continua utilizzando l'elettronica attuale. Tale soluzione permetterebbe al rivelatore TOF dell'esperimento ALICE di raccogliere dati da tutti gli hit generati nelle collisioni pp alla frequenza di interazione di 1 MHz prevista a partire dal 2020 e di conseguenza l'acquisizione di una quantità di eventi per il rivelatore TOF quattro volte maggiore rispetto a quanto inizialmente previsto per tali frequenze con lettura basata sul sistema di trigger. I risultati ottenuti confermano che lo schema di read-out continuo proposto è una opzione percorribile per il rivelatore TOF dell' esperimento ALICE. I risultati evidenziano anche che potrebbe rivelarsi opportuno implementare un sistema di monitoraggio dei canali rumorosi per permetterne la disabilitazione in tempo reale.

Abstract

The quark-gluon plasma (QGP), first discovered at the CERN-SPS in 2000, constitutes the fourth state of matter known so far. It is believed that such a state could be found in nature in the core of neutron stars and that the very early Universe was in a QGP state for some instants at some microseconds after the Big Bang. To recreate such conditions, head-on collisions between massive ions are made up by particle accelerators. Strongly interacting particles at very high temperatures and energy densities are expected to compose the quark-gluon plasma. The main purpose of ultrarelativistic heavy-ion collisions is the investigation of the QGP.

The ALICE experiment situated at the CERN has been specifically designed to study heavy-ion collisions for centre-of-mass energies up to $\sqrt{s_{\mathrm{NN}}} = 5.5\ TeV$ per nucleon pair. Extended particle identification capability is one of the main characteristics of the ALICE experiment. In the intermediate momentum region (up to 2.5 GeV/c for π/K and 4 GeV/c for K/p), charged particles are identified in the ALICE experiment by the Time of Flight (TOF) detector. The ALICE-TOF system is a large-area detector based on the use of Multi-gap Resistive Plate Chamber (MRPC) built with high efficiency, fast response and intrinsic time resolution better than 40 ps.

In the 2012, an upgrade programme was presented by the ALICE Collaboration in order to fully exploit the scientific potential of the LHC for fundamental studies of QCD. The main physics topics addressed by the proposed upgrade programme for the ALICE experiment require the measurement of heavy flavour hadrons, quarkonia, and low-mass dileptons at low transverse momenta. Such measurements will be characterized by rare signals which calls for large statistics, better available with the luminosity enhancement foreseen after the LHC Long Shutdown 2 (LS2). An increase in the particle production from the collisions is expected to follow to the enhancement of luminosity. Thus, it also must follow the ability of the detector to detect a

consisting amount of such data.

This thesis work, developed with the ALICE-TOF Bologna group, is part of the efforts carried out to adapt the read-out of the detector to the new requirements after the LHC Long Shutdown 2. Tests on the feasibility of a new read-out scheme for the TOF detector have been performed. In fact, the achievement of a continuous read-out also for the TOF detector would not be affordable if one considers the replacement of the TRM cards both for hardware and budget reasons. Actually, the read-out of the TOF is limited at 250 kHz i.e. it would be able to collect up to just a fourth of the maximum collision rate potentially achievable for pp interactions.

In this Master's degree thesis work, I discuss a different read-out system for the ALICE-TOF detector that allows to register all the hits at the interaction rate of 1 MHz foreseen for pp interactions after the 2020, by using the electronics currently available. Such solution would allow the ALICE-TOF detector to collect all the hits generated by pp collisions at 1 MHz interaction rate, which corresponds to an amount four times larger than that initially expected at such frequencies with the triggered read-out system operated at 250 kHz for LHC Run 3. The obtained results confirm that the proposed read-out scheme is a viable option for the ALICE TOF detector. The results also highlighted that it will be advantageous if the ALICE-TOF group also implement an online monitoring system of noisy channels to allow their deactivation in real time.

Contents

Introduction

The Standard Model (SM) is at the present the most accredited theory for the description of nature, explaining the existence of elementary particles and their fundamental interactions. Quantum chromodynamics (QCD) is the gauge theory describing strong interactions between quarks within the Standard Model $U(1)_Y \otimes SU(2)_L \otimes SU(3)_C$ and it is responsible for the $SU(3)_C$ portion. Strongly interacting particles at very high temperatures and energy densities are expected to compose a new state of matter called quark-gluon plasma (QGP). The main purpose of ultrarelativistic heavy-ion collisions is the investigation of the QGP. It is believed that such a state could be found in nature in the core of neutron stars and that the very early Universe was in a QGP state for some instants at around $\sim 10^{-6}$ s after the Big Bang. To recreate such conditions, head-on collisions between massive ions are made up by particle accelerators.

The ALICE experiment has been specifically designed to study heavy-ion collisions up to $\sqrt{s_{\mathrm{NN}}} = 5.5\ TeV$ and to analyze QGP observables. Extended particle identification capability is one of the main characteristics of the ALICE experiment. The ALICE-TOF system is a large-area detector based on the use of Multi-gap Resistive Plate Chamber (MRPC) that are built with high efficiency, fast response and intrinsic time resolution better than 40 ps.

The main physics topics addressed by the proposed upgrade programme for the ALICE experiment require the measurement of heavy flavour hadrons, quarkonia, and low-mass dileptons at low transverse momenta. Such measurements will be characterized by rare signals which calls for large statistics, better available with the luminosity enhancement foreseen after the LHC Long Shutdown 2. While the excellent particle identification capabilities of the current ALICE detector have to be preserved, a significant improvement of secondary vertex identification and substainable read-out rate will

be needed.

In order to achieve access to rare physics channels and collect a large statistical sample of minimum-bias events, needed to better understand the QGP state, an upgrade has been scheduled for the Long Shutdown 2 (LS2), including a new inner tracking silicon detector, a new read-out of the TPC via Gas Electron Multipliers (GEM) and improved electronics. Between 2020-2028 an integrated luminosity of 10 nb^{-1} is foreseen to be collected.

This thesis work, developed with the ALICE-TOF Bologna group, is part of the efforts carried out to adapt the read-out of the detector to the new requirements after the 2018. It is developed in three parts. I discuss the physics of relativistic heavy-ion collisions by focusing on the QCD and on the characterization of the quark-gluon plasma with an overview on the physics results collected so far. Then I describe the ALICE experiment and its upgrade programme, planned for the 2018, and its physics motivations. I therefore develope a continuous read-out proposal for the TOF detector and its criticalities.

Chapter 1

The physics of ultrarelativistic heavy-ion collisions

Strongly interacting particles at very high temperatures and energy densities are expected to compose a new state of matter called quark-gluon plasma (QGP). The main purpose of ultrarelativistic heavy-ion collisions (URHICs) is the investigation of the QGP. It is believed that such a state could be found in nature in the core of neutron stars and that the very early Universe was in a QGP state for some instants at around $\sim 10^{-6}$ s after the Big Bang.

To recreate such conditions, head-on collisions between massive ions are made up by particle accelerators. In these heavy-ion collisions protons and neutrons composing the two nuclei smash into one another, forming a *deconfined* state of quarks and gluons. The initial shape of the collision zone is usually an ellipse. Pressure in the liquid seeks to make the matter round, so it makes the liquid flow faster in the shorter directions. As the fireball instantly expands and cools down, the quarks hadronize and the system freezes out. Furthermore, the individual partons recombine into ordinary matter that typically speeds away in all directions. The debris contains nuclei of atoms or antiatoms which are made up by quarks and antiquarks yielded by the collision. What takes place during the expansion and hadronization phases can be inferred from the study of the dynamical properties of the resulting hadrons [1].

The first ideas for experiments to search for the QGP emerged in the 1970s, when the QCD state equations (see Sec. 1.1) began to prospect

the likelihood of a quark state of matter at temperatures and densities accessible to high-energy heavy-ion collisions experiments. The experimental attempts to create the QGP in the laboratory and to measure its properties started around 1975 at the Bevalac (Billions of eV Linear Accelerator), Lawrence Berkeley Laboratory (Long Island, USA), with a centre-of-mass energy per pair of colliding nucleons of $\sqrt{s_{\mathrm{NN}}} \simeq 1\ GeV$. Energies rised to $\sqrt{s_{\mathrm{NN}}} = 5\ GeV$ at the Alternating Gradient Synchrotron (AGS) at BNL (Brookhaven National Laboratory, USA), and to $\sqrt{s_{\mathrm{NN}}} = 17\ GeV$ at the Super Proton Synchrotron (SPS) at the CERN, in the 1980s and 1990s. The results obtained at SPS led the CERN to announce indirect evidence for a "new state of matter", in 2000 [2].

Four experiments (STAR , BRAMHS, PHENIX, PHOBOS) have been put into action at the Relativistic Heavy Ion Collider (RHIC) at BNL in the 2000s with $\sqrt{s_{\mathrm{NN}}} \simeq 200\ GeV$. Their results have provided clearer indications of the formation of the QGP at high temperature and low baryon density.

Further confirmations came from the experiments of the LHC, at the CERN, where the ALICE experiment is specifically optimized to study *Pb-Pb* collisions.

1.1 Strong interactions

Quantum chromodynamics (QCD) is the gauge theory describing strong interactions between quarks. It constitutes a fundamental theory within the Standard Model $U(1)_Y \otimes SU(2)_L \otimes SU(3)_C$ and it is responsible for the $SU(3)_C$ portion. Weak and electromagnetic interactions are considered unified in the single $U(1)_Y \otimes SU(2)_L$ symmetry group where Y, the weak hypercharge, is the generator of the group that is given by the Gell-Mann–Nishijima relation between electrical charge and isospin $Q = \frac{Y}{2} + I_3$. The subscript L is used to denote left-handed spinors recording the vector-axial nature of the charged currents and the subscript C refers to the charge of strong interactions given by the *colour*.

In quantum field theories, charges point out any generator of continuous symmetries in a physical system. In correspondence of a symmetry the existence of a conserved current is implied according to the Noether's theorem. For example, the electric charge is the generator of the $U(1)$ symmetry group of electromagnetism and the corresponding conserved current is the electric current. The charge is then the generator of the local symmetry

group. A gauge field is associated to each charge and the request of the local gauge invariance of the lagrangian leads to the introduction of new vector fields (as many as the generators of the group, $N^2 - 1$ for $SU(N)$), when the field is quantized. In the QCD, these fields are associated to 8 ($N_C^2 - 1 = 8$, for $SU(3)_C$) gauge bosons which take the name of *gluons* and are the intermediate bosons of the strong interactions corresponding to the eight Gell-Mann generators of the $SU(3)_C$ group.

The QCD is a complex *non-abelian* quantum field theory: gluons carry colour charge (they are said *coloured*) and thus they can interact with themselves. Quantum electrodynamics (QED), instead, is a *linear* theory. Photons cannot interact with themselves and they do not carry electrical charge.

Quarks (q) and corresponding antiquarks ($\bar{q}$) occur in six different *flavours*: u, d, c, s, t, b. They are spin $\frac{1}{2}$ fermions and they carry both electrical and colour charges. Quarks have a fractional – with respect to the electron charge e, taken as unity – electric charge Q and they are classified according to the flavour quantum number as: up (u), charm (c), top (t), with $Q = +\frac{2}{3}|e|$, and down (d), strange (s), bottom (b), with $Q = -\frac{1}{3}|e|$. Antiquarks present electric charges of the same module but opposite in sign. The colour is the charge of the strong interactions and quarks and antiquarks are the only fermions endowed with colour quantum numbers. The colour quantum number is linked to the colour charges by the colour isospin $I_3^C \equiv \lambda_3$ and the colour hypercharge $Y^C \equiv \frac{1}{\sqrt{3}}\lambda_8$, where λ_i indicate the Gell-Mann matrices. While quarks present colours, i.e. *red* (r), *green* (g), *blue* (b), antiquarks have anticolours: *cyan* ($\bar{r}$), *magenta* ($\bar{g}$), *yellow* ($\bar{b}$) [3].

With colour, quarks gain an additional degree of freedom that has been decisive to solve the problem of the *particle proliferation*. Thus, quarks take a threefold variety of colours, e.g. an *up* quark is presented as a colour triplet (u_r, u_g, u_b), and so on. One might therefore expect each hadron to exist in a multitude of versions due to all possible colour combinations, instead hadrons occur in nature only as neutral colour combination particles. This is known as *colour confinement* (see Sec. 1.1.2) and it is equivalent to say that free quarks do not exist in nature. There are two kinds of hadrons, or, in other words, two ways to achieve colour neutrality: *mesons* and *baryons*. Mesons are composed of a $q\bar{q}$ pair that carry opposite signs of the same colour while baryons are composed by a triplet qqq of three different coloured quarks. Such quarks determine the properties of a hadron

and they are named *valence quarks*.

Then, the density of the QCD Lagrangian is

$$\mathcal{L}_{QCD} = \bar{q}_i^{\alpha} \left(i\gamma^{\mu}\mathcal{D}_{\mu} - \hat{m}\right)_{ij}^{\alpha\beta} q_j^{\beta} - \frac{1}{4} G_{\mu\nu}^{\alpha} G_{\alpha}^{\mu\nu} \tag{1.1}$$

where:

- γ are the Dirac matrices;
- $q_i^{\alpha}(x)$ denotes the quark fields of colour ($i = 1 \div 3$) and of flavour ($\alpha = 1 \div 6 = u, d, c, s, t, b$);
- the mass matrix is colour independent and it is diagonal in the flavour space: $\hat{m} = diag_f(m_{1\div 6})$;
- the covariant derivative in the Eq. (1.1) has the form of a 3×3 matrix and it is defined as

$$(\mathcal{D}_{\mu})_{\alpha\beta} \equiv \delta_{\alpha\beta}\partial_{\mu} - ig \left(\frac{\lambda^{\alpha}}{2}\right)_{\alpha\beta} A_{\mu}^{\alpha}, \tag{1.2}$$

  where:

  - A_{μ}^{α} is the gluon field, with $\alpha = 1 \div 8 = N_C^2 - 1$,
  - g is the bare coupling constant,
  - λ_{α} denotes the Gell-Mann matrices of the gauge $SU(3)_C$ group;

- the gluonic field tensor is

$$G_{\mu\nu}^{\alpha} = \partial_{\mu} A_{\nu}^{\alpha} - \partial_{\nu} A_{\mu}^{\alpha} + g f^{abc} A_{\mu}^{b} A_{\nu}^{c}, \tag{1.3}$$

  where f_{abc} is a totally antisymmetric tensor and its elements are the structure constants of the $SU(3)$ group [4].

The bilinear term in the gluonic fields $A_{\mu}^{\alpha} + g f^{abc} A_{\mu}^{b} A_{\nu}^{c}$ generates self-interaction terms with vertices of three and four gluonic propagators. This expresses the non-abelianity of the theory [5].

All interactions contained in the QCD lagrangian depend on a single gauge coupling constant $g = g_s$ for strong interactions. This is known as *universality*.

1.1.1 Couplings and asymptotic freedom

Each of the four fundamental interactions can be characterized by a dimensionless parameter expressed in terms of universal constants, the *coupling constant*. In the lagrangian of strong interactions, the coupling constant α_S is parameterized by the gauge coupling parameter, g, giving in natural units

$$\alpha_S = \frac{g^2}{4\pi}. \tag{1.4}$$

However, in a general field theory, the effective coupling constant is not a constant, but it depends on a momentum or distance scale due to renormalization effects. The effective coupling constant decreases at short distances, or equivalently, at high momenta. Such theories are said to be asymptotically free.

Asymptotic freedom is actually one of the main features of the QCD. It is expressed by the dependence of the gauge bare coupling constant g by the scale energy of the physical processes considered, described by the *beta function*

$$\beta(g) = \mu\frac{\partial g}{\partial \mu} = \frac{\partial g}{\partial ln\mu}, \tag{1.5}$$

where μ is the energy scale of the given physical process. In quantum field theories, a beta function encodes the running of a coupling parameter g. If the beta function vanishes, the theory is said to be scale-invariant. In non-Abelian gauge theories, the beta function can be negative and therefore the coupling decreases logarithmically[1], as it is shown in Fig. 1.1. As a consequence, quantitative calculations based on a perturbative sum of Feynman diagrams, works. Viceversa, perturbative calculations fail at high energies.

In QED, an electron can emit a single virtual photon or it can emit a photon that subsequently can annihilate in an electon-positron pair, and so on, provided that the energy remains conserved within the Heisenberg's uncertainty principle. Thus, around the bare charge of an electron, e^+e^- pairs arise in the vacuum with positrons closer to the electron. This generates a cloud of polarized charges shielding the negative charge of the electron (*charge screening*). The effect becomes more significant as one gets closer to the electron, for example with a charge probe.

[1]This was first found by F. Wilczek, D. Politzer and D. Gross, Nobel prize in Physics in 2004 "for the discovery of asymptotic freedom in the theory of strong interaction".

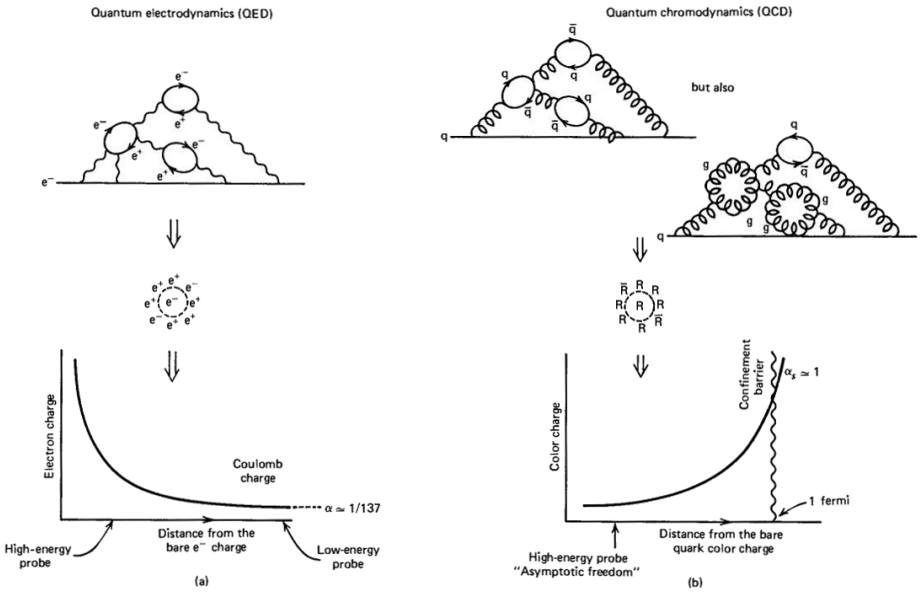

Figure 1.1: *Screening of the electric (a) and colour (b) charges in quantum field theory. Feynman's diagrams for the creation of virtual particles for the two processes are also showed [6].*

In QCD, instead, the effect is the opposite and a charge is preferably surrounded by other charges of the same colour. The more one approaches the charge, the weaker the charge appears (*charge anti-screening*), and the two charges become non-interacting (*asymptotic freedom*).

The asymptotic freedom can be analyzed in the framework of the renormalization group theory. In field theories, quantum corrections obtained via the perturbative approach presents divergences that can be re-absorbed by renormalizing some appropriate parameters. This is true for renormalizable theories such as QED and QCD. The energy scale at which the divergences are absorbed is called the renormalization point. One of the most important results of the renormalization group theory is the dependence of the coupling constant of the theory from the transferred momentum.

In particular, in the case of QCD, one gets for the leading order the following dependence on the transferred four-momentum q:

$$\alpha(|q^2|) = \frac{12\pi}{(11n - 2f)\, ln\left(\frac{|q^2|}{\Lambda^2_{QCD}}\right)}, \tag{1.6}$$

where n indicates the number of colours, f the number of quark flavours

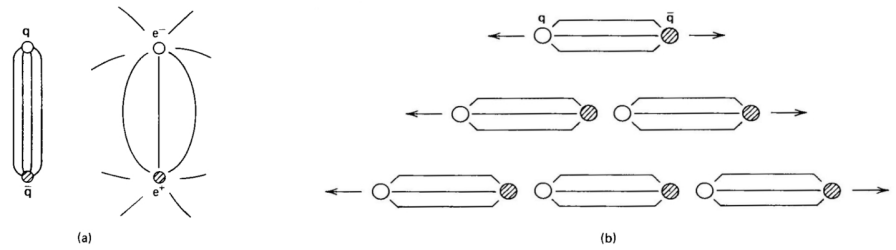

Figure 1.2: *Differences between lines of force of electric field and colour field (a). Formation of new $q\bar{q}$ pair at the increasing of the separation energy (b).*

and Λ_{QCD} ($\approx 200\ MeV$) represents an intrinsic energy scale for the strong interaction, at which perturbative approach can be applied. It is $11n > 2f$ in nature and, in consequence, the strength of strong interactions α_S decreases at small distances (or high energies).

Many interesting aspects of the QCD such as confinement from hadronic matter to QGP occur at low energies ($T \sim \Lambda_{QCD}$) and therefore they can not be treated perturbatively. Asymptotic freedom of strong interactions permits to perturbatively study the theory only for high transferred momentum. For energies around Λ_{QCD} the theory cannot be used and it is easy to see that the Eq. (1.6) presents a divergence for $q^2 \to \Lambda^2_{QCD}$.

1.1.2 Colour confinement

The term *confinement* indicates that coloured free particles do not exist in nature.

Besides valence quarks, a hadron contains a population of more quarks and gluons. From the graphic depicted in Fig. 1.1 (b) it is possible to infer that the strong interaction between two quarks enhances with the increasing of their distances. The corresponding colour field lines of force between the quark and the antiquark become packed into a tube-like region, as shown in Fig. 1.2 (a). This constitutes a significant difference with the Coulomb field where there is no self-coupling of the photons to contain lines of force and then nothing prevents them from spreading out. If the colour tube is supposed to have a constant energy density per unit length, the potential energy between a quark and an antiquark in a hadron grows with separation and its form can be assumed $V \sim \lambda r$. The separation can go on until the potential energy becomes high enough to create another $q\bar{q}$ pair. (Fig. 1.2

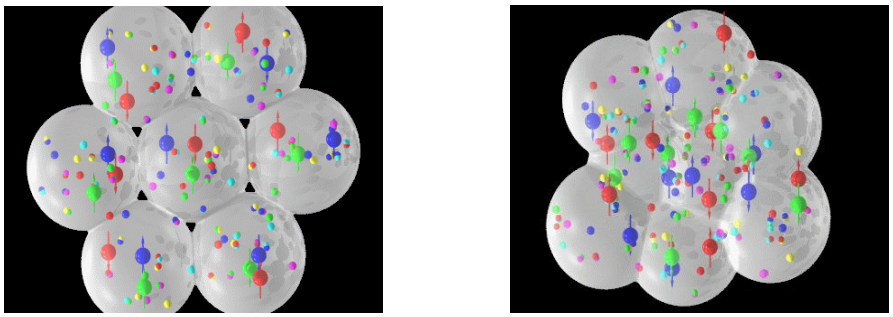

Figure 1.3: *A comparison between confined (on the left) and deconfined (on the right) phase in a heavy nucleus.*

(b)) The process also works backwards i.e. the annihilation of two quarks produces a gluon. Such new quarks - and gluons - are said *of the sea*. Why quarks and gluons cannot escape from hadrons results now explained.

One should infer that the origin of the hadron mass is the strong interaction since light quark masses only represent less than 10% of the total hadron mass. In this respect, the Higgs boson only explains about 1% of the total mass of the proton and neutron which are the main massive constituents of ordinary matter [7].

Although the phenomenon of confinement has been clearly observed, it is not supported by accurate predictions within the Standard Model, and in general, unlike the electroweak interactions, it is not possible to handle the QCD with the perturbative approach, as mentioned in Sec. 1.1.1. However, lattice non-perturbative approaches have confirmed quark confinement as an intrinsic property of QCD. While, as remarked, in normal conditions quarks and gluons are confined in their parent hadrons, at the QGP condition they are expected to be free to move through protons and neutrons that constitute the nucleus, as depicted in Fig. (1.3). Such phase is known as *deconfined*. A state in which quarks and gluons from originary nucleons are free to move through the matter, i.e. *deconfinement*, is expected to happen at extreme conditions of temperature and density, as those expected for the first few instants ($\sim 10^{-6} s$) after the Big Bang.

1.1.3 Symmetries of the QCD

An important feature of the QCD is the conspicuous amount of symmetries of its lagrangian. First and foremost, its lagrangian is invariant

under local gauge transformations, i.e. one can redefine the quark fields indipendently at every point in the space-time, without changing the physical content of the theory. This determines a number of implications in the dynamics of the theory. Furthermore, strong interactions do not depend on the quark flavour and if the masses of quarks are identical, the QCD Lagrangian stated at the Eq. (1.1) is invariant under arbitrary flavour rotations of the quark fields. This flavour symmetry introduces the symmetry under isospin transformations. If one requires that *all* the quark masses are equal to zero, the flavour symmetry can be enlarged. Fields in the Eq. (1.1) can be decomposed in left-handed and right-handed quark fields [6]

$$q_{L,R} = \frac{1}{2}\left(1 \pm \gamma_5\right) q. \tag{1.7}$$

These are eigenstates of the Dirac chirality operator γ_5 with eigenvalues ± 1. For massless free quarks the chirality coincides with the helicity[2] $\vec{\sigma}\cdot\hat{p}$. So, in the chiral limit ($m_i \to 0$) chiral symmetry is an exact symmetry; otherwise it is an approximate symmetry.

Then, the QCD Lagrangian density becomes

$$\mathcal{L}_{(m_q \to 0)} = -\frac{1}{4} G^{\mu\nu} G_{\mu\nu} + i\bar{q}_L \not{\partial}\, q_L + i\bar{q}_R \not{\partial}\, q_R \tag{1.8}$$

and it is symmetric for the group

$$U(1)_V \otimes U(1)_A \otimes SU(n_f)_L \otimes SU(n_f)_R \otimes SU(3)_C \tag{1.9}$$

where $U(1)_V$ is the vector baryon conservation symmetry group and its axial counterpart is $U(1)_A$. The lagrangian of a physical system is chirally symmetric if it is invariant under the global $SU(n_f)_L \otimes SU(n_f)_R$ transformations

$$\begin{aligned} SU(n_f)_L \quad &: \quad q_L \to e^{i\theta_a^L \frac{\lambda^a}{2}} q_R \\ SU(n_f)_R \quad &: \quad q_R \to e^{i\theta_a^R \frac{\lambda^a}{2}} q_L \end{aligned} \tag{1.10}$$

where θ_a are the generators of the $SU(n_f)$ group.

Requiring this symmetry is equivalent to require the one that leaves the lagrangian invariant under global vector and axial vector transformation on the chiral symmetry group $SU(n_f)_V \otimes SU(n_f)_A$.

[2] The helicity is defined as the projection of the spin $\vec{\sigma}$ on the direction of the momentum $\hat{p} = \frac{\vec{p}}{|p|}$.

Spontaneous breakdown of the $SU(n_f)_V$ group due to the quark masses produces the breaking of the entire group symmetry stated in Eq. (1.9).

In relativistic quantum field theories (RQFTs), the spontaneous breaking of exact continuous global symmetries implies the existence of massless Goldstone bosons. In the case of chiral symmetry and under chiral limit, they can be identified with the pion triplet ($\pi = \bar{q}q$, $n_f^2 - 1 = 3$).

If chiral symmetry would be an exact symmetry of QCD the pions should be massless. Instead, due to masses of quarks it is an approximate symmetry and pions are expected to have finite – even though relatively small – masses. In fact, the mass of pions is $\sim$140 MeV, quite small if compared, for example, with the proton mass that is $\sim$940 MeV.

The spontaneous symmetry breaking of chiral symmetry corresponds to the existence of a non-zero vacuum expectation value of the axial symmetry. This has non-perturbative origin and it is related to the existence of a non-zero *chiral quark condensate* $\langle\bar{q}(x)q(x)\rangle$. This condensate is a measure of spontaneous chiral symmetry breaking. The connection between spontaneous chiral symmetry breaking and non-vanishing chiral condensate can be highlighted by introducing a pseudoscalar operator $P(x) \equiv \bar{q}(x)\gamma_5 q(x)$. The pseudo-scalar operator P applied to the ground state returns a pion, that is the massless Goldstone pseudoscalar boson: $P|0\rangle = |\pi\rangle$. If f_π indicates the pion decay constant, the chiral condensate expectation value can be derived from the GOR (Gell-Mann, Oakes, Renner) relation

$$m_\pi^2 f_\pi^2 = -(m_u + m_d)\langle\bar{q}(x)q(x)\rangle, \tag{1.11}$$

that gives

$$\langle\bar{q}(x)q(x)\rangle = -(240\ MeV)^3. \tag{1.12}$$

The chiral condensate is calculated as a function of the temperature T and of the density ρ. In the limit for low temperatures and low densities it is

$$\frac{\langle\bar{q}q\rangle_{T,\rho}}{\langle\bar{q}q\rangle_0} \sim 1 - aT^{-2} - b\rho \tag{1.13}$$

where $\langle\bar{q}q\rangle_0$ is the vacuum condensate at $T = 0$ and $\rho = 0$, with a, b being constant. As it can be seen from the Eq. (1.13), in high temperature and high density regime, the chiral condensate approaches to zero. Although for the ordinary hadronic matter the chiral symmetry is broken at low temperature, it is expected that in conditions created by heavy-ion collisions the quarks are deconfined and the chiral symmetry becomes restored. This suggests that the chiral symmetry can be restored in the QGP phase.

1.2 The quark-gluon plasma

The basic idea about the QGP is that at sufficiently high energy or density of hadronic matter, the quarks and gluons become deconfined. Statistical mechanics applied to QCD gives the theoretical support and basic indications to investigate such new state of matter and the phase change that is predicted to take place.

1.2.1 QCD phase diagram

The QCD phase diagram aims to describe the behaviour of matter in which the interactions between particles are ruled by the quantum chromodynamics. The QCD phase transition scheme, in fact, is yet under studies and one of the targets of the research is therefore to quantitatively map it out.

A comparison between the phase diagram for water and QCD matter gas is shown in Fig. 1.4. In classical thermodynamics, phase diagrams present three broad regions, one for each phase of the matter (gas, liquid, solid), typically separated by phase transition lines. In correspondence of the triple point, all the three phases can exist. The critical point, defined by the *critical temperature*, T_C, and *critical energy density*, ϵ_C, indicates the condition at which the vapour pressure curve terminates and liquid and gas phases can coexist. Of course, in classical thermodynamics and especially in the case of water, all features are experimentally well established with great accuracy.

The QCD phase diagram is usually built as a function of the baryo-chemical potential μ_B vs the temperature T according to phenomenological models and mainly to lattice QCD (L-QCD) calculations (see Sec. 1.2.2). This is because, in thermodynamics, the chemical potential μ quantifies the variation of the internal energy of the system U after the introduction of an additional particle, $\mu = \frac{\partial U}{\partial N}$. The baryo-chemical potential μ_B is the chemical potential for a single baryon and it expresses the energy needed to increase the baryon quantum number, that is a globally conserved property of dense hadronic matter. The addition of a baryon-antibaryon pair, then, would not affect the global energy of the system that can be expressed by the first law of thermodynamics as $dE = -PdV + TdS + \mu_B dB$. A variation of μ_B, instead, would change the global energy of the system, its pressure

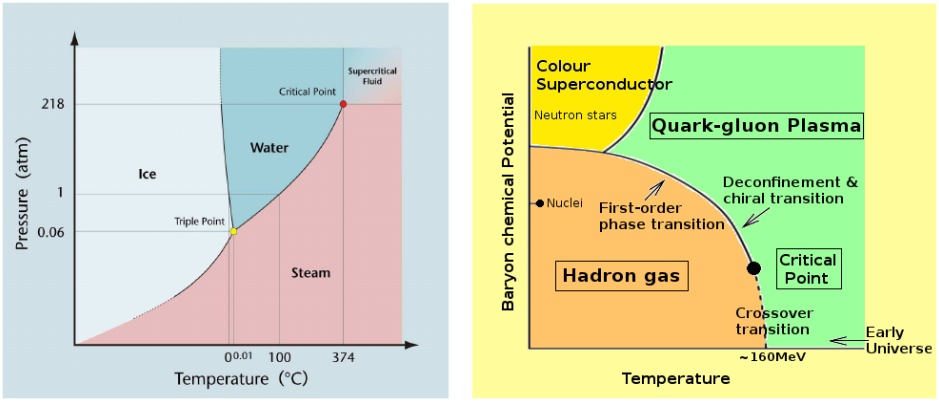

Figure 1.4: *The well-known phase diagram of water (on the left) and (on the right) a QCD phase diagram.*

or its temperature [3]. The baryo-chemical potential is also connected with the baryon density number n_B and it can represent the pressure P. As a consequence, it is closely linked to the hadronic density ρ_B. Furthermore, μ_B is a measurable quantity and, unlike the density, it remains continuous during the phase transition [8].

Various effective theories and phenomenological models are the basis of the schematic phase diagram of QCD that is shown in the right side of Fig. 1.4 [9]. The transition to the QGP can be induced either by increasing the temperature or the density. At low temperatures and high values of the chemical potential, nuclear matter consists of an interacting and degenerate highly compressed Fermi gas of quarks. The interaction among the quarks can be attractive in specific combinations of colours states, leading to the formation of quark-quark pairs which determine a colour superconducting phase. While in the case of early Universe the transition from QGP to hadrons is supposed at high temperature and vanishing chemical potential, it is thought that in the neutron stars, due to gravitational collapse, the QGP state should be formed for high values of the baryo-chemical potential and temperature close to zero. The LHC achieves experimental conditions close to those supposed for the primordial stages of the Universe, with high T and low μ_B, thus allowing to investigate in a region of highest interest in the QGP phase transition scheme. Thus, such conditions are also the frame for most L-QCD calculations and results [10].

The search for experimental evidences of the creation of a deconfined

phase is linked to the nature of the transition between confined and deconfined phases and then to the prediction for observables in a QGP creation experiment. The nature of such transition depends also on the number of quark flavours involved and on their masses.

A phase transition is classified according to the free energy F as a function of the temperature. If a discontinuity occurs, then a phase transition is expected. The free energy F is defined as $F = U - TS$, where U is the free internal energy and S the entropy of the thermodynamic system. A n^{th} order phase transition implies that $\frac{\partial^n F}{\partial T^n}$ is discontinuous while $\frac{\partial^{n'} F}{\partial T^{n'}}$, with $n' < n$, is continuous. A first order transition implies a discontinuity in the free energy derivative $\frac{\partial F}{\partial T} = S$ that means that a latent heat is associated to the transition. In second order transitions, there are discontinuities only for derivatives of orders higher than the first. In a *crossover* region, the transition takes place without discontinuities for the free energy and its derivatives and an abrupt change in the phase transition from a phase to another is not observed. In a QCD phase transition scheme (Fig. 1.4), the first order phase transition line divides the hadronic matter area from the quark-gluon plasma state. At the crossover point, the confined phase of hadronic gas and the deconfined state of QCD can cohexist.

Analogies with classical thermodynamics and other arguments based on a variety of models could suggest that one should expect that the phase transition line ends at a critical point as a first-order phase transition is a function of temperature at finite μ_B. Furthermore, L-QCD calculations at non-zero baryo-chemical potential suggest the existence of a tri-critical point $(\mu_{B,c}; T_c)$ at which the first order transition becomes a crossover for $\mu_B < \mu_{B,c}$ and $T < T_c$. However, the existence of a critical point is not yet established experimentally.

Figure 1.5 shows the result of L-QCD calculations for hadronic matter phase and shows the dependence of phase transitions on the number of flavours for $\mu_B = 0$ and m_u=m_d. In the case of three flavours, the order of the transition varies depending on mass values that u, d or s quarks assume. The tri-critical value for the mass of the s quark is indicated by m_s^{tric}. Beyond such value, the transition becomes of second order, while $m_{u,d}$ is set to zero.

Quantum chromodynamics is highly dependent on values of parameters entering the lagrangian. In particular, number of quark flavours and

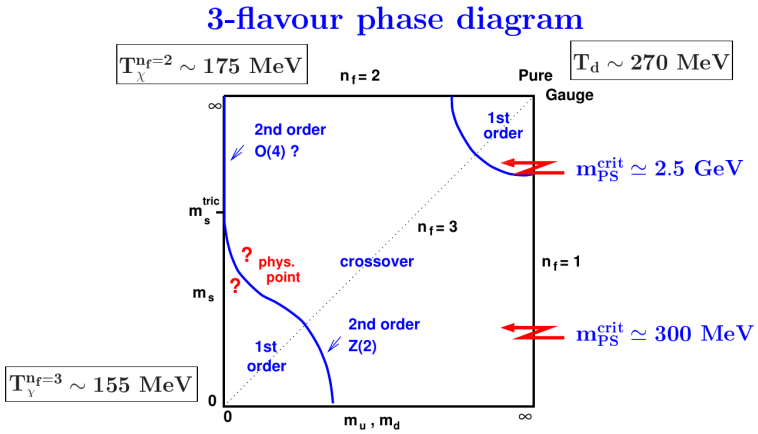

Figure 1.5: *Dependence of the phase transition orders on quark masses and on number of flavours considered in the QCD lagrangian. The results obtained in the calculation are expressed in the lagrangian in terms of a observable, i.e. the ratio of the lightest pseudo-scalar and vector meson masses (m_{PS}/m_V). Temperatures for deconfinement and for chiral symmetry restoration in the case of two distinct phase transitions are also reported (see Sec. 1.2.2) [11].*

quark masses can affect some symmetries (e.g. the restoring of the chiral symmetry) and then the order of the phase transitions. The greatest effects are expected by variations of the lighter quark masses which dominate the dynamic of the system. In the low μ_B values region, transitions strongly depend on the number of quark flavours and on the masses of light quarks. It is still unclear whether the transition shows discontinuities for realistic values of the light quark masses, or whether it is a crossover. Recent calculations [10, 12] indicate that the transition is a crossover for values of $\mu_B \leq 400\ MeV$.

1.2.2 Lattice QCD calculations

Due to the asymptotic freedom, the coupling constant α_S of QCD is a diminishing function as the energy scale increases (see Eq. (1.6)). Therefore, the high-energy or equivalently the short-distance behavior can be described by a perturbative expansion, but a perturbative approach to the QCD fails at large distances where the α_S begins to diverge as the scale of energy decreases. A different approach allows to better characterize the transition to the deconfined state of hadronic matter and the physical mechanisms at the origin of colour confinement. A suitable non-perturbative approach is

the numerical study of QCD on a lattice (L-QCD).

The leading idea is to outline QCD interactions as a grid in the space-time with quarks placed on nodes and gluonic fields on links. While the size of the grid is considered infinitely large, the sites are infinitesimally close to each other. Many progresses have been achieved on the algorithms and on the computing performances and nowadays L-QCD computation represents a notably reliable method to test QCD in the non-perturbative domain. The computational complexity of such calculations is so high that the INFN began to build specific SIMD supercomputers[3] (APE Project) to perform these simulations already in 1984.

Lattice calculations present intrinsic systematic errors due to the use of a finite lattice cutoff and to the use of quark masses which become eventually infinite. To lessen the computational load, so-called quenched calculations are introduced. In such approximations quark fields are considered as non-dynamic "frozen" variables [13]. While this represented the ordinary way to perform calculations in early L-QCD computing, "dynamical" fermions are now standard [14, 15]. In addition, numerical methods suffer in evaluating integrals of high oscillatory functions with a large number of variables. This is the fermion sign problem that emerges for example when quark-chemical potentials are included, e.g. in calculations at non-zero net baryon density or when wave functions change sign due to the effects of the symmetry introduced by the Pauli's principle [16].

Relatively simple models (e.g. the MIT Bag Model [8]) furnish yet a reasonable valuation for the critical temperature $T_C \sim 170\ MeV$ and the critical energy density $\epsilon_C \sim 1\ GeV/fm^3$.

Lattice QCD calculations have shown that for massless quarks at baryonic potential $\mu_B = 0$ the transition to the QGP happens via a first order transition if $n_f \geq 3$ (three quarks with zero masses) and via a second order transition for $n_f = 2$ (two quarks and zero masses). Critical temperature should amount to $(173 \pm 15)\ MeV$, and the critical energy density to $\epsilon = (0.7 \pm 0.3)\ GeV/fm^3$, where the uncertainties are mainly due to the method used for its determination [11]. More realistic calculations that include the mass for the s quark (case "2+1 flavours" in Fig. 1.6) indicate that at zero chemical potential the transition appears most likely as a crossover.

[3]Single Instruction Multiple Data (SIMD) computers are vector machines where a single control unit can drive several functional units which are able to execute simple operations. SIMD computers can be considered precursors of modern GPUs.

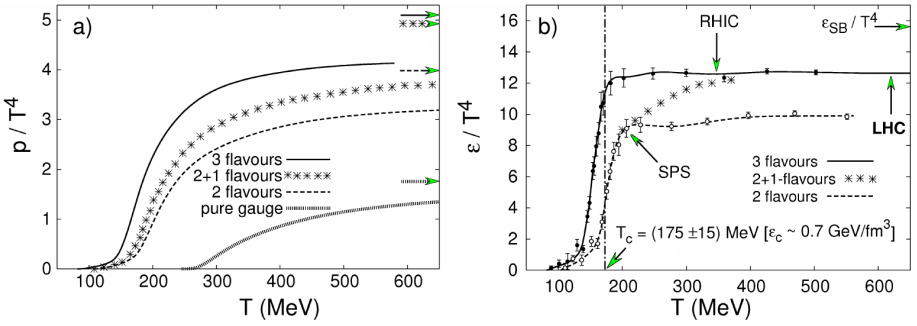

Figure 1.6: *Dependence of the pressure (right) and of the energy density (left) as a function of the temperature of the hadronic matter at null baryonic potential given by lattice QCD calculations at finite temperature. For the calculations with a real s mass, the transition is faded away. Values for an ideal gas are indicated by arrows (Stefan-Boltzmann limit) [11].*

If the transition was of the first order, ϵ would have a discontinuity in correspondence of the critical temperature T_C. Since the crossover takes place in a small range of temperatures, the phase transition shows a rapid variation in the observables and in Fig. 1.6 it can be seen that the energy density ϵ abruptly rises in just 20 MeV of temperature interval.

In Fig. 1.6 it is also visible that the saturated values of energy density at high temperatures are still under the Stefan-Boltzmann limit; this indicates residual interactions among the quarks and gluons in the QGP phase. Even the p/T^4 ratio saturates under the SB limit, for temperatures $\sim 2T_c$. This suggests a non ideal behavior for the gas considered in Lattice QCD calculation.

The inclusion of lighter quarks masses in the calculations results in a significant decrease for the transition temperature, but early predictions led to significant discrepancies in the results.

Although critical temperature depends on the number of quark flavours involved in the restoring of the chiral symmetry, these differences strongly diminished in current calculations. A reliable extrapolation of the transition temperature to the chiral limit gave [17]

$$T_C = \begin{cases} (173 \pm 8)\ MeV, & n_f = 2 \\ (154 \pm 8)\ MeV, & n_f = 3 \end{cases} . \tag{1.14}$$

Calculations based on chiral order parameter show a crossover tran-

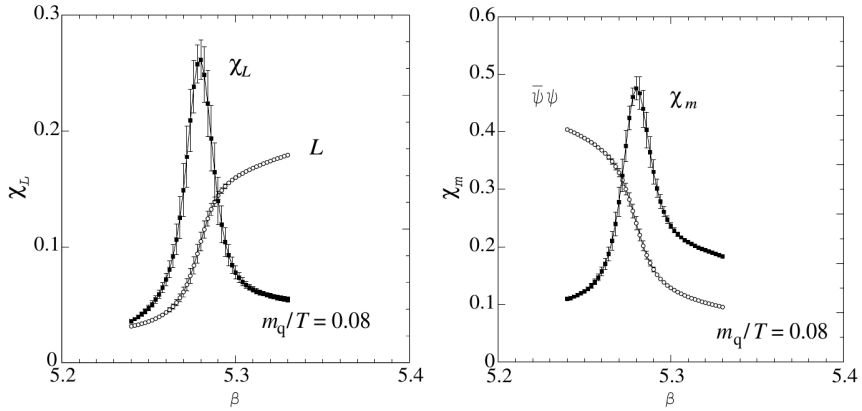

Figure 1.7: *Deconfinement (on the left) and restoration of chiral symmetry (on the right) in two-flavours L-QCD for a quark mass which scales with temperature as* $m_q = 0.08\ T$. *Circles indicate the Polyakov loop* L *on the left side and the quark chiral condensate* $\psi\bar{\psi}$ *on the right side. The corresponding susceptibilities* χ_L *and* χ_m *are also showed. All quantities are expressed as a function of the coupling* $\beta = 6/g^2 \sim T$.

sition for $T_\chi = 155\ MeV$. In addition, even though QCD seems to give only one transition from the low temperature hadronic regime to the high temperature plasma phase, it has been speculated that two distinct phase transitions leading to deconfinement at T_d and chiral symmetry restoration at T_χ could occur in QCD, with $T_d \leq T_\chi$ according to general arguments about energy scales [18].

Another important outcome of lattice QCD is the prediction of the restoration of the chiral symmetry (see Sec. 1.1.3) that would occur in correspondence of the deconfinement transition. It is expected, in fact, that the value of the chiral condensate after the deconfinement transition goes to zero, allowing the restoration of the chiral symmetry.

Figure 1.7 shows a comparison between predictions in two-flavours L-QCD for the chiral condensate $\psi\bar{\psi}$, which is the order parameter for chiral-symmetry breaking in the chiral limit ($m_q \to 0$), and the Polyakov loop, which is the order parameter for deconfinement in the pure gauge limit ($m_q \to \infty$). It can be seen that as the temperature increases through the crossover, the value of the chiral condensate $\psi\bar{\psi}$ drops down and the Polyakov loop boosts. Such variations occur at the same temperature, suggesting that deconfinement and restoration of chiral symmetry happen at the same temperature. The corresponding susceptibilities $\chi_L \propto \left(\langle L^2\rangle - \langle L\rangle^2\right)$

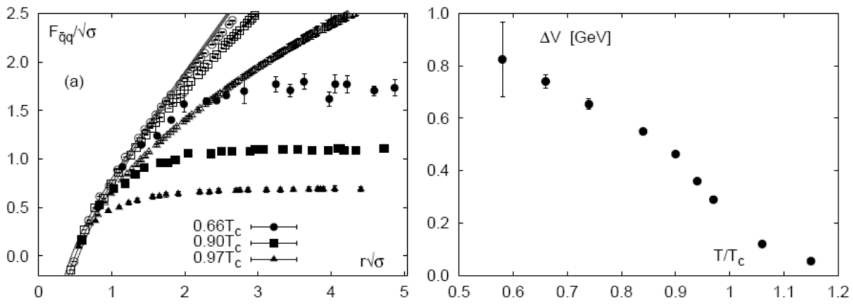

Figure 1.8: *Heavy quark potential for 3-flavours QCD vs the $q\bar{q}$ separation. The different points corresponds to lattice calculations with different temperatures. The separation is indicated in units of string tension σ. The right hand figure gives the limiting value of the free energy as a function of temperature for the case of three flavour QCD The quark mass used in the $n_f = 3$ calculations corresponds to a ratio of pseudo-scalar and vector meson masses of $m_{PS}/m_V \simeq 0.7$.*

and $\chi_m = \partial\langle\psi\bar{\psi}\rangle/\partial m$ are also showed. Their peak occur at the same value of the coupling [3].

In addition, the calculation of the potential energy between two heavy quarks as a function of the temperature shows a confirmation of the deconfinement. In Fig. 1.8 it is shown the predicted behaviour in the three flavour QCD scenario of the potential energy between a quark and an antiquark. It can be seen on the left side that as the separation increases, the potential energy flattens and it becomes constant at long distances, validating the hypothesis of deconfinement. On the right side, instead, it is shown that the separation between a quark and and antiquark decreases with the raise of the temperature [19].

Finally, the results of lattice calculations suggest to consider the QGP as a weakly coupled medium characterized by the coupling constant

$$\alpha_S(T) \propto \frac{1}{log\left[\frac{2\pi T}{\Lambda_{QCD}}\right]}, \tag{1.15}$$

confirming the evidence of deconfinement found at SPS and the perfect fluid behavior highlighted by RHIC data and discussed later in the chapter [20].

1.2.3 Evolution of collisions and QGP

Extreme density and temperature allow the transition for the ordinary matter to the deconfined phase, in which quarks and gluons are free from their parent hadrons and they can interact with each other. Such conditions can be reached by ultrarelativistic heavy ion collisions.

Different phases of evolution of the matter are predicted according to theoretical models and on the basis of data collected so far. Nuclei that are accelerated to ultrarelativistic energies become Lorentz-contracted and they are supposed to be in a glass colour condensate state [21, 22]. Protons and neutrons of colliding nuclei at such energies can be considered transparent for each other and thus only their inner components are involved in the interaction. In heavy-ion collisions, a large number of nucleons is involved in the processes while the collision takes place in a very tight region.

Central collisions, i.e. characterized by an impact parameter[4] $b \sim 0$, involve all the protons and neutrons of the nuclei. Otherwise, in non-central collisions, the involved nucleons are called *participants* while the others *spectators*.

A schematic of the evolution of a central heavy-ion collision is provided in Fig. 1.9. The formation of QGP matter occurs if critical temperature and critical energy density are reached. If the matter produced in the impact does not meet such conditions, the system will run into a hydrodynamical evolution (Fig. 1.9, on the left). Soon after the impact there is a pre-hadronic phase in which, despite an enhancement of pressure and temperature, a real parton deconfiment does not occur. This is called pre-hadronic phase. Nucleons, however, can recombine into new hadrons that can be detected after the hadron gas phase freeze-out. In the right side of the Fig. 1.9 it is shown the evolution of the heavy-ion collision in the case of QGP formation is shown. The following distinction is thus allowed.

- **Pre-equilibrium** ($t \lesssim 1 fm/c$): partons scatter among each other and give rise to an abundant production of deconfined quarks and gluons. High transverse momentum particles ($p_T \gg 1\ GeV/c$) are produced at this stage. At energies higher than those reached by SPS, such particles can also be produced in subsequent stages. A large quantity

[4]The impact parameter $b = |\vec{b}|$ indicate the projection of the vector $\vec{b}$ defined as the distance between the centres of the two colliding nuclei in a plane transverse to the beam axis.

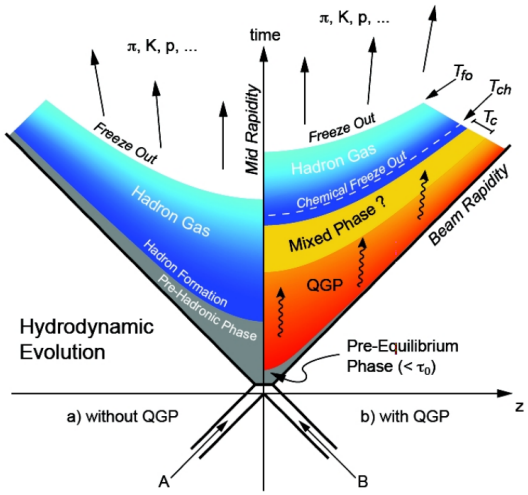

Figure 1.9: *Evolution of a central heavy ion collision in a Minkowski-like plane. The two scenarios with and without QGP are pointed out. The critical temperature is indicated by T_c, while the freeze-out and chemical freeze-out temperatures, are pointed out with T_{fo}, and T_{ch}, respectively. Rapidity and mid-rapidity will be better discussed in Sec. 1.3.*

of photons is also produced, *direct photons*, real or virtual. Virtual photons decay in lepton-antilepton pairs.

- **Thermalization** ($t \sim 1 \div 10\ fm/c$): elastic and inelastic interactions between partons in QGP lead to the thermalization phase. Inhelastic interactions can modify the flavour composition of particles. Due to its internal pressure, the system at thermal equilibrium rapidly expands. While expanding, the system begins to convert into hadron gas. This is the *mixed phase*.

- **Hadronization** ($t \sim 20\ fm/c$): during its expansion, the system cools down. When it reaches again the critical energy density, the hadronization begins and quarks and gluons of the QGP matter condensate in new hadrons. There are two possible reaction mechanisms for hadronization: *fragmentation* i.e. when a high p_T parton fragments in lower p_T hadrons and *coalescence* that involves partons with lower momenta which combines to form larger p_T hadrons. Fragmentation dominates at higher energies, while coalescence at lower ones. The energy density of the system strongly decreases and the interac-

tion region physically expands while the temperature remains stable at T_C. Hadrons continue to interact among themselves until the interaction rate can no more substain the QGP expansion. At this point the flavour composition of the QGP matter is fixed. This is called *chemical freeze-out*.

- **Thermal freeze-out**: when the mean distance between the hadrons becomes greater than the radius of strong interaction (at $T \sim 120\, MeV$), elastic scatterings between hadrons cease and kinematical spectra of the resulting matter also become fixed.

Some theoretical models predict for the pre-equilibrium and the thermalization phases the incoherent production of mini-jets that compose the plasma in a global equilibrium state. Coherent approaches, instead, predict the formation of strings of colour that decay in hadrons. At the end of the thermalization phase, the evolution of the system is ruled by relativistic hydrodynamics. Different models can be used mainly depending by the assumption of viscosity in the system.

Relative abundances are almost fixed at $T \approx T_C$. This is because hadronic cross section is strongly dominated by resonant processes, like $\pi + N \to \Delta \to \pi + N$, in which the bound state often decays in the same parent hadrons. The measure of relative abundances of quark flavours in resulting hadrons provides an evaluation of the critical temperature of the system.

Some of the characteristic parameters of the system created after ion collisions are listed in the following Table 1.1.

		CERN-SPS	BNL-RHIC	CERN-LHC
$\sqrt{s_{\rm NN}}\ (TeV)$	Centre-of-mass energy per nucleon	0.017	0.2	5.5
$\tau_0(fm/c)$	Termalization time	1	0.2	0.1
T/T_C	Reaction-critical temperature ratio	1.1	1.9	3.0 ÷ 4.2
$\epsilon\ (GeV/fm^3)$	Energy density	3	5	15 ÷ 60
$\tau_{QGP}\ (fm/c)$	Mean life of the QGP phase	≤2	2÷4	≥10
$\tau_{fo}\ (fm/c)$	Freeze-out time	∼10	20÷30	30 ÷ 40
$V_{fo}\ (fm^3)$	Freeze-out volume	$\sim 10^3$	$\sim 10^4$	$\sim 10^5$

Table 1.1: *Heavy-ion collision characteristic parameters for CERN-SPS, RHIC and CERN-LHC experiments [23].*

1.3 Experimental observables

The main experimental challenge is to build observables that allow to determine if a collision produced just an extremely dense state of standard matter (i.e. mainly made by hadrons) or if a deconfined state has been actually created. Particles that can be revealed by a detector as product of a QGP hadronization are ordinary particles (e.g. π, p, K, *etc...*), in general. Since it is impossible to directly observe free quarks and gluons, the only reasonable way to identify traces of the creation of a QGP state is the indirect approach. In addition, the equilibrium state of the QGP cannot be directly detected, as it has a lifetime of the order of 10^{-23} s. Thus, it is important to select observables that permit to probe the different phases of the QGP evolution and its properties, such as critical temperature, the order of the phase transition, sound velocity and viscosity.

Experimental evidences are traditionally subdivided in *hard probes* and *soft probes*, depending on the stage of the collision from which they emerge, and on the energy of the respective processes. Hard probes come from the interaction of high transverse momentum partons in the earlier instants of the QGP evolution. They are constituted by jets, heavy quarks and their bound states (i.e. *charmonium*, *bottomonium*), photons and direct leptons. Their study allows the building of a tomography of the QGP medium. Soft observables e.g. *strangeness enhancement*, *anisotropic flow*, *hadronic spectra*, *particle ratios*, *hadronic resonances*, typically dominate in low momentum region $p_T < 2\ GeV/c$. They are useful to give informations about collective properties of the medium and depend on the interaction between partons at lower momenta, mainly produced at the final stages of the evolution.

1.3.1 Global observables

Global observables are mainly accessible by investigating low momenta particles produced in the collision. The study of their properties allows insights into initial geometry of the collision and the evolution of the bulk matter created in heavy-ion collisions.

The properties of the bulk at the kinetic freeze-out are mainly expressed by the measured hadron spectra. At the freeze-out phase, elastic collisions are mostly ended and although the system is already cold, accurate reconstruction of the hadron spectra at kinetic freeze-out can give an amount of

informations about the earlier stages of the QGP evolution. More informations about earlier phases than the freeze-out can be deduced from the analysis of the integrated yields of the different hadron species. Inelastic collisions terminate at the chemical freeze-out (before the kinetic freeze-out) and they are the only way to change hadronic species. Particle abundances and chemical composition of the fireball revealed at this step represent a snapshot taken at the hadronization instant and then they are very weakly affected by hadronic rescattering.

Constraints about chemical reaction processes can be obtained from the study of the chemical equilibrium among hadrons. Hadrons are produced at the chemical equilibrium: if the chemical freeze-out temperature coincides with the critical temperature predicted by L-QCD, the equilibrium should have been established by the hadronization process itself i.e. the observed equilibrium cannot have been generated via hadronic rescattering due to the short timescale.

Since nuclei are extended objects, the whole dynamics of the processes depend on the centrality of the collision. The centrality of the collision is geometrically defined by the impact parameter. Even though centrality is a not directly measurable quantity, it is related to the impact parameter b of the collision and it can be determined via multiplicity measurements and inferred by comparison of data with simulations of the collisions. The centrality of a nuclear collision can also be expressed in terms of the total hadronic interaction cross-section[5] σ_{AA} that is proportional to $\pi b^2/\pi(2R_A)^2$, where R_A is the nuclear radius. Finally, centrality is experimentally expressed as a percentage of the total nuclear interaction cross-section, e.g. the 10% most central events are the 10% that have the highest particle multiplicity.

Neither the impact parameter nor the number of participants N_{part}, spectators N_{spec} or binary collisions N_{coll} are directly measurable, but they can be related to the impact parameter via Glauber model calculations. Nevertheless, experimental observables to be related to these geometrical quantities are needed [26]. One such observable is the multiplicity of the particles produced in collision in a given rapidity[6] range around mid-rapidity,

[5]The total hadronic cross-section is determinable through special runs triggering during the detector calibration. For this purpose, most heavy ion experiments are often equipped with special detectors. These devices are called event characterization detectors [24, 25].

[6]In relativistic mechanics the addition law for velocities moving along the same direction is in general not linear. Rapidity $y = tanh^{-1}\beta = \frac{1}{2}ln\left[\frac{E+p_z}{E-p_z}\right]$ is the relativistic

that increases monotonically with the impact parameter.

The centrality of a collision can be also given by the zero-degree energy, which in ALICE is measured by the ZCD subdetector (see Sec. 2.1.5). From the assumption that, on average, the particle multiplicity at midrapidity (the zero-degree energy) monotonically increases (decreases) with the overlap volume, i.e. with centrality, it is possible to obtain the following experimental relation for the centrality:

$$c \approx \frac{1}{\sigma_{AA}} \int_{N_{ch}^{thr}}^{\infty} \frac{d\sigma}{dN'_{ch}} dN'_{ch} \approx \frac{1}{\sigma_{AA}} \int_{0}^{E_{ZDC}^{thr}} \frac{d\sigma}{dE'_{ZDC}} dE'_{ZDC}. \tag{1.16}$$

The Eq. (1.16) defines the centrality as the percentile of the hadronic cross-section corresponding to a particle multiplicity above a given threshold (N_{ch}^{thr}) or equivalently an energy deposited in the ZDC detector, below a given value (E_{ZDC}^{thr}).

If the E_{ZDC} is large, the nucleus-nucleus collision was rather peripheral and a large portion of the beam energy continued without deflection. Since the cross section can be replaced with the number of observed events n, considering the trigger efficiency of the detector and the non-hadronic interaction background, one can define the parameter N_{ev}, by which the expression for the centrality c can be written as

$$c \approx \frac{1}{N_{ev}} \int_{N_{ch}}^{\infty} \frac{dn}{dN'_{ch}} dN'_{ch} \approx \frac{1}{N_{ev}} \int_{0}^{E_{ZDC}} \frac{dn}{dE'_{ZDC}} dE'_{ZDC}. \tag{1.17}$$

An illustration of the dependence of N_{part} and N_{coll} on the centrality for the LHC energy is showed in Fig. 1.10. The inelastic nucleon-nucleon cross section, σ_{AA}^{inel} acted as an input for Glauber model to perform the calculations [24, 26].

Basic global observables

Two main quantities can be considered as basic global observables: the average charged particle multiplicity per (pseudo-)rapidity unit $\frac{dN_{ch}}{dy}$ $\left(\frac{dN_{ch}}{d\eta}\right)$ (i.e. the hadron rapidity density) and the transverse energy per (pseudo-) rapidity unit $\frac{dE_T}{dy}$ $\left(\frac{dE_T}{d\eta}\right)$. Their study allows the determination of temperature, entropy, momentum spectra and energy density of the system created

analogue of the velocity for particles with small β and it is an additive quantity. Pseudo-rapidity η is defined as $\eta \equiv -ln\left(tan\frac{\theta}{2}\right)$, where θ is the polar angle between $\vec{p}$ and the z-axis. For small mass particles i.e. $E \gg m$, it is $y \approx \eta$ [25].

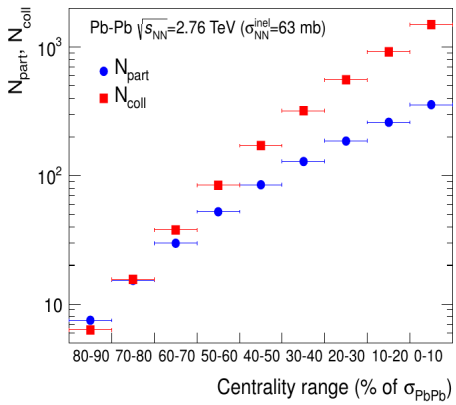

Figure 1.10: *Centrality dependence of N_{part} and N_{coll} (average values) for* Pb-Pb *collisions in the ALICE experiment at $\sqrt{2.76\ TeV}$. The total interaction cross section is $\sigma_{PbPb} = 7.7\ b$ [27]*

in a heavy-ion collision. Both these quantities involve soft processes whose effects dominate at large distance scale, where QCD becomes unsuccessful.

Multiplicity in *pp* collisions

Experiments based on proton-proton collisions have provided a great deal of information about observables and their physics. During its Operational Run 1 of data taking, the ALICE experiment studied *pp* collisions either as a benchmark for the further study in *Pb-Pb* events and to improve the knowledge about phase transition to QGP, analyzing multiplicity fluctuations. It is known that the number of particles produced does not increase proportionally to the centre-of-mass energies of the collision, from previous measurements of *pp* collisions. Instead, it scales as $ln(s)$ [25]. Figure 1.11 shows particle multiplicity as a function of the centre-of-mass energy for *pp* collisions.

Multiplicity in heavy-ion collisions

Measurements of charged hadron pseudorapidity density $\left(\frac{dN_{ch}}{d\eta}\right)$ are needed to characterize the system produced in collisions. Previous experiments evidenced that the charged particle density is scaled by the number of participating nucleons. The ALICE collaboration found the density of primary charged particles at mid-rapidity to be $\frac{dN_{ch}}{d\eta} = 1584 \pm 4(\text{stat}) \pm 76(\text{sys})$ and by normalizing for participant pair, it is $\frac{dN_{ch}}{d\eta(0.5\langle N_{part}\rangle)} = 8.3 \pm 0.4(\text{sys})$, with

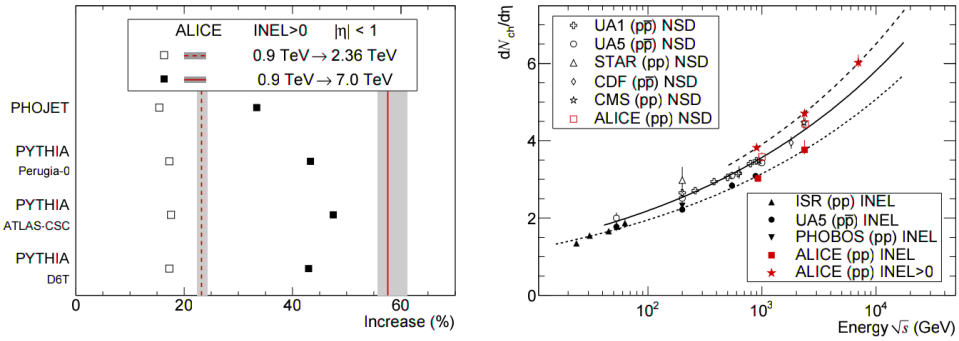

Figure 1.11: *On the left: comparison between relative increase of the charged-particle pseudorapidity density measurements in 7 TeV ALICE (dashed and solid lines) and various model predictions (open and full squares). On the right: Charged-particle pseudorapidity density as a function of the centre-of-mass energy for various experiments. Data points at the same energy have been slightly shifted horizontally for visibility [28].*

negiglible statistical error.

To compare pp collisions multiplicities to heavy-ion a parameter indicating the number of participants N_{part} is introduced. It is 2 in pp, $2A$ in central AA collisions and varies with centrality. In Fig. 1.12, such value is compared to the measurements for Au-Au and Pb-Pb, and with non-single diffractive (NSD) pp and $p\bar{p}$ collisions, over a wide range of collision energies. It can be noted that the energy dependence is steeper for heavy-ion collisions than for pp and $p\bar{p}$ collisions. The energy dependence shown in Fig. 1.12 can be described by $(\sqrt{s_{\rm NN}})^{0.3}$ for nucleus-nucleus, and $(\sqrt{s_{\rm NN}})^{0.22}$ for pp and $p\bar{p}$ collisions. For illustration, corresponding curves $\propto s_{\rm NN}^{0.15}$ and $\propto s_{\rm NN}^{0.11}$ are superimposed on the data. A significant increase, by a factor 2.2, in the pseudo-rapidity density is observed at $\sqrt{s_{\rm NN}} = 2.76\ TeV$ for Pb-Pb compared to $\sqrt{s_{\rm NN}} = 0.2\ TeV$ for Au-Au collisions studied at RHIC. This increase has been interpreted as the outcome of an increase of the initial entropy density [27]. On the right side of Fig. 1.12 it can be seen that the ALICE measurements confirmed the phenomenological $(\sqrt{s_{\rm NN}})^{0.3}$ behaviour found at lower energies. The data points are obtained by summing the $\frac{dN}{dy}$ yields for pions, kaons and protons and their antiparticles.

The centrality dependence of $\frac{dN_{ch}}{d\eta}$ found at the LHC is identical to that measured at RHIC (see Fig. 1.13). This highligths that the mechanism of particle production is the same at the two energies. The colour glass con-

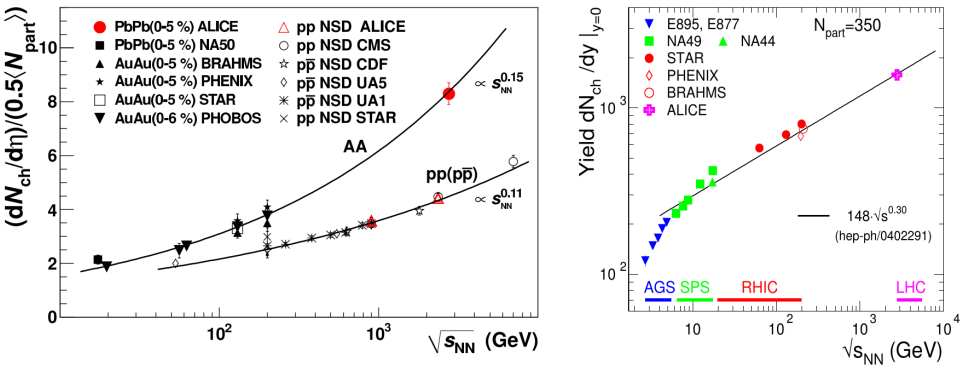

Figure 1.12: *On the left: charged particle pseudo-rapidity density per participant pair for central nucleus-nucleus and non-single diffractive* pp *and* $p\bar{p}$ *collisions as a function of* $\sqrt{s_{\rm NN}}$ *[29]. On the right: Collision energy dependence of charged-particle rapidity density (sum of pions, kaons and protons and their antiparticles) at midrapidity, measured by various experiments in central collisions corresponding to* $N_{part} = 350$ *[27].*

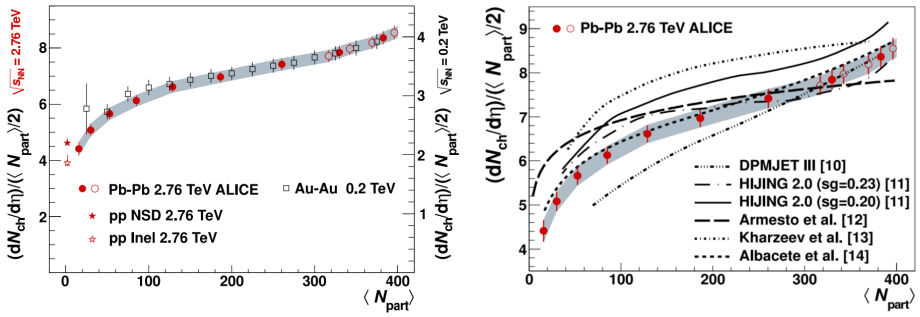

Figure 1.13: *On the left: Centrality dependence of the charged particle pseudorapidity density in* Pb-Pb *collisions at the LHC and in* Au-Au *collisions at RHIC. It is possible to appreciate the comparison for LHC and RHIC data, with the two energy scales on the two vertical axis. On the right: A comparison between* $\frac{dN_{ch}}{2d\eta\langle N_{part}\rangle}$ *measured in ALICE and corresponding predictions from various theoretical models [30].*

densate model for the parton structure of matter at low parton fractional momentum well describes the data [30].

Energy density

The energy density of the central rapidity region in the collision zone can be estimated via the Bjorken formula, that is based on the assumptions of longitudinal boost invariance and formation of a thermalized central region at an initial time τ_0

$$\epsilon(\tau) = \frac{1}{\tau S_T}\frac{dE}{dy}\bigg|_{y=0}, \tag{1.18}$$

where τ is the evaluation time, S_T is the transverse overlap area of the colliding nuclei and E is the total energy. It is possible to approximate $\frac{dE}{dy}|_{y=0}$ as

$$\frac{dE}{dy}\bigg|_{y=0} \approx \langle E_T \rangle \frac{dN}{dy}\bigg|_{y=0}, \tag{1.19}$$

in which $\frac{dN}{dy}|_{y=0}$ is the hadron multiplicity at $y = 0$ and $\langle E_T \rangle$ is the average transverse energy in the considered time interval τ. Therefore, the Bjorken formula in Eq. (1.18) can be written as

$$\epsilon(\tau) = \frac{1}{A_T}\frac{dE_T}{d\eta}\frac{1}{c\tau_0}, \tag{1.20}$$

where $A_T = \pi R^2$ is the geometric transverse area of the fireball and E_T is the transverse energy. The transverse energy density $\left(\frac{dE_T}{d\eta}\right)$, which can be measured, determines the fraction of the initial energy of the collision converted in particles revealed in the transverse direction. For typical parameters in ALICE for central *Pb-Pb* collisions ($A_T \simeq 150 fm^2$) and assuming a conservative value for the equilibrium time ($\tau_0 = 1\ fm/c$ [31]) it is possible to calculate the energy density for LHC energies: $\epsilon_{\mathsf{LHC}} = 14\ GeV/fm^3$ [32]. From ALICE measurements for the most central ($0 \div 5\%$) value of $\frac{dE_T}{dy}$, it is $\epsilon^{meas}_{\mathsf{LHC}} = 16\ GeV/fm^3$, quite close to the prediction and larger than the corresponding one at RHIC of about a factor 3. Such increase in energy density corresponds to a 30% enhancement in the temperature of the QGP produced in collisions, in comparison with RHIC at the same time after the onset of the reaction, assuming that the multiplicity is proportional to the entropy of the final state and that $\epsilon \propto T^4$ [33].

1.3.2 Hadron-spectra and chemical freeze-out

Most of the particles produced in heavy-ion collisions are soft hadrons originated in the late stages of the collision evolution (see Sec. 1.2.3). Detected hadron spectra reflect the properties of the bulk of the matter at kinetic freeze-out, providing indirect informations about the early stages of the collision. More direct informations about earlier stages can be deduced from the integrated yields of the different hadron species. Particle spectra, in fact, can be modified due to rescattering processes among hadrons that are expected to occur before the chemical freeze-out. The total yields reflect the particle abundances and thus the chemical composition of the QGP matter at hadronization. In addition, total yields are very weakly affected by hadronic rescattering. Particles produced in the fireball are in chemical equilibrium and they can be described by a statistical ensemble. In the chemical equilibrium model, the system is dealt as a grand-canonical ensemble and distribution functions are derived via the maximum entropy principle by imposing global energy, baryon and strangeness conservation, for each particle kind [34, 35].

To constrain the values of system temperature and baryon chemical potential at chemical freeze-out, measured integrated hadron yield ratios are used. The measured particle abundance ratios are fit under statistical model assumptions that the system is in thermal and chemical equilibrium and that the particle production is ruled by the chemical freeze-out temperature T_{ch} as scale parameter. Below such temperature elastic collsions cease and abundances are fixed. Other parameters in the model are the baryon and strangeness chemical potentials, μ_B and μ_S and the ad-hoc strangeness suppression factor, γ_S.

Results obtained in ALICE (Fig. 1.14) for integrated hadron yield ratios for central *Pb-Pb* collisions indicate a lower chemical freeze-out temperature $T_{ch} = (152 \pm 3)\ MeV$ than the $T_{ch} = (163 \pm 5)\ MeV$ found at RHIC. Further comparisons evidence a better agreement with prediction for p/π and Λ/π ratios and significant discrepancies for ratios involving multi-strange hadrons, like Ξ/π and Ω/π [36, 37].

A comparison between results of heavy-ion collision experiments that have worked in the last 20 years at AGS, SPS, RHIC, LHC , shows that particle yield $\frac{dN}{dy}|_{y=0}$ tends to flatten with the increasing of the centre-of-mass energy, as it can be seen in the left side of Fig. 1.15. The monotonic decrease

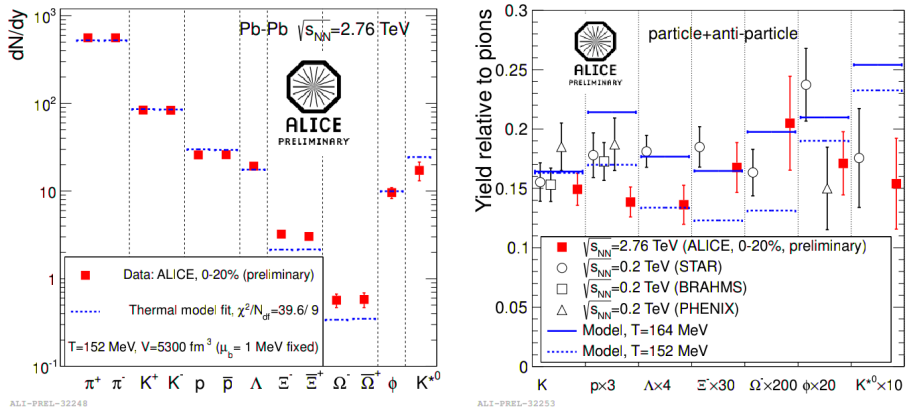

Figure 1.14: *On the left: integrated yields at mid-rapidity* $\frac{dN}{dy}$ *in central* $(0 \div 20\%)$ Pb-Pb *collisions at* $\sqrt{s_{\rm NN}} = 2.76\ TeV$ *with results from thermal fit. On the right: a comparison with RHIC results and thermal model predictions [36].*

of the proton yield indicates that as the centre-of-mass energy increases, nucleons in the colliding nuclei (or their valence u, d quarks) are stopped in the fireball. The differences in production yields of π^+ and π^- at low energies re-

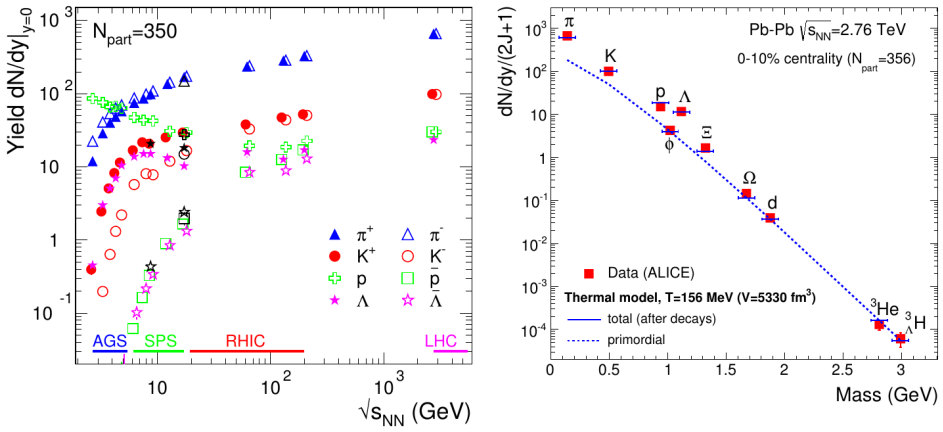

Figure 1.15: *On the left: Collision energy dependence of the multiplicities (yield,* $\frac{dN}{dy}$*, at mid-rapidity) of pions, kaons, protons and* Λ *hyperons and their antiparticles, measured in central collisions (corresponding to* $N_{part} = 350$*) of* Au *or* Pb *nuclei. On the right: Measured hadron abundances divided by the spin degeneracy factor* $(2J+1)$ *in comparison with thermal model calculations for the best fit to data in central* Pb-Pb *collisions at the LHC .*

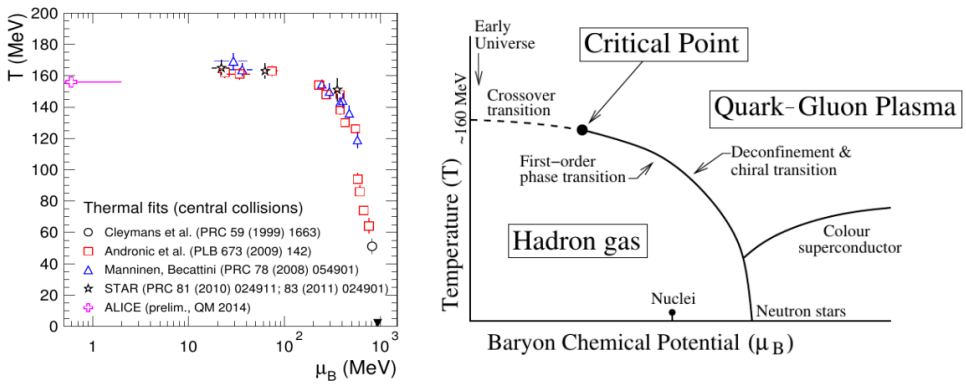

Figure 1.16: *A comparison between the phenomenological (on the left, with logarithmic scale for μ_B [27]) and the predicted (on the right [9]) QCD phase diagram.*

flect the isospin composition of the fireball. The difference between $K^+(u\bar{s})$ and $K^-(\bar{u}s)$ meson yields and $\Lambda(uds)$ and $\bar{\Lambda}(\bar{u}\bar{d}\bar{s})$ hyperon production is determined by the quark content of the hadrons. These differences vanish gradually for higher energies, where the hadrons are mostly newly created and the production yields exhibit a clear mass ordering. Figure 1.15 (on the right) shows that a good fit of hadron abundances measured in ALICE is achieved with the thermal model [38]. Remarkably, multiply-strange hyperons and (hyper)nuclei are well described by the model, which also explains [39] the equal production of matter and antimatter at the LHC [40].

Finally, in Fig. 1.16 a comparison between the phenomenological (on the left) and the predicted (on the right) QCD phase diagram is shown (cf. Fig. 1.4 in Sec. 1.2.1). Each point corresponds to a fit of hadron yields in central *Au-Au* or *Pb-Pb* collisions at a given collision energy. The agreement between the results from several indipendent analyses is remarkable. An outcome of these fits is the confirmation that T increases with increasing energy, i.e. decreasing μ_B (see Sec. 1.2.1), reaching the saturation at about 160 MeV, for $\mu_B = 300$ MeV. This saturation of T led to the connection to the QCD phase boundary, and indicates that the chemical freeze-out temperature can correspond to the hadronization temperature. The two regimes in the phase diagram (the approximately constant T for small μ_B values and the strong increase of T at large μ_B) can imply the existence of a triple point in the QCD phase diagram [27, 39].

1.3.3 Collective flow and kinetic freeze-out

A special role for the study of the properties of the QGP is played by the analysis of the collective flow in the matter created after the collision. Collective flow is a distinct feature of nucleus-nucleus collisions. Typical quantities that can be drawn from the study of the flow allow to go back to several features of the medium including mainly the viscosity and properties of the QGP thermalization. At low energy, collective flow is principally due to the nucleons in the incoming nuclei and the theoretical interpretations require the compressibility of nuclear matter or mean field effects. On the contrary, nucleon contributions are negligible at mid-rapidity, where parton effects are expected to be dominant at higher energies. The phenomenon can be described by hydrodynamical models that consider the free mean path of particles in the medium much smaller than the system size [35].

Different patterns of collective flow are taken into account in theoretical models: radial flow and anisotropic flow. The observation that the QGP is a near-perfect liquid is based on measurements of inclusive spectra (radial flow) and azimuthal anisotropy of particle production (elliptic flow) for identified hadrons at soft transverse momenta (p_T), up to about 3 GeV/c. This is further confirmed by comparison to model calculations based on viscous relativistic hydrodynamics

Radial flow and kinetic freeze-out

Radial flow consists in the emission of particles from the fireball. In central collisions i.e. when the overlap region of the two spherical nuclei is symmetric in azimuth there is only a radial component in the flow. In such case, outgoing particles are produced isotropically on the transverse plane. If the collision is not perfectly central, elliptic components arise. Pressure gradients lead to azimuthally symmetrise the fireball that becomes almost spherical. In addition, the random thermal motion contribution has to be considered. Transverse momentum distributions of radial flow present a soft component ruled by an exponential law, and a hard part governed by a power law. To quantify typical characteristics of the radial flow such as the temperature and the average transverse velocity $\langle\beta_T\rangle$, the transverse momentum p_T spectra are fitted with theoretical models. One of the most accredited models is the blast-wave model, which provides a convenient description of the thermal component of empirical hadron (and/or parton) spectra [41].

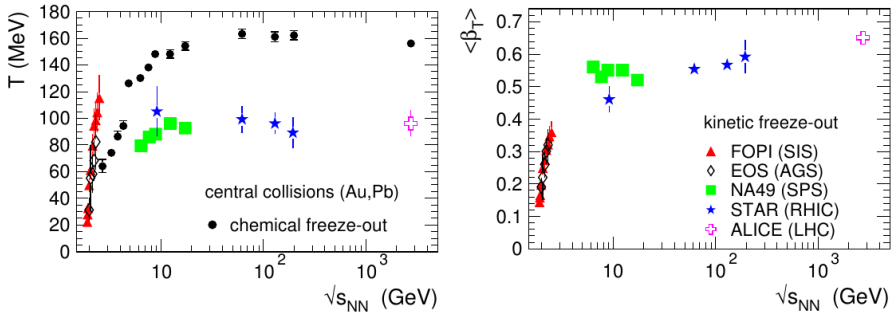

Figure 1.17: *Collision energy dependence of collective radial flow in central collisions, quantified by the temperature T and average velocity $\langle\beta_T\rangle$ at kinetic freeze-out. The temperature at chemical freeze-out is represented by the dots [27].*

It also gives bulk properties of the fireball at kinetic freeze-out. The extracted fit parameters are shown in Fig. 1.17 as a function of the collision energy. Data points are obtained from several experiments that worked so far, including STAR at the RHIC and ALICE at the LHC. At low energies, a strong increase of both T and $\langle\beta_T\rangle$ is found. A small further increase of $\langle\beta_T\rangle$ can be seen for $\sqrt{s_{\rm NN}} \gtrsim 5\ GeV$. At LHC energies $\langle\beta_T\rangle$ reaches the value $\langle\beta_T\rangle \simeq 0.65c$ with a corresponding temperature for the kinetic freeze-out of $(T_{kin} = (95 \pm 10)\ MeV)$, which is about $(50 \div 60)\ MeV$ lower than value found for the chemical freeze-out. At lower energies, the chemical freeze-out temperature is smaller than the kinetic one, which is unphysical and awaits a resolution [27, 40].

Anisotropic flow and valence quarks

Non-central collisions outline asymmetric overlap regions that produce an irregular shape bulk of initial interaction. As the system expands, the bulk tends to spherical symmetrise by pressure gradients contribution. When nuclei collide with non-zero impact parameter, the overlap region is not isotropically perpendicular to the beam axis but it rather takes an *almond* shape, which varies depending on the centrality. If in the overlap region particles are subjected to rescattering and if the phenomenon is strong *enough*, the spatial anisotropy is converted in momentum anisotropy whose effects are spread over further stages of QGP evolution and then they can be detected. The flow pattern can be quantified by analyzing the particle production in the transverse plane with respect to the reaction plane, which is defined by

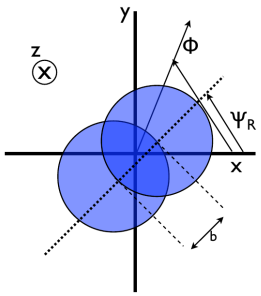

Figure 1.18: *An illustration of the reference system for collective phenomena in relativistic heavy-ion collisions [42].*

the shorter axis of the almond. The asymmetry in this distribution can be decomposed into Fourier components of the density distribution

$$E\frac{d^3N}{d^3p} = \frac{1}{2\pi}\frac{d^2N}{p_T dp_T dy}\left(1 + \sum_{n=1}^{\infty} \nu_n cos[n(\phi - \Psi_n)]\right) \tag{1.21}$$

where E indicate the energy of the particle, ϕ is the azimuthal angle of particle and Ψ_n the azimuthal orientation of the reaction plane and ν_n are the Fourier (or flow) coefficients, depending on p_T, y and centrality. It is worthy to note that the azimuthal orientation of the reaction plane can vary for different coefficients ν_n and that they can be calculated via the following relation

$$\nu_n(p_T) = \langle cos[n(\phi - \Psi_n)]\rangle. \tag{1.22}$$

The ν_n coefficients give indications about the hydrodynamic evolution of the plasma and in addition they allow estimates on the shear viscosity of the produced medium. Isotropic emissions are indicated by the condition $\nu_n = 0, \forall n$. Otherwise, non-zero values of such coefficients indicate the anisotropic flow. The ν_1 armonic represents the direct flow of particles from the fireball. It is directional and presents opposite signs in the two emispheres. The second armonic characterizes the ellipticity of the azimuthal distribution of the produced particles and thus, ν_2 represents the elliptic flow. Further armonics ν_3 and ν_4 indicate fluctuactions from initial conditions and represent triangular and quadrangular flows, respectively [43].

Large elliptic flow has been observed at RHIC. Theoretical models based on ideal relativistic hydrodynamics with a QGP equation of state and zero shear viscosity reasonably well describe the data but fail to describe elliptic

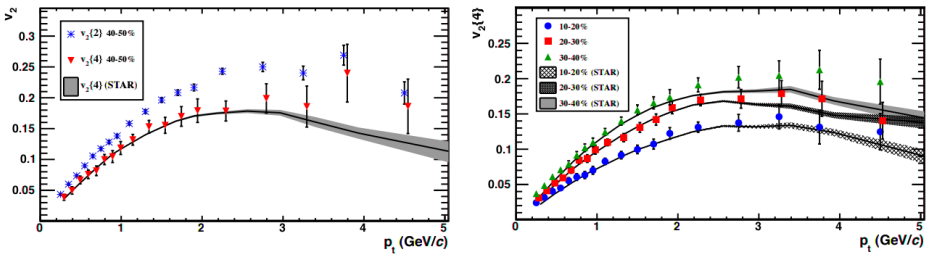

Figure 1.19: *On the left: The $\nu_2(p_T)$ coefficient for the centrality bin $(40 \div 50)\%$ in the ALICE experiment from 2- and 4- particle cumulant methods and comparison with the STAR measurements for* Au-Au *collisions. On the right: $\nu_2(p_T)\{4\}$ for various centralities compared to STAR measurements. The data points in the $(20 \div 30)\%$ centrality bin are shifted in p_T for visibility [44].*

flow measurements at lower energies ($\lesssim 2\ GeV$). For higher energies hard processes become dominant: jets and high energy hadrons leave the medium without interacting in re-scattering processes. Elliptic flow measurement in different centrality classes for particles with $|\eta| < 0.8$ have been made up in the ALICE experiment. Results of cumulant data analysis with two and four particles (respectively $\nu_2\{2\}$ and $\nu_2\{4\}$) in the centrality class $(40 \div 50)\%$ are shown in the left side of Fig. 1.19. The shaded area indicates the STAR results in Au-Au collisions at $\sqrt{s_{\rm NN}} = 200\ GeV$. It can be inferred that the value of $\nu_2(p_T)$ does not change within uncertainties from $\sqrt{s_{\rm NN}} = 200\ GeV$ to $2.76\ TeV$. On the right, $\nu_2(p_T)$ obtained with the 4-particle cumulant method for three different centralities is shown, in comparison with STAR measurements. The transverse momentum dependence is qualitatively similar for all three centrality classes. At low p_T there is agreement of $\nu_2(p_T)$ with STAR data within uncertainties. In Fig. 1.20 (on the left) the ALICE integrated elliptic flow as a function of centrality is shown. Data indicate that ν_2 increases varying from central to peripheral collisions, reaching a maximum in the $(50 \div 60)\%$ centrality class ($\nu_2\{2\}$) and $(40 \div 50)\%$ $\nu_2\{4\}$. On the right side, the integrated elliptic flow for the $(20 \div 30)\%$ centrality class is displayed, in comparison with results of previous experiments. As it can be noted, the elliptic flow enhances as the energy increases. The existence of triangular and quadrangular flows has been also verified [45]. In comparison to the elliptic flow measured at STAR at $\sqrt{s_{\rm NN}} = 200\ GeV$ an enhancement in the magnitude of about the 30% for ν_2 is observed in

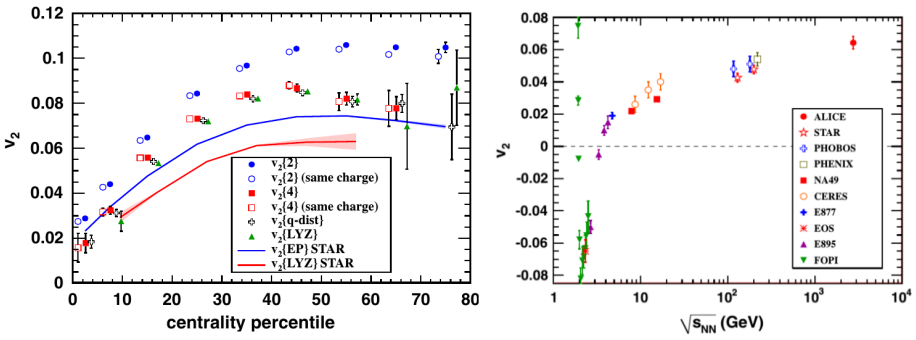

Figure 1.20: *On the left: integrated elliptic flow in the* $p_T = (0.2 \div 5.0)\ GeV/c$ *range as a function of centrality. On the right: comparison between integrated elliptic flow at* $2.76\ TeV$ *for* Pb-Pb *collisions in ALICE in the* $(20 \div 30)\%$ *centrality class and other experiments results at analogue centralities [44].*

ALICE at $\sqrt{s_{\rm NN}} = 2.76\ TeV$. Such increase is larger than in current ideal hydrodynamic calculations at LHC multiplicities but it is in agreement with some models that include viscous corrections which becomes less important at the LHC [44].

A feature of the anistropic flow obserbed initially at RHIC was the scaling of the elliptic flow with the number of constituent quarks, at intermediate values of transverse momenta $p_T = (2 \div 5)\ GeV/c$ that has been discovered at RHIC. The effect observed at LHC is smaller than a RHIC. As a qualitative idea, if the elliptic component of the particle flow has been generated in the QGP phase, detected hadrons will present a contribution in their motion depending on p_T/n. Then, particles tend to group in accordance with their hadron type i.e. baryon and meson. This so-called number of constituent quark scaling of ν_2 has been interpreted as an evidence that quark degrees of freedom dominate in the early stages of heavy-ion collisions when collective flow develops [46]. Figure 1.21 shows the elliptic flow of identified particles scaled with the constituent number of quarks, n_q (2 for mesons and 3 for baryons) as a function of p_T for different centrality classes. The effect is smaller than at RHIC, in particular for high centrality pp collisions. As consequence, this open question can lead to a reconsideration of coalescence models for quarks in hadrons during the QGP thermalization phase, maybe introducing differences between baryons and mesons.

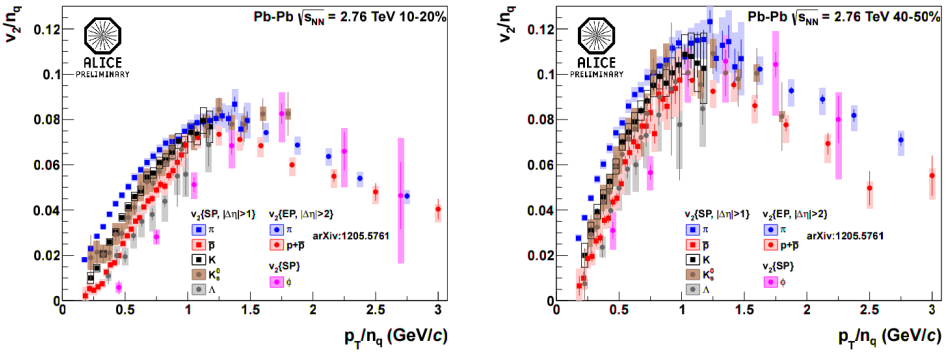

Figure 1.21: *Identified particle $\nu_2(p_T)$ scaling with the constituent number of quarks n_q vs $\frac{p_T}{n_q}$ for $(10 \div 20)\%$ (on the left) and $(40 \div 50)\%$ (on the right) centrality classes [47].*

Strangeness enhanchement

The initial strangeness content of colliding nuclei is typically very low as there is no net strangeness in the ordinary matter. Anyway, the strangeness production in collisions is expected to increase in the formation of the QGP as it was proposed already in the early 1980s [48]. The production of s quarks in fact, was supposed to take place not only in the early stages of the collision but even during the plasma phases due to the interaction of gluons. The production of new u and d quarks would be suppressed due to the Pauli's exclusion principle and then the production of s quarks would be favoured for the same quantum state. In addition, the production threshold in the deconfined medium is expected to be of the same order of the plasma temperature ($2m_s \sim 300\ MeV$, $T_C \sim 200\ MeV$) and then the production of s quarks should be favoured by the dynamics of the system. The increase of the number of strange particles, in fact, is observable in π/K abundance ratio and in the yield measurements of strange particles like the ϕ ($s\bar{s}$) meson or Ξ (sqq), Λ (uds) and Ω (sss) hyperons, whose production should be enhanched by recombination mechanisms (*coalescence*) during the chemical freeze-out phase.

Past experiments such as those at SPS and RHIC already reported an increase in the production of strange particles in relativistic heavy ion collision experiments. Due to their short lifetime, the detection of particles containing heavy quarks is particurlarly challenging. Thus, except for the

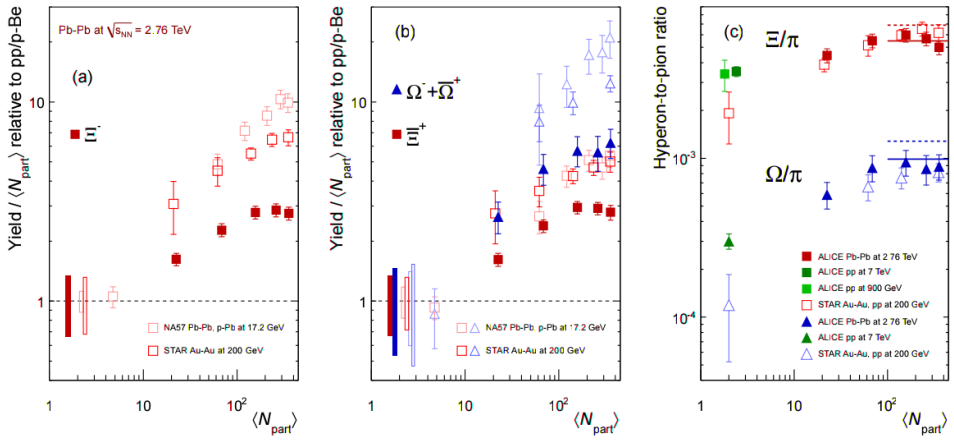

Figure 1.22: *(a), (b): enhancements in the rapidity range* $|y| < 0.5$ *as a function of the mean number of participants* $\langle N_{part} \rangle$*, showing LHC (ALICE, full symbols), RHIC and SPS (open symbols) data. Error bars on the data points represent the corresponding uncertainties for all the heavy-ion measurements and those for* p-Pb *at the SPS. (c) Hyperon-to-pion ratios as a function of* $\langle N_{part} \rangle$*, for* A+A *and* pp *collisions at LHC and RHIC energies. The lines mark the thermal model predictions [49].*

charged kaons, the strange particles are identified by their decay products. Strangeness enhancements have indeed been observed by comparing central heavy-ion collisions with *p-Be* and *pp* collisions both at the SPS and at RHIC. Over the past 15 years, it has been found that the hadron yields in central heavy-ion collisions follow the expectation for a grand-canonical ensemble, increasingly well as a function of the collision energy, indicative of a system in equilibrium. At the same time it was understood that, for *pp* collisions, canonical suppression effects are important and account for the overall hyperon enhancement. In Fig. 1.22, enhancement for $\Xi^{\pm}$ and $\Omega^{\pm}$ hyperons in *Pb-Pb* collisions at $\sqrt{s_{\rm NN}} = 2.76\ TeV$ in ALICE as a function of the number of participants and in comparison with the previous experiments results are shown. The enhancements are larger than unity for all the particles. They increase with the strangeness content of the particle, showing the hierarchy already observed at lower energies and also consistent with the picture of enhanced $s\bar{s}$ pair production in a hot and dense partonic medium. In addition, the same shape and scale are observed for baryons and anti-baryons, as expected because of the vanishing net-baryon number at the LHC energy. In comparison with other experiments, the enhancements are found to decrease

with increasing centre-of-mass energy, continuing the trend established at lower energies. The hyperon-to-pion ratios for N+N and pp collisions both at LHC and RHIC energies, are shown in the right side of Fig. 1.22 as a function of $\langle N_{part} \rangle$. They indicate that different mechanisms contribute to the evolution with centrality of the enhancements as defined above. Indeed, the relative production of strangeness in pp collisions is larger than at lower energies. The yields have been measured to be larger than at RHIC while the hyperon-to-pion ratios are similar at the two energies, rising with centrality and showing a saturation at $\langle N_{part} \rangle \sim 150$. The values of those ratios for central collisions are found compatible with recent predictions from thermal models. The enhancements relative to pp increase both with the strangeness content of the baryon and with centrality, but are less pronounced than at lower energies [49].

1.3.4 Electromagnetic probes

Electromagnetic signals, i.e. photons and dileptons constitute particularly significant probes in the study of the dynamics of the QGP in the very early instants of its formation. Photons and leptons do not interact with the color field. The coupling constant α_{EM} is smaller than α_S and the medium appears as almost transparent. A greatly important signal is given by the thermal radiation emitted by the QGP via the $q\bar{q}$ annihilation that permits a direct measurement of temperature of the plasma. In addition, thermal radiation constitutes a direct mark of what has been produced in the collision and it can be considered as a strong signal of deconfinement. Anyway, the separation of direct electromagnetic signals from the background due to subsequent processes ($\pi^0 \to \gamma\gamma,\ \eta \to \gamma\gamma$) is difficult.

Photons

Photons are produced at different stages of a heavy-ion collision. At first stages of the collision, *prompt* photons are produced from parton-parton scatterings due to first to nucleus-nucleus collisions and then to nucleon-nucleon ones. In the following stage, quark-gluon plasma is expected to form and photons to be emitted from quarks which collide with gluons and other quarks of the medium. Then, the system expands and cools down. At the hadronization, photons are produced either in the scattering of the produced particles (π, ρ, ω and so on) or in resonances and π^0 decays. This

mechanism survives until the resonances cease to interact. The energy of these photons ranges from a few hundred MeV to several GeV. Finally, once the kinetic freeze-out is also reached, the photon production is mainly due to resonance decays and the spectrum extends up to few hundred MeV. By distinguishing photons emitted during the QGP phases from the background, it is possible to investigate thermal photons emitted during the hadronization at the thermalization of the system. Measurements of thermal photons at RHIC have shown that the temperature averaged over the lifetime of the fireball is larger than the chemical freeze-out T [50]. A somewhat larger value $T_{\mathsf{LHC}} = (304 \pm 51(syst + stat))\ MeV$ is extracted from preliminary data of photon production at the LHC [51].

Dileptons

As well as photons, dileptons constitute an important tool for measuring the properties of the matter produced in relativistic heavy-ion collisions. Lepton-pair production is similar to the creation of photons i.e. there are prompt contributions from the hard nucleon-nucleon collisions, thermal radiation from the quark-gluon plasma and the hot hadronic phase, as well as final-state interactions and meson decays (Dalitz decays: $\pi^0 \to e^+e^-\gamma$) after freeze-out. Like the case of photons, dileptons do not have strong interactions with the medium. The prompt contribution to the continuum in the dilepton mass range above pair mass $m \sim 2\ GeV$ is dominated by semileptonic decays of heavy-flavour mesons and by the Drell-Yan process and it can be calculated in perturbative QCD. The experimental task, then, is the discrimination of thermal radiation from the large prompt background, like in the case of photon detection.

1.3.5 High transverse momentum measurements

Measurements at RHIC showed that hadron production at high transverse momentum p_T in head-on Au-Au collisions at a centre-of-mass energy per nucleon pair $\sqrt{s_{\mathrm{NN}}} = 200\ GeV$ is suppressed by a factor $4 \div 5$ if compared to expectations from independent superposition on nucleon-nucleon collisions. High p_T hadrons are mainly produced via the fragmentation of high p_T partons that originate in hard scatterings at early stages of nuclear collisions. The observed suppression at RHIC is generally attributed to energy loss of the partons as they propagate through the hot and dense QCD

medium. To quantify nuclear medium effects at high transverse momentum, the *nuclear modification factor* is defined as

$$R_{AA}(p_T) = \frac{\frac{1}{N_{evt}^{\mathrm{AA}}} \frac{d^2 N_{ch}^{\mathrm{AA}}}{d\eta dp_T}}{\langle N_{coll} \rangle \frac{1}{N_{evt}^{pp}} \frac{d^2 N_{pp}^{ch}}{d\eta dp_T}}, \tag{1.23}$$

where the number of binary nucleon-nucleon collisions $\langle N_{coll} \rangle$ is given by the product of the nuclear overlap function T_{AA} and the inelastic nucleus-nucleus cross section σ_{inel}^{NN}. It represents the ratio of the charged particle yield in *Pb-Pb* to that in *pp*, scaled by the number of binary nucleon-nucleon collisions. Thus, if no nuclear modification is present, $R_{AA} = 1$ at high p_T. A larger energy loss of high p_T partons was awaited at the LHC, since a larger density of the medium was expected due to higher energy. On the other hand, since the transverse momentum spectra decreases more slowly, a smaller suppression in the p_T spectrum of charged particles for a given magnitude of partonic energy loss could be reasonable. As a further issue to consider, the value of R_{AA} in central collisions and its p_T dependence may also, in part, be influenched by gluon shadowing and saturation effects, which in general decreases with increasing $x = \frac{2p_T}{\sqrt{s}}$ and Q^2. In order to calculate the nuclear modification factor for collisions at a given energy, a *pp* reference measurement at the same energy is needed.

The first measurements of R_{AA} for charged hadron production at the LHC showed that the suppression is larger than at RHIC.The suppression is reduced towards larger p_T values. Figure 1.23 (on the left) shows R_{AA} for central and peripheral *Pb-Pb* collisions. In both cases the nuclear modification factor deviate from the unity. At high p_T, where production from hard processes is expected to dominate, there is a marked difference between peripheral and central events. In peripheral collisions, R_{AA} reaches about 0.7 and no evident p_T dependence for $p_T > 2$ GeV/c is shown. In central collisions, R_{AA} is again significantly different from one, reaching a minimum of $R_{AA} \simeq 0.14$ at $p_T = (6 \div 7)$ GeV/c. In the intermediate region there is a strong dependence on p_T with a maximum at $p_T = 2$ GeV/c. This may reflect a variation of the particle composition in heavy-ion collisions with respect to *pp*, as observed at RHIC. A significant rise of R_{AA} by about a factor of two is observed for $p_T = (7 \div 20)$ GeV/c. The plot shows, for central collisions only, the result for R_{AA} at $p_T > 6.5$ GeV/c using alternative *pp* references obtained by the use of a $p\bar{p}$ measurement at $\sqrt{s_{\mathrm{NN}}} = 1.96$ TeV

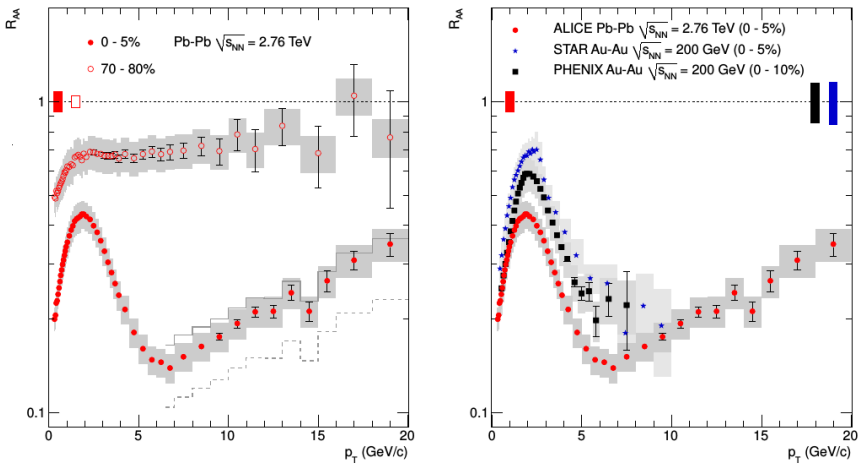

Figure 1.23: *On the left:* R_{AA} *for central and peripheral collisions at* $\sqrt{s_{\mathrm{NN}}} = 2.76\,TeV$. *Bars indicate statistical uncertainties, while shaded boxes contain systematic errors in the data and the* p_T *dependent systematic errors on the* pp *reference, added in quadrature. On the right: comparison of* R_{AA} *in central* Pb-Pb *collisions at LHC to measurements at* $\sqrt{s_{\mathrm{NN}}} = 200\,GeV$ *by the PHENIX and STAR experiments at RHIC [52].*

(dashed line). For such scenarios, the overall value for R_{AA} is shifted, but a significant increase of R_{AA} in central collisions for $p_T > 7\ GeV/c$ persists. On the right side of Fig. 1.23, the ALICE result in central *Pb-Pb* collisions at LHC is compared to measurements of R_{AA} of charged hadrons at $\sqrt{s_{\mathrm{NN}}} = 200\ GeV$ by the PHENIX and STAR experiments at RHIC. At low energies ($\sim$1 GeV/c) the measured value of R_{AA} is similar to those from RHIC. The position and shape of the maximum at $p_T \sim 2\ GeV/c$ and the subsequent decrease are similar at RHIC and LHC, contrary to expectations from a recombination model. Despite the much flatter p_T spectrum in *pp* at the LHC, the nuclear modification factor at $p_T = (6 \div 7)\ GeV/c$ is smaller than at RHIC. This suggests an enhanced energy loss at LHC and therefore a denser medium. A quantitative determination of the energy loss and medium density will require further investigation of gluon shadowing and saturation in the present energy range and detailed theoretical modeling [52].

Data for *p-Pb* collisions at the LHC demonstrate that the suppression of hadron production at high p_T in *Pb-Pb* collisions, has no contribution from initial state effects. The ALICE *p-Pb* data show no nuclear matter

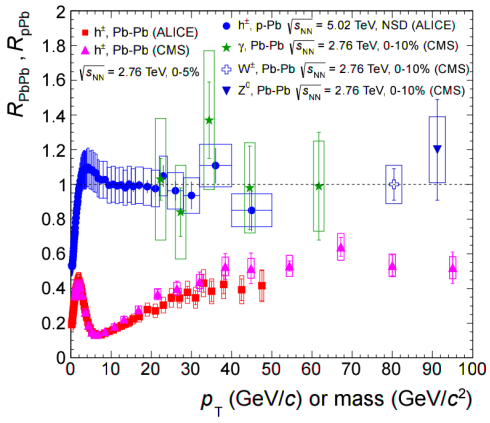

Figure 1.24: *Transverse momentum dependence of the nuclear modification factor* $R_{\text{p-Pb}}$ *of charged particles* ($h^{\pm}$) *measured in minimum-bias (NSD) p-Pb collisions at* $\sqrt{s_{\text{NN}}} = 2.76\ TeV$ *in comparison to data on the nuclear modification factor* $R_{\text{Pb-Pb}}$ *in central Pb-Pb collisions at* $\sqrt{s_{\text{NN}}} = 2.76\ TeV$. *The Pb-Pb data are for charged particle direct photon,* Z^0 *and* $W^{\pm}$ *production. All data are for midrapidity [53].*

modification of hadron production at high p_T and therefore they are fully consistent with the observation of binary collision scaling in *Pb-Pb* of observables which are not affected by hot QCD matter (direct photons and vector bosons). The nuclear modification factor for *p-Pb* collisions is defined as

$$R_{p\text{-}Pb}(p_T) = \frac{\frac{d^2 N_{ch}^{p\text{-}Pb}}{d\eta dp_T}}{\langle T_{p\text{-}Pb} \rangle \frac{d^2\sigma^{pp}}{d\eta dp_T}}, \tag{1.24}$$

where $N_{ch}^{p\text{-}Pb}$ is the charged particle yield in *p-Pb* collisions. The results covering the $p_T = (0.15 \div 50)\ GeV/c$ range, exhibit, within uncertainties, no deviation from binary collision scaling at high p_T; the nuclear modification factor remains consistent with unity for $p_T \gtrsim 2\ GeV/c$. The data at high p_T confirm the earlier observation that initial state effects do not contribute to the strong suppression of hadron production at high p_T observed at the LHC in *Pb-Pb* collisions. The measurements, in conjunction with theoretical models, clearly demonstrate that partons lose energy in the deconfined hot and dense matter created in collisions at RHIC and LHC. The basic features seen in the data are reproduced by theoretical models [53].

1.3.6 Jet quenching

One way to characterize the properties of the QGP is to use partons from the hard scattering of the partonic constituents in the colliding nucleons as medium probes.

High transverse momentum particles are expected to be produced in early stages of collision evolution and then to propagate through the expanding medium. Hard partons eventually fragment and produce jets of hadrons. High p_T partons reduce their energy, if compared with pp collisions, while interacting with the hot and dense QGP medium. Accredited theories suggest that the dominant energy-loss mechanism is radiative i.e medium-induced gluon radiation (*gluonsstrahlung*) rather than collisional [54]. In relation to these studies, partons radiate gluons and the parton energy loss grows quadratically with the in-medium path length. Besides the reduction of the high p_T particle yield, jet quenching effects are several and their measurements can give more informations about the system. Because of the dependence on the impact parameter of the collision, jet quenching should be larger in central collisions. The p_T spectra of jets made of c and b quarks reveal possible medium modifications of the heavy quark fragmentation functions.

Jets are usually reconstructed by grouping measured particles within a given distance. The interaction with the medium can result in a broadening of the jet shape, a softening of the jet fragmentation leading to an increase of out-of-cone gluon radiation with respect to jets reconstructed in pp collisions. Therefore, for a given jet radius parameter R and a fixed initial parton energy, the energy of jets reconstructed in heavy-ion collisions is expected to be smaller than those reconstructed in pp collisions.

Jet quenching has been observed at RHIC and at the LHC via the measurement of inclusive hadron and jet production at high p_T, di-hadron angular correlations and the di-jet energy imbalance. In all cases, the measured observable is found to be strongly modified in central heavy-ion collisions with respect to pp collisions, when compared to expectations based on treating heavy-ion collisions as an incoherent superposition of independent nucleon-nucleon collisions.

Results from ALICE measurements in the $(0 \div 10)\%$ and $(10 \div 30)\%$ central Pb-Pb collisions are reported in Fig. 1.25. The signal jets were obtained using the anti-k_T jet algorithm with a resolution parameter of $R =$

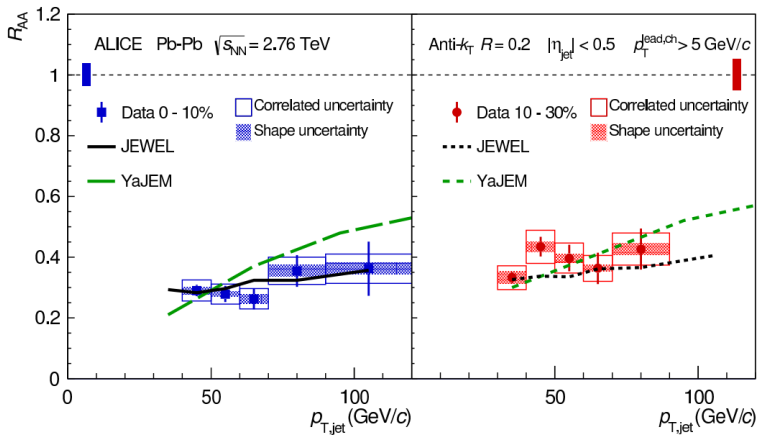

Figure 1.25: R_{AA} *for* $R = 0.2$ *jets with the leading track required of* 5 GeV/c *of in* $(0 \div 10)\%$ *(on the left) and* $(10 \div 30)\%$ *(on the right) most central* Pb-Pb *collisions compared to expectations from two jet quenching model calculations with different approaches [55].*

0.2 in the pseudorapidity range of $|\eta_{jet}| < 0.5$. Signal jets were required to contain at least one charged particle with $p_T > 5\ GeV/c$. As it can be seen, jets in the measured $p_{T,jet}$ range are strongly suppressed. The average R_{AA} in both $(0 \div 10)\%$ and $(10 \div 30)\%$ central events was found to have a negligible p_T, jet dependence. In the 10% most central events, combining the statistical and systematic uncertainty in quadrature, the average R_{AA} is found to be 0.28 ± 0.04. The suppression is smaller in magnitude in the $(10 \div 30)\%$ central events, leading to an average R_{AA} of 0.35 ± 0.04. The systematic and statistical uncertainties from the *Pb-Pb* and *pp* measurements are added in quadrature. The observed suppression is in fair agreement with expectations from two model calculations with different approaches to jet quenching [55].

1.3.7 Heavy quarks

Heavy quarks constitute a significant probe for the QGP. While interacting with the medium, heavy quarks lose energy until they reach sufficiently low transverse momentum to thermalize. Reinteractions will reflect in the p_T spectra and, in particular, in the elliptic flow in semi-central collisions. Thus, the study of heavy flavour particle interactions with the QGP medium could allow to understand how the thermalization and the hadronization of heavy quarks take place and the energy losses of heavy quarks in the QGP

medium, in relation to their masses. Heavy quarks are produced soon after the collision in hard parton scatterings. Typical processes are $q\bar{q} \rightarrow Q\bar{Q}$ and $gg \rightarrow \bar{Q}Q$, where lower case q indicates small mass quarks belonging to the incoming nucleus and uppercase Q indicates heavy quarks eventually created after collisions. For these processes, the transferred momentum must be larger than $2m_Q$. Heavy quarks, then, are produced on short timescale ($\sim\frac{1}{m_Q}$) but they can survive during the QGP phase due to their relatively long lifetime. Charm and bottom quarks can live through the thermalization phase and can be affected by the presence of the QGP medium. Once the quark-gluon plasma was created, the presence of free colour charge is expected to screen the binding colour potential leading to the dissolution of quarkonium states. This is because the binding energies are comparable in size to the mean plasma energy ($\sim 3T_c$) [56]. Open heavy flavour states (i.e. having c or b quark as costituent) result from the creation of a a $q\bar{q}$ pair that brings to the creation of a pair of mesons, one containing the heavy quark plus an light antiquark and the other containing the parent antiquark plus a light quark. For example, the D meson family contains a charm quark plus one of the light antiquarks, i.e., up, down, or strange. Their study assume an important role in the physics of QGP.

J/ψ suppression

The J/ψ meson (i.e. the bound state of c and $\bar{c}$ quarks) was one of the first signals to be proposed for the study of QGP states, since it is the first hadron for which a clear mechanism of suppression in QGP was proposed, based on the colour analogue of Debye screening. Further observations, including the whole quarkonia species, $c\bar{c}$ and $b\bar{b}$, led to a new picture of the so-called "sequential suppression", a hierarchy of quarkonium dissociation dependent on the binding energy of the quarkonium state which could give information on the temperature of the medium. In the statistical hadronization model, the charm quark produced in initial hard collisions thermalize and recombine into new hadrons at chemical freeze-out. All charmonium states are assumed to be not formed at all in the deconfined state but they are produced, toghether with all other hadrons, at chemical freeze-out. An alternative production mechanism for quarkonium is the kinetic recombination of charm and anti-charm quarks in QGP. In this model, continuous

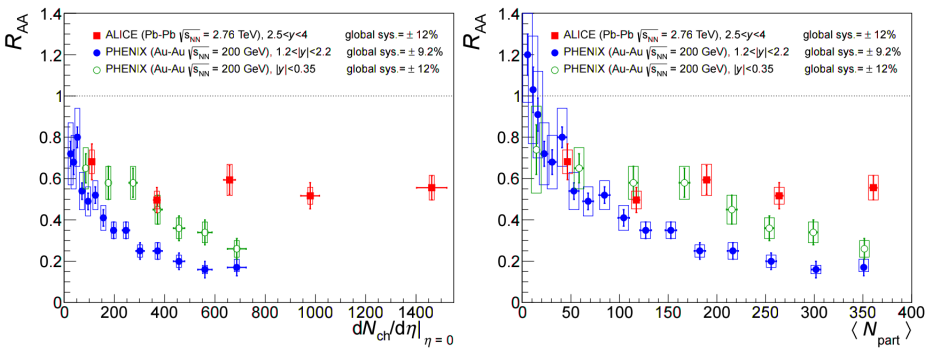

Figure 1.26: *R_{AA} obtained by the ALICE experiment in the range $y = 2.5 \div 4$ and for $p_t \geq 0$ as a function of $\frac{dN_{ch}}{d\eta}|_{\eta=0}$ (left) and of $\langle N_{part} \rangle$ (right). In both the plots a comparison with the PHENIX results in* Au-Au *collisions at $\sqrt{s_{\rm NN}} = 200\ GeV$ at mid-rapidity and forward rapidity is shown [57].*

dissociation and regeneration of charmonium takes place over the entire lifetime of the deconfined stage [27].

In the two past decades, J/ψ production in heavy-ion collisions was intensively studied at the SPS and at the RHIC in the $(20 \div 200)\ GeV$ range of centre-of-mass energy per colliding nucleon pair. A strong suppression was found in the most central *Pb-Pb* collisions, at the SPS. A possible interpretation of the observed suppression is the dissociation of excited $c\bar{c}$ states, (e.g. χ_c and $\psi(2S)$) that constitute about 40% of the inclusive J/ψ yield in *pp* collisions. A suppression for the J/ψ was also observed at RHIC, in central *Au-Au* collisions, at a level similar to the one observed at the SPS when measured at mid-rapidity although it is larger at forward rapidity.

The measurement of J/ψ production in *Pb-Pb* collisions at the LHC was expected to provide a definitive answer on the question of regeneration. The J/ψ R_{AA} measured in ALICE at $\sqrt{s_{\rm NN}} = 2.76\ TeV$ is larger than the one measured at the SPS and at RHIC for most central collisions and does not exhibit a significant centrality dependence. Figure 1.26 shows the results for R_{AA} obtained by ALICE in the range $y = 2.5 \div 4$ and for $p_t \geq 0$, as a function of $\frac{dN_{ch}}{d\eta}|_{\eta=0}$ (left) and of $\langle N_{part} \rangle$ (right). The charged-particle density closely relates to the energy density of the created medium whereas the number of participants reflects the collision geometry. The centrality integrated J/ψ R_{AA} is $R^{0\% \div 80\%} = 0.545 \pm 0.032(stat) \pm 0.083(syst)$, indicating a clear J/ψ suppression [57]. This is confirmed by more recent data [58]. The data are

well described by both the statistical hadronization model and transport models. The quarkonium data at the LHC demonstrate that regeneration in deconfined matter during the QGP lifetime or at the chemical freeze-out are the only possible mechanisms of production.

The study of the Λ_C and of the Λ_C/D^0 ratio

The distribution of heavy quarks at the moment of their creation is isotropic in azimuthal direction, then, a non-zero ν_2 value of heavy-flavour mesons can only arise from interactions between the QGP medium and the heavy quarks. Anisotropy is detected by measuring the momentum-dependent azimuthal distribution of the produced particles with respect to the reaction plane and it is quantified by the second coefficient of the Fourier expansion of the azimuthal distribution, ν_2 (see Sec. 1.3.1). A measurement of the ν_2 coefficient for D^0, D^+ and D^{*+} in semi-central Pb-Pb collisions was obtained by ALICE using about 10^7 events from the 2011 run [59]. This non-zero ν_2 suggested that D mesons may take part in the flow dynamics. Anyway, at RHIC, it was found that ν_2 of identified particles scales with $m_T - m_0$ for $p_T < (1 \div 2)\ GeV/c$. The same behaviour is observed also at LHC. At higher p_T, a correlation with the number of constituent quarks n_q was reported. A powerful test of the level of in-medium thermalization of charm and beauty quarks would be to verify whether this universal scaling continues to hold also for heavy-flavour mesons and baryons. This requires measuring the D meson and Λ_C elliptic flow in the range $(2 \div 5)\ GeV/c$, where the baryon/meson (Λ/K) ratio measured at RHIC is most pronounced. Excess of baryons with respect to mesons suggests hadronization via coalescence of constituent quarks. The production of charm and beauty baryons has also a particular interest to assess the thermalization and the mechanisms of hadronization of heavy flavours in the medium, because it was predicted that their production could be significantly enhanced in nuclear collisions. For light flavour and strange baryons, such an enhancement was indeed observed at intermediate transverse momenta at RHIC and at LHC, as shown in Figure 1.27.

Within thermal models, it is assumed that charm and beauty hadrons are produced during the QGP hadronization and that they are in thermal equilibrium with the medium. Within coalescence models, partons produced in hard scatterings can combine with quarks and antiquarks in the QGP

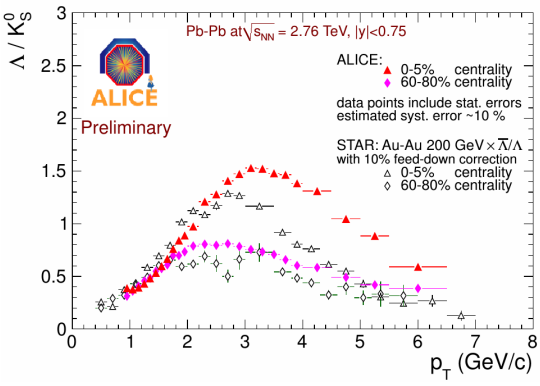

Figure 1.27: Λ/K^0_S *ratio vs transverse momentum as measured by ALICE at LHC and by STAR at RHIC [60, 61].*

to form hadrons. The resulting baryons from coalescence will have their strongest contribution in a momentum range intermediate between those from independent fragmentation and from thermal production. In addition, contrary to thermal models, coalescence models consider also the possibility of recombination of a heavy quark with diquarks present in the QGP. This could lead to a rather significant enhancement of the Λ_C with respect to thermal models, where the relative abundance of particles depends only on their masses. Some coalescence models consider also the possibility of recombination of a heavy quark with diquarks present in the QGP, which would lead to larger enhancements.

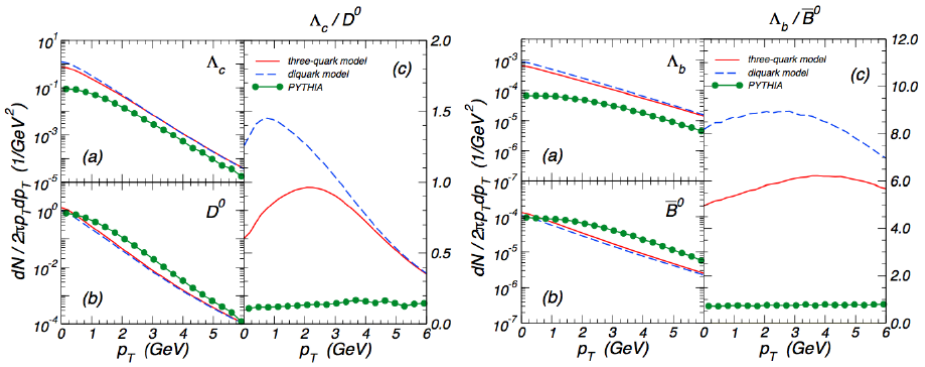

Figure 1.28: *Predicted heavy flavour baryon/meson enhancement as a function of* p_T *in* Au-Au *collisions at* $\sqrt{s_{\rm NN}} = 200\ GeV$. *Left:* Λ_c/D^0. *Right:* Λ_b/B^0 *[62].*

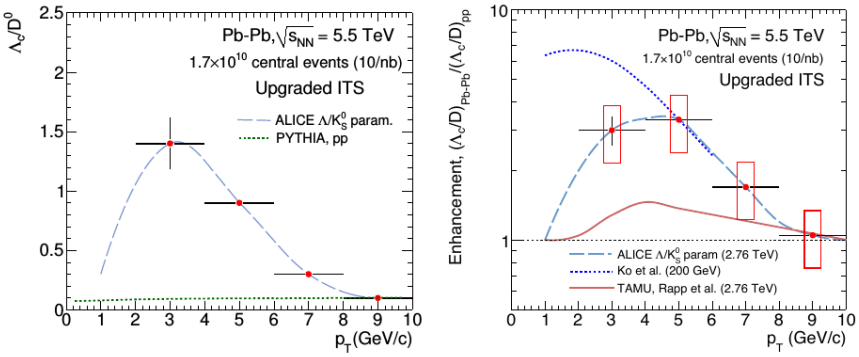

Figure 1.29: *Left: estimated statistical uncertainties on the measurement of the* Λ_c/D^0 *ratio using* 1.7×10^{10} *central* Pb-Pb *collisions* $(0 \div 20)\%$ *corresponding to an integrated luminosity of* $10\ nb^{-1}$*. The points are drawn on a line that captures the trend and magnitude of the* Λ/K^0_S *ratio (see Figure 1.27). The* pp *expectation from the PYTHIA v6.4.21 generator is also shown. Right: enhancement of the* Λ_c/D^0 *ration in central* Pb-Pb *with respect to* pp *collisions. Two model calculations are also shown [62, 63].*

In Figure 1.28 the predicted Λ_C/D^0 and $\Lambda_b/\bar{B}^0$ enhancement as a function of transverse momentum for central *Au-Au* collisions at RHIC ($\sqrt{s_{\rm NN}} = 200\ GeV$) are shown. The enhancement is up to 7÷10 for both baryon/meson ratios, and it is maximum at $p_T \approx 2\ GeV/c$ for charm and $\approx 4\ GeV/c$ for beauty. For strange quarks (Figure 1.27) the position of the maximum is higher at LHC with respect to RHIC energy. Therefore, one could expect the maximum of Λ_c/D^0 to be at p_T of about 3 GeV/c at LHC energy. This demands for a measurement of Λ_C production in central *Pb-Pb* collisions starting from p_T of $(2 \div 3)\ GeV/c$.

The Λ_C production can be measured in central and peripheral collisions, for $p_T > 2\ GeV/c$ with the planned upgraded ALICE detector (see Sec. 1.4). Figure 1.29 (left) presents the expected statistical uncertainties for the measurement of the Λ_c/D^0 ratio using 1.7×10^{10} central *Pb-Pb* collisions ($(0 \div 20)\%$), corresponding to an integrated luminosity of $10\ nb^{-1}$. The points are drawn on a line that captures the trend and magnitude of the Λ/K^0_S ratio. Figure 1.29 (right) shows the enhancement of the Λ_c/D^0 ratio in central *Pb-Pb* ($(0 \div 20)\%$ for $L_{int} = 10\ nb^{-1}$). It is assumed that the statistical uncertainties for the D^0 measurements and for the Λ_c measurement in *pp* are negligible with respect to those for the Λ_c measurement

in *Pb-Pb* [64].

1.4 Perspectives in heavy-ion physics

The ALICE experiment widely confirmed the evidences of the quark-gluon plasma matter created at SPS and further studies at RHIC.

According to theoretical predictions, at high temperatures the QGP was expected as a weakly-interacting gas of quarks and gluons. Heavy-ion experiments indicate instead the formation of a strongly-coupled plasma with very short mean free path, with a high degree of collectivity and flows. It has been possible to characterize the QGP as an almost-perfect liquid on the basis of the results from CERN SPS and BNL RHIC experiments of the last two decades. Then, after the first three years of LHC running, the ALICE, CMS and ATLAS experiments have confirmed this picture extending the precision and kinematic range of all significant probes of the QGP. Furthermore, it also observed the creation of hot hadronic matter at unprecedented values of temperatures, densities and volumes [65]. However, several fundamental aspects about the QGP are not well understood at present. Important open questions remain about the parton-hadron transition and the nature of confinement, and about the nature of QCD matter at high temperature. A much deeper insight into the mechanisms underlying chiral symmetry breaking and the origin of light-quark mass is necessary.

In 2012, the ALICE collaboration presented a plan to extend its physical programme, in order to fully exploit the scientific potential of the LHC for fundamental studies of QCD, with the main emphasis on heavy-ion collisions [64]. The proposed upgrade of the ALICE detector performance will enable detailed and quantitative characterization of the high density, high temperature phase of strongly interacting matter, together with the exploration of new phenomena in QCD. In order to achieve access to rare physics channels and collect a large statistical sample of minimum-bias events, needed to better understand the QGP state, an upgrade has been scheduled for 2019-2020. Between 2020 and 2028 an integrated luminosity of 10 nb^{-1} is foreseen to be collected.

So far, I have described the physics of the ALICE experiment and its main physics aims. In the following chapter I am going to present the ALICE detector together with its upgrade programme and with a focus on the TOF subdetector.

Chapter 2

The ALICE experiment

The ALICE experiment is a general-purpose detector installed at the CERN LHC optimized for the study of heavy-ion collisions. Its final aim is to focus on QCD, the strong interaction sector of the Standard Model and in particular on the study of strongly interacting matter under extreme energy density and temperature in heavy-ion collisions, discussed in the previous chapter.

The first conceptual idea for such general-purpose heavy-ion detector at the LHC was formulated in 1990. The experiment was approved in 1997 and it was put into operation in 2009. The first lead ion runs at $\sqrt{s_{\mathrm{NN}}} = 2.76\ TeV$ were collected in 2010 and 2011. In 2013, before the first long shutdown (LS1) of the LHC, the first run colliding protons and lead ions was done, with a centre-of-mass energy of $\sqrt{s_{\mathrm{NN}}} = 5.02\ TeV$. During the Run 2 (2015-2018) data taking the energy of $\sqrt{s_{\mathrm{NN}}} = 5.5\ TeV$ per colliding nucleon pair in *Pb-Pb* collisions is planned to be reached.

The main requirements for a heavy-ion experiment are an efficient tracking system within a large acceptance and a good particle identification in a wide momentum region. The detector design of the ALICE experiment developed consequently. An efficient online trigger system is also needed for specific analyses, for example those involving high-p_T electrons and rare processes. Therefore, in ALICE it is possible to track and identify particles from very low ($\sim$100 MeV/c) up to quite high ($\sim$100 GeV/c) transverse momenta in an environment with large charged-particle multiplicities. Estimates for the charged particle multiplicity density at mid-rapidity in central *Pb-Pb* collisions spanned the range from $\frac{dN}{d\eta} = 2000$ up to almost $\frac{dN}{d\eta} = 8000$. The ALICE experiment is optimized for a value of about $\frac{dN}{d\eta} = 4000$ and tested

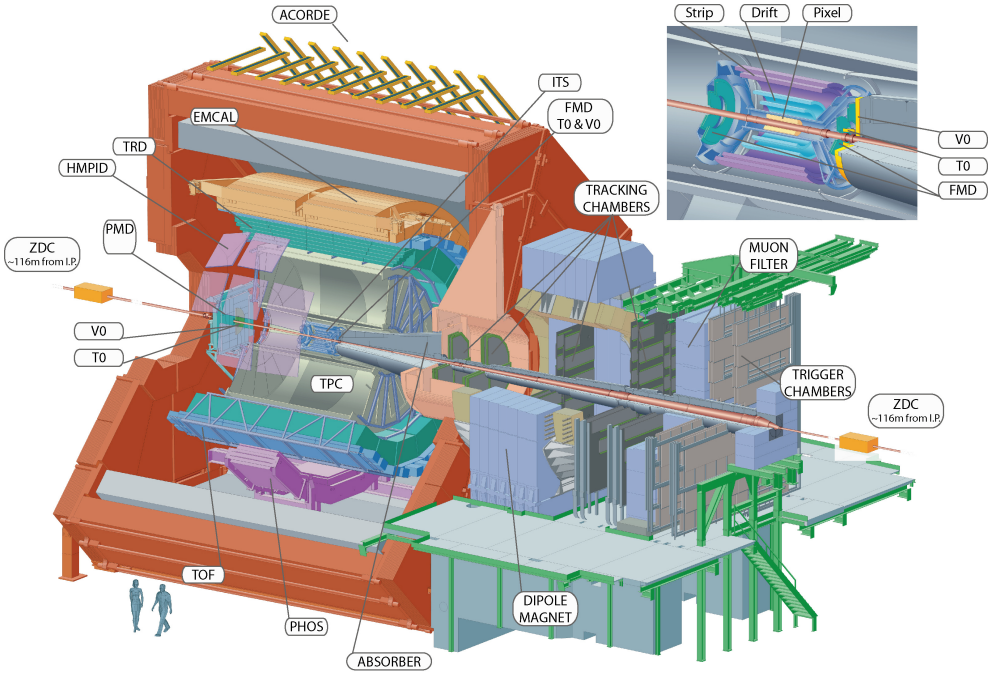

Figure 2.1: *ALICE schematic layout [66].*

with simulations up to twice that amount. ALICE is equipped with slow but high-granularity detectors, since radiation doses are moderate and the interaction rate with nuclear beams at the LHC is low (10 kHz for Pb-Pb collisions). The tracking uses three-dimensional hit informations with up to 150 points in a magnetic field of 0.5 T. The choice of a low magnetic field allows the reconstruction of low-momentum particles. To measure particle momenta over such a broad momentum range, a combination of very thin materials reduces the multiple scattering at low p_T while a large tracking lever arm of up to 3.5 m guarantees a good resolution at high p_T. Particle Identification (PID) over much of this momentum range is essential, as many observables are either mass or flavour dependent. ALICE employs essentially all known PID techniques: specific ionization energy loss $\frac{dE}{dx}$, time-of-flight, transition and Čherenkov radiations, electromagnetic calorimetry, muon filters and topological decay reconstruction.

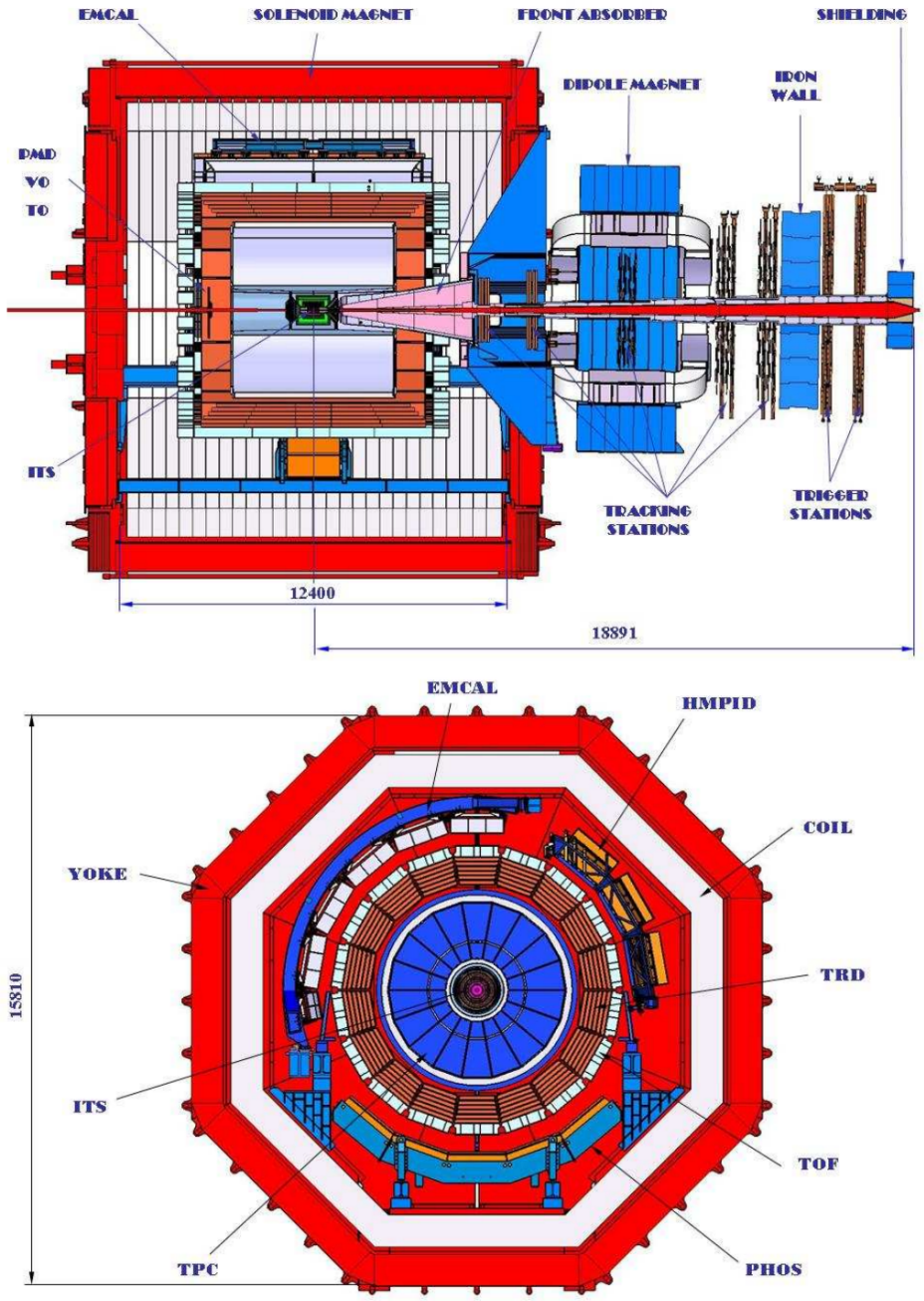

Figure 2.2: *Two-dimensional cut views along the yz direction (upper part) and along the xy direction (lower part). The detector overall dimensions are $\sim 16 \times 16 \times 26\ m^3$ with a total weight of approximately $10^4\ tons$. Distances reported in the upper part are expressed in millimeters [66].*

2.1 Detector layout

Figures 2.1 and 2.2 give a general overview of the ALICE detector. The coordinate system in the ALICE experiment is defined such as the positive z-axis is parallel to the mean beam direction, pointing in the direction opposite to the muon spectrometer. The x-axis is then perpendicular to the mean beam direction, aligned with the local horizontal and pointing to the accelerator centre and the y-axis is perpendicular to the x-axis and to the mean beam direction, pointing upward.

The detector consists of a central barrel part, which measures hadrons, electrons and photons, and other forward detectors. The central system covers the pseudo-rapidity region $|\eta| \leq 0.9$ (which corresponds to polar angles from 45° to 135°) over the full azimuthal angle and is embedded in a large solenoid magnet reused from the L3 experiment at LEP. It includes, from the beam pipe to the outside, the Inner Tracking System (ITS), a cylindrical Time-Projection Chamber (TPC), three particle identification arrays of Transition Radiation detectors (TRD), Time-of-Flight (TOF), Ring Imaging Čherenkov (HMPID) and two electromagnetic calorimeters (PHOS and EMCal). All detectors except HMPID, PHOS, and EMCal cover the full azimuth. The forward muon arm ($2° \div 9°$) consists of a complex arrangement of absorbers, a large dipole magnet, and fourteen planes of tracking and triggering chambers. Several smaller detectors (ZDC, PMD, FMD) for global event characterization and triggering are located at small angles. In addition, the forward region is instrumented with a system of Čherenkov counters to provide the event time (T0) and with two arrays of segmented scintillator counters used for minimum-bias trigger and beam-gas background rejection (V0). An array of 60 large scintillators is installed on top of the magnet to provide a cosmic-ray trigger for calibration and alignment purposes as well as for cosmic-ray physics (ACORDE) [66]. A new subdetector, the di-jet calorimeter (DCAL), was installed during the Long Shutdown 1 (LS1, 2013-2014).

Improvement upgrades to the ALICE detector are scheduled for the second Long Shutdown 2 (LS2, 2019-2020), in order to prepare the detector to operate a higher luminosity, since 2020.

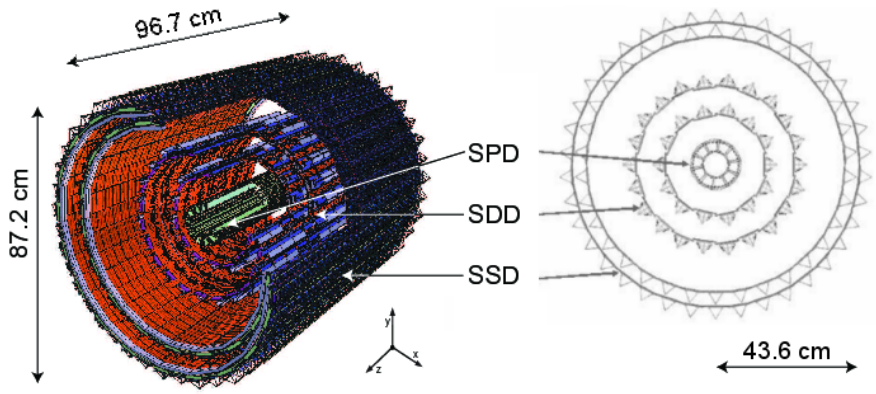

Figure 2.3: *Layout of the ITS detector. From the beam pipe to the outside: SPD, SDD and SSD silicon detectors [67].*

2.1.1 Tracking detectors

Tracking in the central barrel is divided into the Inner Tracking System and the Time-Projection Chamber. The Transition Radiation Detector (better discussed in the following Sec. 2.1.2) will also be used for tracking in the central region improving the p_T resolution at high momentum.

Inner Tracking System (ITS)

The Inner Tracking System surrounds the 800 μm-thick beryllium beam pipe of ALICE. As it can be seen in Fig. 2.3, it consists of six layers of high-resolution silicon pixel (SPD), drift (SDD), and strip (SSD) detectors. The layers are located in the central barrel at radii $r \approx (4, 8, 15, 24, 38, 43)$ cm from the beam pipe axis. Another representation is given in the box of the Fig: 2.1, where FMD (at both sides of the ITS) and the front absorber (muon-spectrometer side) are also shown. The innermost radius is determined by the requirements for the beam pipe, while the outermost is chosen in order to match tracks from the ITS to the TPC and viceversa. The tracking system meets the following requirements:

- it has to localize the primary vertex with a resolution better than 100 μm, in order to detect hyperons and open charm and beauty particles;
- it has to permit the secondary vertex reconstruction from hyperon

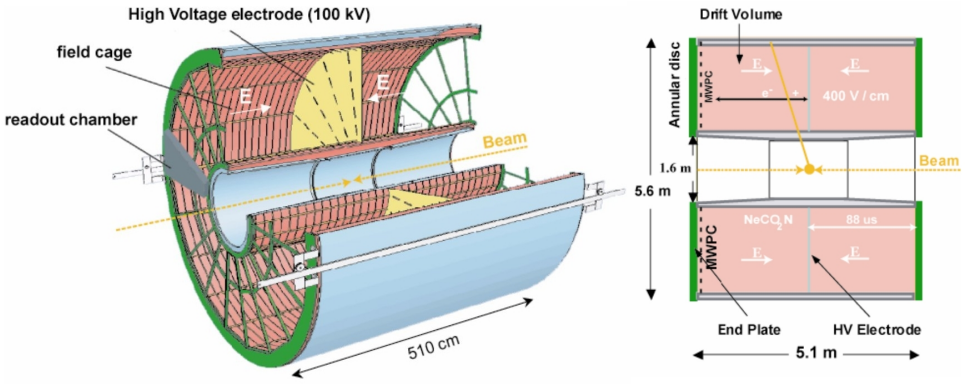

Figure 2.4: *On the left: a tridimensional schematic of the ALICE-TPC. On the right: some details concerning the field cage.*

decays and from D and B meson decays;

- it has to track and identify particles with transverse momentum below 200 MeV/c, that are in general too much deflected by the magnetic field to be reconstructed by the TPC;
- it has to improve momentum and angle resolution of high-p_T particles and to reconstruct particles crossing dead regions of the TPC.

Due to the high charged-particle density expected for *Pb-Pb* collisions, high-granularity devices have been chosen for the innermost layers of the ITS, the two layers of Silicon Pixel Detectors (SPD) and the two layers of Silicon Drift Detectors (SDD). At larger radii, where high granularity requirements are no more essential, two layers of double-sided Silicon Strip Detectors (SSD) are used. The SDD and SSD detectors have also analogical read-out (R/O) and therefore can be used for particle identification at low momentum via energy loss $\frac{dE}{dx}$ measurements [66, 68].

Time Projection Chamber (TPC)

The Time Projection Chamber (Fig. 2.4) is the main tracking detector of the ALICE central barrel. Together with other central-barrel detectors the TPC contributes to provide charged-particle momentum measurements with good two-track separation, particle identification and vertex determination. The TPC is cylindrical in shape, with an active volume of 88 m^3. The internal radius is 0.85 m and the outer about 2.50 m. The overall length along

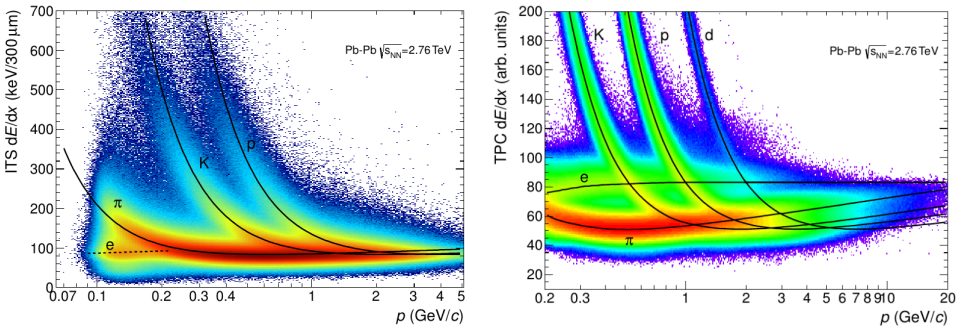

Figure 2.5: *On the left: Distribution of the energy-loss signal in the ITS as a function of momentum. On the right: Specific energy loss in the TPC vs particle momentum in* Pb-Pb *collisions at* $\sqrt{s_{\rm NN}} = 2.76\ TeV$. *The lines show the parametrizations of the expected mean energy loss [71].*

the beam direction is 5 m. The chamber is filled with a $Ne/CO_2/N_2$ gas mixture which gives low radiation length, low diffusion and low multiple scattering inside the field cage. The N_2 admixture improves the quenching and allows higher maximum gas gains. The chamber is divided in two drift regions by a high voltage (100 kV) stretched Mylar electrode which gives a voltage gradient of 40 kV/m and guarantees the perpendicularity of the field along the chamber. The electron drift velocity of 0.0283 $m/\mu s$ over 2.50 m (the maximum drift length) fixes the maximum drift time of 88μs which defines the rate capability of the TPC. Electrons produced by ionization processes from particles crossing the TPC, drift in the gas until they are detected by Multi-Wire Proportional Chambers (MWPC) at the edges of the detector. The charge collected on TPC read-out pads is used to measure the linear stopping power[1] and it allows to evaluate the mean energy loss per path length ($\frac{dE}{dx}$). Combining particle specific energy loss with particle momentum measurements in the Bethe-Bloch formula in the low-momentum region it is possible to obtain the mass of the particle crossing the detector [69, 66, 70].

Figure 2.5 shows the energy-loss in the ITS and in the TPC detectors. While at low momenta particles can be easily identificated, often on a

[1]The stopping of a charged particle travelling in matter includes both collisional and radiative processes. Linear stopping pawer, S, also referred to as specific energy loss is given by $S = -\frac{dT}{dx}$, where T is the kinetic energy of the particle. The higher the stopping power, the shorter the range into the material the particle can penetrate.

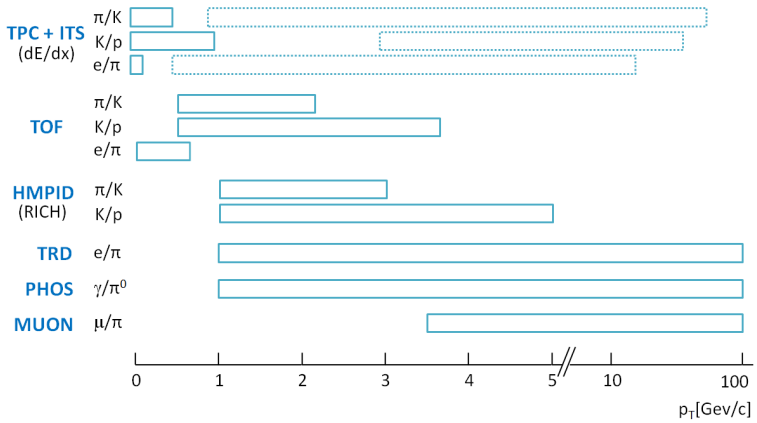

Figure 2.6: *Indicative PID range momenta for different ALICE subdetectors.*

track-by-track basis, in the relativistc rise region, the $\frac{dE}{dx}$ exhibits a nearly constant separation for the different particle species over a wide momentum region. The main limitation at the moment is the statistical precision, so it is expected that the measurement can be extended up to $\sim$50 GeV/c in the future [71].

2.1.2 Particle identification detectors

Particle identification is a key strength of the ALICE experiment. Besides the TPC and the ITS which rely on the particle energy loss ($\frac{dE}{dx}$), other detectors are specifically built to this purpose and use different approaches.

Charged hadrons are identified combining information provided by the ITS, TPC, TRD, TOF, and HMPID detectors. Electrons are identified using information mainly from the TRD and the TPC. The information from the EMCal will improve the purity of electron identification, especially at higher momenta. The PHOS spectrometer detects and identifies photons. Figure 2.6 shows PID range momenta for various ALICE detectors and for the main particle separations. Separation power of the different detectors is in Fig. 2.7 for hadron separation. Charged-particle identification based on a $\frac{dE}{dx}$ measurement performs well in the $\frac{1}{\beta^2}$ region (i.e. for low momenta) and, for gas-based detectors, in the multi-GeV region. However, this technique inevitably leaves a hole in the momentum range around the minimum of the

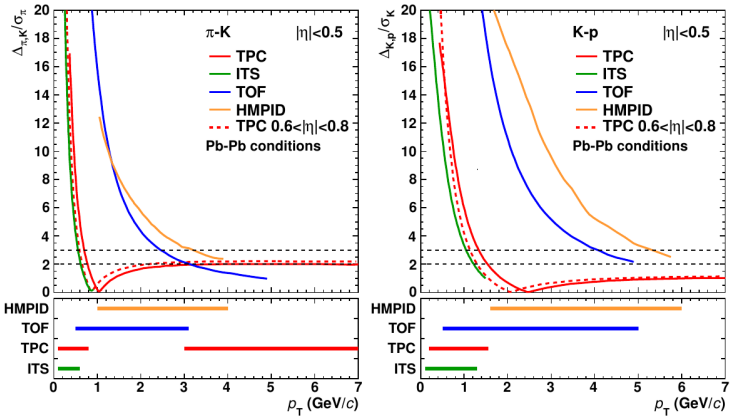

Figure 2.7: *Separation power of hadron identification in the ITS, TPC, TOF, and HMPID as a function of p_T at midrapidity. The left (right) panel shows the separation of pions and kaons (kaons and protons), expressed as the distance between the peaks divided by the resolution for the pion and the kaon, respectively, averaged over $|\eta| < 0.5$. For the TPC, an additional curve is shown in a narrower η region. The lower panels show the range over which the different ALICE detector systems have a separation power of more than 2σ [71].*

ionizing losses, i.e. $\sim(0.9 \div 3)$ GeV/c. In the ALICE experiment this range is covered by the TOF detector (see Sec. 2.2).

Transition radiation detector (TRD)

Relativistic charged particles travelling in inhomogeneous mediums or, better, in a stratified detector emit the so-called transition radiation. The threshold of the phenomenon depends on the Lorentz γ factor of the particle crossing the medium and it is about $\gamma \gtrsim 1000$ [69]. Figure 2.8 shows some representations of the TRD in the ALICE experiment. The detector is composed of several modules, each consisting of a radiator where x-rays are emitted by the charged particle per boundary crossing, and a multi-wire proportional read-out chamber which detects the x-rays. The TRD in ALICE has been developed to comply with specific requests, such as to have good capability to reject pions and a good resolution of position and momentum from the track. In addition, the detector design minimizes the radiation length, in order to reduce the bremsstrahlung which can affect the correct determination of momenta. The detector provides electron identification in the momentum region above $\sim$1 GeV/c, where the identification through

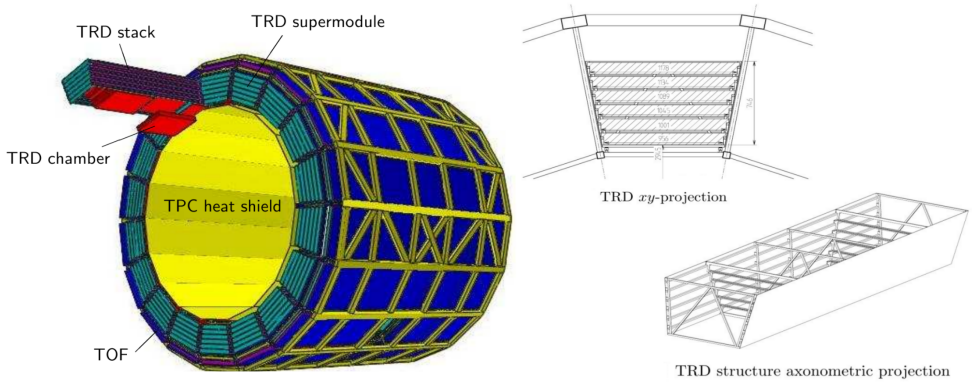

Figure 2.8: *Schematic views of the TRD detector.*

ionization energy loss made by the TPC becomes no more efficient. Thus, the granularity of the detector has to be high enough to identify electrons even in conditions of high multiplicity of charged tracks, as expected in heavy-ion collisions where the production of J/ψ and Υ is measured via their dielectron decay channels. Figure 2.9 shows the combined TRD signal ($\frac{dE}{dx}$ and TR) as a function of momentum for p-Pb collisions and the dependence of the most probable TRD signal on $\beta\gamma$. The onset of TR production is visible for $\beta\gamma = 800$, both for electrons and high-energy (TeV scale) cosmic muons. Also note that the muon signal is consistent with that from electrons at the

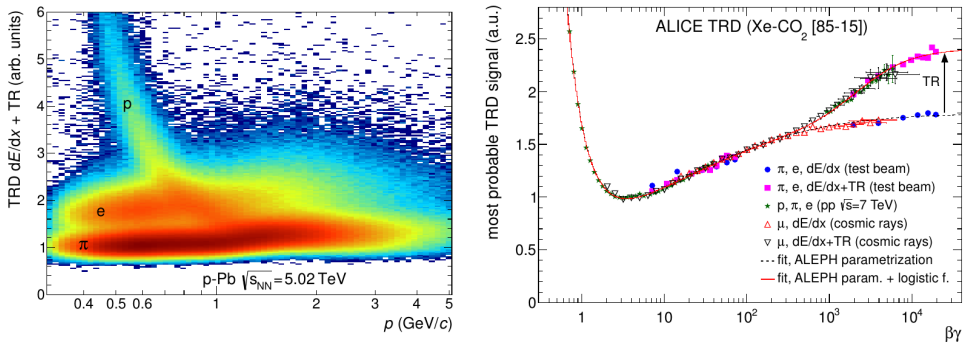

Figure 2.9: *On the left: sum of the TRD signal (ionization energy loss plus transition radiation) as a function of momentum for protons from γ decays, charged pions from K^0_S decays, and electrons from Λ conversions in* p-Pb *collisions. On the right: the most probable TRD signal as a function of $\beta\gamma$. Measurements performed in test beam runs,* pp *collisions and cosmic rays are compared [71].*

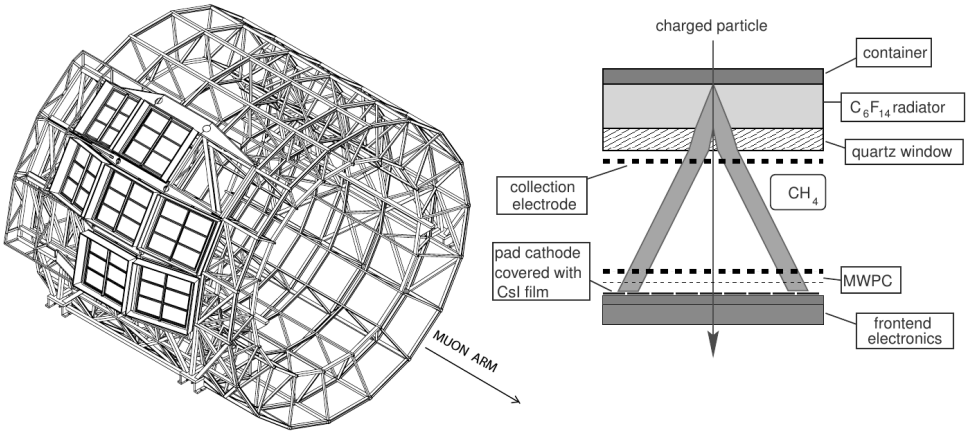

Figure 2.10: *On the left: the seven modules of the HMPID on the cradle surrounding the beam pipe. On the right: the working principle of the RICH detector.*

same $\beta\gamma$ [66, 72].

High-momentum Particle Identification (HMPID)

The HMPID detector is conceived to identify hadrons with momenta larger than 1 GeV/c and then to improve the PID capabilities of the ALICE detector, by extending the momentum region for π/K and K/p separation up to 3 GeV/c and 5 GeV/c respectively. It is particularly dedicated to inclusive measurements of identified hadrons for $p_T > 1$ GeV/c. The Čherenkov light cone produced by a particle above the threshold refracts out of the liquid radiator and expands in the proximity volume of CH_4 before reaching the MWPC photon detector [66, 73].

The HMPID is based on the detection of the Čherenkov radiation that is generated by a particle crossing a dielectric medium with velocity $\beta \geq \beta_{thr} = \frac{1}{n}$, where n indicates the refraction index of the medium. Čherenkov photons are then emitted at θ_c angle, given by the relation

$$cos\theta_c = \frac{1}{n\beta}. \tag{2.1}$$

Ring Imaging Čherenkov (RICH) detectors are arranged in an array with an acceptance of 5% of the central barrel phase space (Fig. 2.10, left). On the right side of the Figure 2.10 a depiction of the HMPID working scheme is shown. The detector is thus composed by proximity-focusing RICH counters employing CsI thin films deposited onto the cathode plane

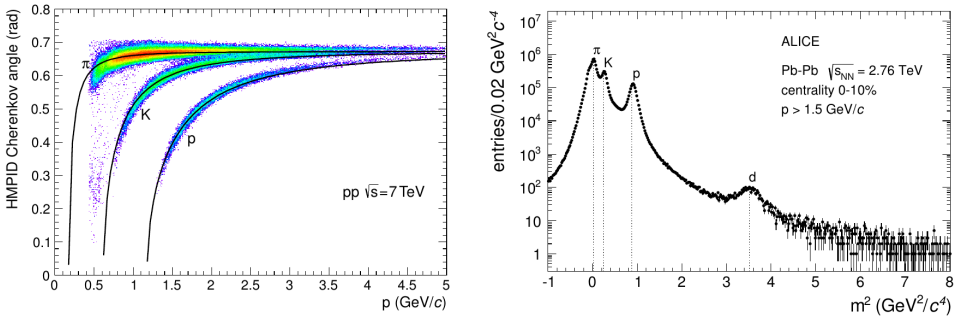

Figure 2.11: *On the left: Mean Čherenkov angle measured by HMPID in* pp *collisions at* 7 TeV *as a function of track momentum. On the right: Squared particle masses calculated from the momentum and velocity determined with ITS-TPC and HMPID, respectively, in central* Pb-Pb *collisions at* $\sqrt{s_{\rm NN}} = 2.76\ TeV$ *[71].*

of MWPC.

The left side of Fig. 2.11 shows the measured Čherenkov angle as a function of track momentum for pions, kaons, and protons in pp collisions at 7 TeV. The lines represent parametrizations of Eq. (2.1) for each species. The separation of kaons from other charged particles, determined by fitting the Čherenkov angle distribution with three Gaussians for each transverse momentum bin (the background is negligible), is 3σ for $p_T < 3\ GeV/c$ for pions and $p_T < 5\ GeV/c$ for protons. On the right side of the figure, the squared mass distribution of particle identified by the HMPID in central *Pb-Pb* collisions is reported. The velocity is calculated from the Čherenkov angle measured in the HMPID. Dotted lines indicate the PDG mass values. The pion tail on the left-hand side is suppressed by an upper cut on the Čherenkov angle. The good performance of the pattern recognition in the high-multiplicity environment of central *Pb-Pb* collisions is supported by the fact that the deuteron peak is clearly visible and that all the particle peaks are at their nominal mass values.

2.1.3 Electromagnetic calorimeters

The ALICE detector is also equipped with two electromagnetic calorimeters: the Photon Spectrometer (PHOS) and the Electromagnetic Calorimeter (EMCal).

Photon Spectrometer (PHOS)

The PHOS is a high resolution electromagnetic calorimeter conceived for the detection of direct photons from the interaction point and neutral mesons (e.g. the π^0) decaying in two photons. The main task of the detector is to distinguish between direct photons or photons produced in particle decays. Therefore, high granularity and good space and energy resolution are required. The segmentation must be below the Molière radius[2] of the material. The calorimeter is made of lead tungstate crystals ($PbWO_4$, $PbWO$) grouped in five modules of $20X_0$. The Molière radius of $PbWO$ is 2 cm. The PHOS is designed as a single-arm electromagnetic spectrometer consisting of 5 modules each made of a highly-segmented calorimeter and a Charged Particle Veto (CPV) detector, i.e. a MWPC with charged particle detection efficiency better then 99%. The PHOS is located at 460 cm from the interaction point and it covers the pseudo-rapidity region $-0.12 \leq \eta \leq 0.12$ and an azimuthal angle of 100°. Its total area is $\sim$8 m^2 [66, 74].

Electromagnetic Calorimeter (EMCal)

The main physics motivation for the EMCal is to improve the ALICE performances for an extensive study of jet quenching. In fact the EMCal enlarges the ALICE p_T capabilities for jets, direct photons and electrons from heavy-flavor decays. The detector includes several modules each consisting of sampling calorimeters made of alternating layers of polystirene scintillator and lead, of 1.76 mm and 1.44 mm respectively. The EMCal covers the pseudo-rapidity range $0.7 \leq \eta \leq 0.7$ and 110° in ϕ. It is positioned to provide partial back-to-back coverage with the PHOS and its nominal acceptance is about 25% of the TPC acceptance [66, 75].

2.1.4 Muon spectrometer

Muon detection is performed in the pseudo-rapidity range $-4.0 \leq \eta \leq -2.5$, by the muon spectrometer. The detector built in ALICE is expected to measure the complete spectrum of heavy-quark vector-meson resonances (i.e. J/ψ, ψ', Υ, Υ', Υ'') in the $\mu^+\mu^-$ decay channel. The simultaneous

[2]The Molière radius, $R_M = 0.00265X_0(Z + 1.2)$, with X_0 indicating the radiation length, describes the electromagnetic characteristic of the material and it is related to the transverse dimension of the electromagnetic shower in the calorimeter. Therefore, the smaller is R_M, the better is the capability of the calorimeter to contain and measure the shower.

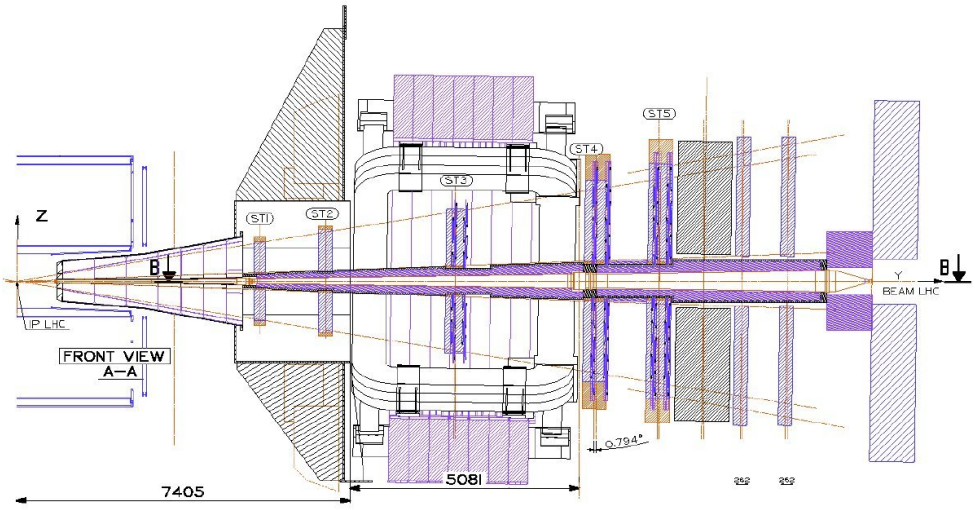

Figure 2.12: *Layout of the muon spectrometer.*

measurements of quarkonia species with the same apparatus allow a direct comparison of their properties (production rate, width) versus different global parameters such as collision centrality. The layout of the Muon Spectrometer is shown in Fig. 2.12. Absorbers with a small interaction length are needed to better absorb hadrons and absorbers with large radiation length to reduce multiple scattering. Muon tracks are then reconstructed by tracking chambers consisting of MWPC with cathode pad read-out. The conical front absorber on the left side of the Fig. 2.12 is followed by 10 tracking planes: 4 placed between the absorber itself and the dipole magnet, two inside the magnet and four between the magnet and the muon-filter wall. Four planes of trigger chambers follow the muon filter. The trigger on dimuon signals is done by four layers of Resistive Plate Chambers (RPCs) operating in streamer mode located behind a second absorber [66, 76].

2.1.5 Forward rapidity detectors

To complete the experimental apparatus forward detectors are located at small angles with respect to the beam axis.

Zero-Degree Calorimeter (ZDC)

The Zero Degree Calorimeters (one on each side of the interaction point)

provide information about the centrality of events by measuring the energy of spectator nucleons. The zero-degree forward energy, in fact, decreases with increasing centrality. Each ZDC consists of two calorimeters, one for neutrons (ZN) and one for protons (ZP). The adopted technique for this detector is to alternate a dense absorber (passive material), in which incident particles originate showers, and quartz fibers (active material), where the showers produce Čherenkov radiation [66, 77].

Photon Multiplicity Detector (PMD)

The Photon Multiplicity Detector measures the multiplicity and the spatial distribution of photons on an event-by-event basis in the forward region of ALICE. It consists of two planes of gas proportional counters having a honeycomb structure with a thick lead converter in between them. The PMD is placed at 360 cm from the interaction point, on the opposite side of the forward muon spectrometer, covering the $2.3 \leq \eta \leq 3.7$ region [66, 78].

Forward Multiplicity Detector (FMD)

The Forward Multiplicity Detector provides information on the charged-particle multiplicity and consists of five rings of silicon strip detectors, two of which are installed on the muon absorber side in the pseudo-rapidity region $-3.4 \leq \eta \leq -1.7$, while the remaining three are located on the opposite side of the interaction point, in the $1.7 \leq \eta \leq 5.1$ region. The FMD allows to extend the pseudo-rapidity coverage of multiplicity measurements to study multiplicity fluctuations on an event-by-event basis [66, 79].

T0 and V0 detectors

Both the T0 and V0 consist of two modules installed on each side of the interaction point. The T0 detector is composed by 24 Čherenkov radiators and it measures the start time of the event (used then by the TOF detector) with a precision of $\sim$50 ps. It also measures a rough vertex position, provides a first level trigger and helps to discriminate against beam-gas interactions. The V0 detector provides a minimum bias trigger for the central barrel detectors. It consists of scintillators, and it can be used as a centrality indicator [66, 79].

2.1.6 Trigger and DAQ systems in ALICE

Trigger systems are employed to rapidly decide which events to record and then analyse, due to limitations in computing power, data storage capacity and rates. The trigger and data acquisition (DAQ) systems of ALICE have been designed to give a fair share of the trigger and DAQ resources to different observables with respect to the DAQ bandwidth. They have also to balance the capacity to record *Pb-Pb* central collisions (which generate large events) with the ability to acquire large fractions of rare events.

During data taking, ALICE sub-detectors are in general busy for different periods. Then, the challenges for the trigger system are to optimize the use of component detectors and to be able to perform trigger selections for several different running modes (*Pb-Pb*, *p-Pb*, and *pp*) varying by almost two orders of magnitude in counting rate. To accomodate such a wide range of requirements, the ALICE Central Trigger Processor (CTP) generates three levels of hierarchical hardware triggers (L0, L1 and L2) before an event is accepted, transmitted to the Data Acquisition System (DAQ) and copied to the High Level Trigger (HLT) for further software assessments. Signals from the TOF, T0 and V0 detectors are sent to the TRD in less than 100 ns and constitute the first trigger signal, the TRD pre-trigger. The TRD electronics, which otherwise would be in stand-by, is then activated. The first response of the trigger system has to be fast enough to cope with the large multiplicities in *Pb-Pb* collisions and to suit detector requirements. The fast part of the trigger is split into two levels: a Level-0 (L0) signal from CTP, that reaches the detectors after 1.2 μs, and a Level-1 (L1) signal, that arrives after 6.5 μs. The L0 signal is too fast to receive all the trigger inputs. Therefore, the L1 signal arrives and picks up all remaining fast inputs. CTP decisions are made in 100 ns. The rest of the L0 latency comes from the generation time for the trigger input signals and from cable delays. When the L1 decision reaches the fast detectors, data conversion and bufferization starts on a temporary ring memory. The third trigger level (L2) fulfils the request to avoid event overlaps in the TPC. With a drift time of 88 μs, the TPC represents the *bottleneck* in the ALICE data acquisition. It may happen either that the drift charges of the previous event are still present in the TPC when the interesting event is coming, or that a subsequent event is triggered before the interesting one has been registered. In order to avoid such a problem, the *past-future* protection, i.e. a circuit which rejects any other event occurring

within a specified time window, is introduced. The final level of trigger, Level-2 (L2), waits for the end of the past-future protection interval. When the CTP sends the L2 decision, the event is ready to be transferred to the Data Acquisition system (DAQ).

The data acquisition system provides to transfer data from the front-end electronics to the control room. The transfer is initiated by the L2 trigger and it is done in parallel for all the subdetectors. The event building is performed first by either Local Data Collectors (LDCs), that collect event fragments and reassembles them into sub-events, and then by Global Data Collectors (GDC), which puts together all the sub-events pertaining to the same physics event, builds the full event and sends it to the mass storage system. The GDC is also capable of online event monitoring. Then, data are stored to the Permanent Data Storage (PDS) system. Mass storage bandwidth is 1.25 GB/s even though the aggregate bandwidth of read-out data from the detector is $\sim$25 GB/s. The event size of *Pb-Pb* collisions is rather big: $\sim$86.5 MB for central events, 50% and 25% of that size for semi-central and minimum bias events, respectively. ALICE DAQ is designed to cope with the event sizes resulting from heavy-ion collisions by using a combination of increased trigger selections and data compression [66, 80].

2.2 The ALICE-TOF detector

The Time-of-Flight technique allows to detect the β factor of a particle by independently measuring the length L of the trajectory of the particle and its time of flight t. It is then possible to obtain the mass of a particle from its momentum measurement:

$$m^2 = \frac{p^2}{c^2}\left(\frac{c^2t^2}{L^2} - 1\right). \tag{2.2}$$

Hence, mass resolution has three contributions:

$$\left(\frac{\delta m}{m}\right)_p = \frac{\delta p}{p}\ , \tag{2.3}$$

$$\left(\frac{\delta m}{m}\right)_L = \gamma^2\frac{\delta L}{L}\ , \tag{2.4}$$

$$\left(\frac{\delta m}{m}\right)_t = \gamma^2\frac{\delta t}{t}\ , \tag{2.5}$$

with $\gamma = \left(\frac{E}{m}\right)$. For $E \gg m$, the contributions relative to the length of the trajectory and to the time of flight are dominant. If one considers two different particles ($m_1 > m_2$) with the same momentum p, if $\frac{m_1^2}{p^2} \ll 1$ and $\frac{m_2^2}{p^2} \ll 1$, the difference between the two times of flight will be

$$\Delta t \sim \frac{L}{2c}\frac{(m_1^2 - m_2^2)}{p^2}. \tag{2.6}$$

The separation can thus be quantified in standard deviations as

$$n_{L,m_{1,2}} = \frac{\Delta t}{\sigma} = \frac{L(m_1^2 - m_2^2)}{2p^2 c\sigma}, \tag{2.7}$$

where σ is the time resolution [69].

2.2.1 Detector layout

The Time-of-Flight (TOF) detector in the ALICE experiment is a cilindrical large area array that covers the central pseudo-rapidity region for PID in the intermediate momentum range, below about 2.5 GeV/c for pions and kaons, up to 4 GeV/c for protons, with a π/K and K/p separation better than 3σ. Its main features include high granularity, an excellent time resolution (80 ps in Pb-Pb), high efficiency ($> 99\%$), and a large acceptance, covering the $-0.9 < \eta < 0.9$ pseudo-rapidity region with a large surface ($\sim$140 m^2) and full covering of azimuthal angle.

The detector has a modular structure corresponding to 18 sectors in ϕ and to 5 segments in z-direction. The TOF system is depicted in the left side of the Fig. 2.13 and it consists of 90 modules. Five modules in a row are arranged in a supermodule. Base units of the TOF detector are the 10 gap *double-stack* Multi-gap Resistive Plate Chambers (MRPCs).

Fig. 2.14 shows the principle of operation of the MRPC. It consists of a pile of resistive glass plates with a high voltage applied to the external surfaces. The passage of a charged particle ionises the gas contained in the chamber and the high electric field amplifies this ionization by an electron avalanche. Resistive plates, which stop the avalanche development in each gap, are transparent to the fast signal induced on the pick-up electrodes by the movement of the electrons. The total signal collected is then the sum of the signals from all gaps, whereas the time jitter of the signal depends on the individual gap width. The reason for many gaps is to achieve high efficiency, while narrow gaps permit to achieve good time resolution.

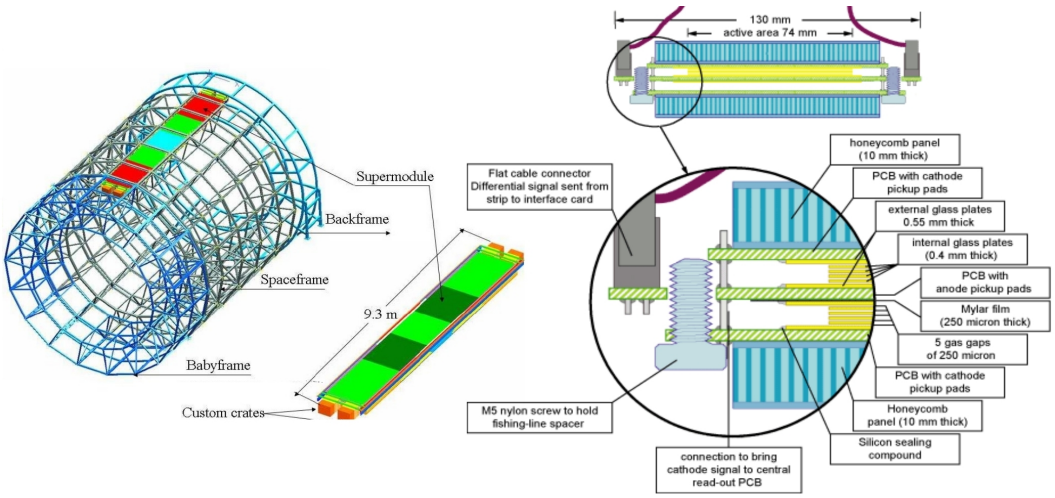

Figure 2.13: *Schematic view of the TOF detector. A drawing of a supermodule is also shown. On the right: A schematic of a single MRPC [81].*

Every module of the TOF detector consists of a group of MRPC strips: 15 in the central, 19 in the intermediate and in the external modules. In the right side of the Fig. 2.13 the structure of a single MRPC used in the ALICE-TOF detector is shown. The key feature of these chambers is that the electric field is high and uniform over the full sensitive gaseous volume of the detector.

Any ionisation produced by a traversing charged particle immediately starts a gas avalanche process which generates the observed signals on the pick-up electrodes. Unlike other types of gaseous detectors, there is no

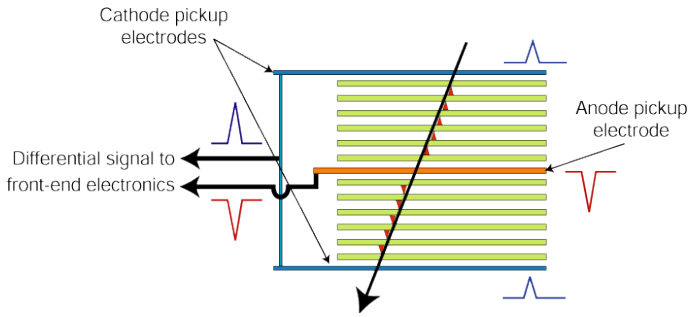

Figure 2.14: *Working scheme of a Multi-gap Resistive Chamber [81].*

drift time associated with the movement of the electrons to a region of high electric field. Thus the time jitter of these devices is caused by the fluctuations in the growth of the avalanche. The MRPC technology offers several advantages with respect to other parallel-plate chamber designs, such as:

- the chamber operates at atmospheric pressure;
- the signal is the analogue sum of signals from many gaps, so it has a peak well separated from zero and there is no late tail in the spectrum;
- the resistive plates quench the streamers so there are no sparks and high-gain operation becomes possible;
- the construction technique is in general rather simple and makes use of commercially available materials. The gas mixture, that is composed by $C_2H_2F_4$ (90%), i-C_4H_{10} (5%)[3] and SF_6 (5%), preserves the detector from degradation over time in a high radiation environment such as the LHC during heavy-ion collision runs.

To guarantee low detector occupancy even in the highest charged-particle density scenario ($\frac{dN_{ch}}{d\eta} = 8000$) the MRPC strip is segmented into two rows of 48 pick-up pads of $3.5 \times 2.5 cm^2$, for a total of about 153000 read-out channels [66, 82].

2.2.2 The ALICE-TOF R/O system

Each of the 18 ALICE-TOF supermodules is read out by 4 electronic crates, placed two by two at the ends of each supermodule. In each crate, one Data Read-out Module (DRM) collects the data from 10 TDC Read-out Module (TRM). A single TRM card includes 30 High Performance TDC (HPTDC) chips, where TDC stands for Time to Digital Converter. The read-out (see Fig. 2.15) is done in three distinct phases:

1. HPTDC read-out: the HPTDC chips internal buffers are read out and data shipped to TRM internal memories.
2. VME read-out: the 10 TRM cards are read out over the VME bus.

[3]The prefix *i-* for the C_4H_{10} molecule (*butane*) indicates the *isobutane* isomer also known as *methylpropane*.

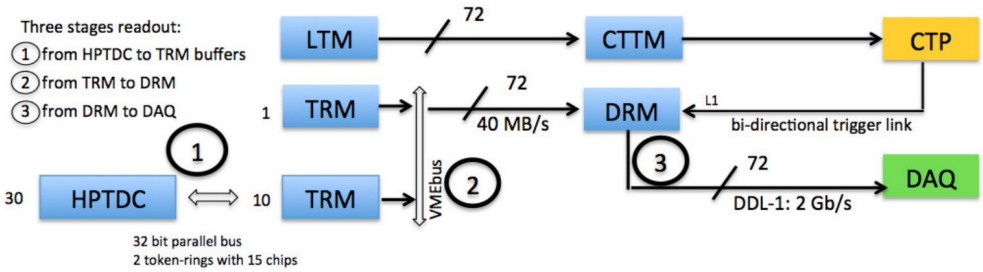

Figure 2.15: *The ALICE-TOF read-out scheme. In terms of DDL links, data segmentation is equal to the number of crates, which is 72 [83].*

3. DAQ read-out: data from the DRM are shipped to the ALICE Central Data Acquisition System over a DDL link.

At L1 trigger signal arrival ($\simeq 6\ \mu s$ after collision), a trigger is sent to the HPTDC and step 1 is performed. At the L2 arrival ($\simeq 80\ \mu s$ after collision), the TRMs are read out (step 2) and data are sent to DAQ (step 3). The large latency between L1 and L2 is exploited to read HPTDC. This system encounters a limitation in the number of DAQ LDCs serving multiple TOF DDL links and the servers. With only one DDL connected the system is able to read-out data at 67 KHz, while lower rates (tens of KHz) are reached with 6 concurrent links per LDC.

2.2.3 Performances

Figure 2.16 illustrates the performance of the TOF detector by showing the measured velocity β distribution as a function of momentum (measured by the TPC). The background is due to tracks that are incorrectly matched to TOF hits in high-multiplicity *Pb-Pb* collisions (mismatched tracks). The distribution is cleaner in *p-Pb* collisions (on the right side), showing that the background is not related to the resolution of the TOF detector, but is rather an effect of track density and the fraction of mismatched tracks. This is also visible in Fig. 2.17 where the β distribution is shown for a narrow momentum band. The pion, kaon, and proton peaks are nearly unchanged but the level of background due to mismatched tracks is higher in *Pb-Pb*. The fraction of mismatched tracks above 1 GeV/c in *Pb-Pb* events is closely related to the TOF occupancy. With 10^4 hits at TOF (corresponding to a very central *Pb-Pb* event) the TOF pad occupancy is 6.7% and the fraction

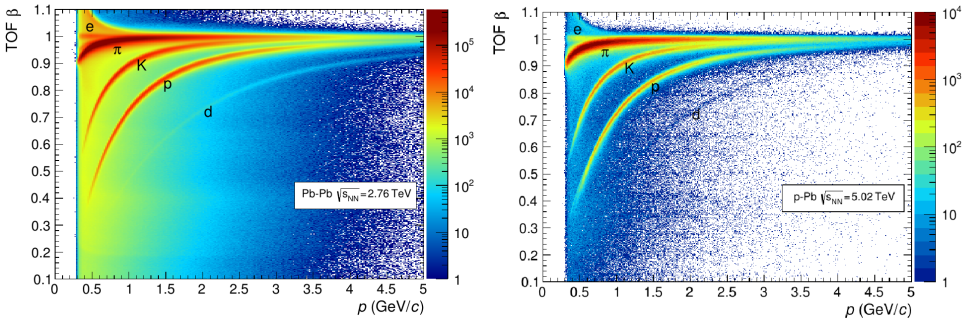

Figure 2.16: *Distribution of β as measured by the TOF detector as a function of momentum for particles reaching the TOF in* Pb-Pb *(left) and* p-Pb *(right) interactions [71].*

of mismatched hits is around 6.5%. While the resolution (width of the mass peaks) is the same, the background of mismatched tracks increases in the high-multiplicity environment of *Pb-Pb* collisions. The resolution can be studied in a given narrow momentum interval by computing the difference between the time of flight measured by TOF and the pion time expectation. The distribution is fitted with a Gaussian whose width is the convolution of the intrinsic time resolution of the TOF detector and the resolution of the event time. In the limit of high track multiplicity, where the error on the event time is negligible, the width becomes equal to the intrinsic resolution of the TOF detector and has a value of 80 ps.

2.3 The ALICE detector upgrade

The main physics topics addressed by the proposed upgrade programme for the ALICE experiment require the measurement of heavy flavour hadrons, quarkonia, and low-mass dileptons at low transverse momenta. Such measurements will be characterized by rare signals which calls for large statistics, better available with the luminosity enhancement foreseen after the LHC LS2. While the excellent particle identification capabilities of the current ALICE detector have to be preserved, a significant improvement of positioning resolution and substainable read-out rate will be needed.

On the basis of these considerations and of physical motivations introduced in Sec. 1.4, the experimental approach taken by ALICE is to read out all *Pb-Pb* events at an interaction rate of 50 kHz and significantly improve

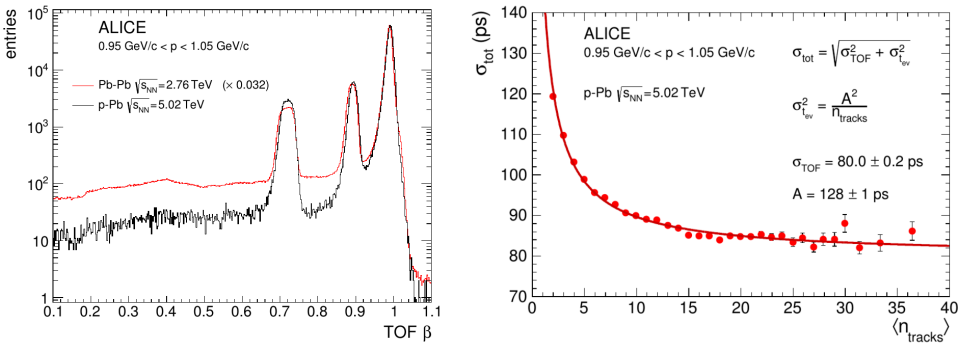

Figure 2.17: *On the left: the β distribution for tracks with momentum $0.95\ GeV/c < p < 1.05\ GeV/c$. The* Pb-Pb *histogram is normalized to the* p-Pb *one at the pion peak ($\beta = 0.99$). On the right: time resolution of pion tracks with $0.95 < p < 1.05 GeV/c$ as a function of the number of tracks used to define the start time of the collision. The data are from* p-Pb *collisions [71].*

vertexing and tracking capabilities at low transverse momentum. This implies also a modification of the read-out of single detectors in order to comply with the foreseen high read-out rate. The building of a new ITS and a major upgrade of the TPC detector will be required.

While Muon Spectrometer, EMCal and TRD detectors are going to improve their present readouts to finite rate values (50 kHz, 5 kHz and 40 kHz, respectively) for both *pp* and *Pb-Pb* interactions, the TPC detector is upgrading to *continuous* read-out. The ITS plans to reach 50 kHz in *Pb-Pb* and several hundreds of kHz in *pp* collisions. For the TOF detector an upgrade to a maximum read-out rate of 250 kHz is planned. Anyway, as a part of this thesis work, a possible way to achieve the continuous read-out even for the TOF detector and its effects on data acquisition have been studied. The results are reported in the following Chapter 3. Since for the measurement of heavy-flavour and low-mass dielectrons, the key detectors are the ITS, TPC and TOF, the achievement of a continuous read-out even for the TOF can play a crucial role in order to collect large statistical sample [64].

2.3.1 ITS upgrade

Based on the technologies available at that time, all ITS sub-detector elements were optimized to minimize their radiation length, achieving be-

tween 0.8% and 1.3% of X_0 per layer, as reported in Tab. 2.1. Another 1.3% of X_0 comes from the thermal shields and supports installed between SPD and SDD barrels and between SDD and SSD barrels, thus making the total material budget $\frac{X}{X_0}$ for perpendicular tracks equal to 7.63% of X_0. Reducing the material budget of the first detection layer is particularly important for improving the impact parameter resolution and reducing the probability of photon conversion. It is planned to reach a radiation length of 0.3% per layer or better making use of new Monolithic Active Pixel Sensors (MAPS) which allow the silicon material budget per layer to be reduced by a factor of 7 in comparison to the present ITS (50 μm instead of 350 μm).

Since in the ALICE upgrade programme a new beam pipe is planned, another intervention in the current detector will regard the first detection layer, that will be closer to the beam line from the current 39 to 22 mm. A new silicon tracker will enable tracking position resolution at the primary vertex to be improved in resolution by a factor 3 or larger.

However, the crucial limitation of the present ITS detector is given by its poor read-out rate capabilities. Read-out times and maximum event read-out rates for the ITS subdetectors under the assumption of no back pressure from the DAQ network are listed in Table 2.1. The read-out time of the three ITS sub-detectors depends only marginally on the detector occupancy and, therefore, it is very similar for *pp* and *Pb-Pb* events. As it can be seen from the table, the ITS can run up to a maximum of about 1 kHz (with 100% dead time) irrespective of the detector occupancy. This rate limitation restrict ALICE to use only a small fraction of the full *Pb-Pb* collision rate and it will also prevents the collection of the required reference data in *pp* collisions. The new ALICE detector aims to read the data related to each individual interaction up to a rate of 50 kHz for *Pb-Pb* collisions and several hundreds of kHz for *pp* collisions. The new ITS read-out will support triggered read-

	X/X_0	R/O time (μs)	Max. rate (kHz)
SPD	1.14%	296	3.300
SDD	1.13%, 1.26%	1023	0.985
SSD	0.83%	310	3.265

Table 2.1: *The thickness of the scattering medium in radiation lengths for both layers of each subdetector are reported in the first coloumn. Read-out times and maximum rate of the ITS sub-detectors are showed in the second and third coloumns, respectively.*

out mode. In triggered read-out mode, only the hits integrated over a time window that includes the event will be shipped off-detector [64].

2.3.2 TPC upgrade

The TPC was optimized to provide high precision momentum and particle energy loss ($\frac{dE}{dx}$) measurements in the unprecedented charged-particle densities in central *Pb-Pb* collisions at the LHC.

The maximum read-out rate of the present TPC is set to 3.5 kHz and constitute a first limitation of the detector. The read-out chambers, in fact, are based on MWPC technology and employ a wire grid scheme which includes a plane of anode wires, cathode wires, and a gating grid. The maximum drift time of ions from the amplification region to the gating grid is about 180 μs. In order to provide efficient ion gating, the gating grid must be closed for 180 μs after the end of the electron drift. In addition, a 100 μs past protection is applied to avoid event pile-up. Another limitation is given by the read-out electronics that is capable of sustaining a maximum rate of minimum-bias events of 520 Hz. The foreseen 50 kHz rate scenario for *Pb-Pb* collisions requires the overcome of the present limitations imposed by the operation of the gating grid and a continuous read-out for the TPC.

The replacing of the present MWPC based read-out chambers with new Gas Electron Multiplier (GEM) detectors will allow an excellent rate capability and an intrinsic ion blocking without additional gating. Nevertheless no principal limitation on the achievable $\frac{dE}{dx}$ resolution in a large-scale detector are imposed, due to a local energy resolution similar to that of a MWPC. The introduction of the new GEM technology will also imply the replacement of the existing front-end electronics, in order to accommodate for the inverted signal polarity and to provide the full flexibility of a continuous read-out. The existing field cage as well as most of the services of the present TPC will remain.

The replacement of multi-wire proportional chambers with GEM detectors and the requirement of a continuous read-out call for the development of new front-end and read-out electronics. The current system is not suitable for the upgraded TPC for two main reasons. First, the shaping-amplifier reads signals with a positive polarity, while its dynamic range for negative polarity as those produced by GEM detectors, is limited to about 100 times the noise and, therefore, not adequate to accommodate the TPC signals

(dynamic range 900:1). The second limitation is related to the read-out scheme. The ALice Tpc Read-Out (ALTRO) chip does not support a continuous read-out. After the sampling of the TPC segnals, it either records them in a local memory or transfers them off detector. The two operations cannot occur concurrently. The new read-out system for the upgraded TPC can be built on the basis of the current TPC read-out and of a new SAMPA chip that supports a continuous read-out scheme [64].

2.3.3 TOF upgrade

The ALICE Collaboration plans to collect interactions $\sim$50 kHz for *Pb-Pb* collisions and up to $\sim$1 MHz for *pp* collisions in the ALICE experiment. This defines new running conditions in terms of charged particle flux on the MRPCs and new requirements on data rates in the read-out electronics. During the heavy-ion run with 3.4 kHz interaction rate, a charged particle flux of 7 Hz/cm^2 was measured by the TOF. Thus, at 50 kHz interaction rate, it is expected a flux of 100 Hz/cm^2, that can be easily sustained, according to previous measurements of the intrinsic rate capability of the MRPCs. Although the current TOF read-out can sustain already rates of tens of kHz, the main aim of the TOF update programme will be to further increase the read-out rate capability for both *Pb-Pb* and *pp* interactions. The TOF read-out time depends on the multiplicity per event: the average hit multiplicity measured by the TOF for minimum bias *Pb-Pb* collisions at $\sqrt{s_{\rm NN}} = 2.76\ TeV$ is 1500 hits/event. Scaling this number to $\sqrt{s_{\rm NN}} = 5.5\ TeV$ in a very conservative way one can expect 2000 hits/event.

The first limitation to the TOF read-out rate is the time needed to transfer the data from the HPTDCs to the TRMs. The transfer of an empty event takes $\sim$3.2 μs, which is determined by the communication protocol between TRM and HPTDCs. This results in a limit on the read-out rate for *pp* of about 250 kHz and even lower for *Pb-Pb*, according to the multiplicity. The read-out rate of 250 kHz is therefore the maximum that can be achieved by the TOF and the upgrade of the rest of the electronic chain is intended to eliminate all further restrictions on this rate.

The VME read-out is currently limited to a throughput of 40 $MByte/s$. Figure 2.18 shows the TOF read-out rate as a function of VME bandwidth. At the expected hit multiplicity of 2000 for the average *Pb-Pb* collisions, the maximum for read-out is about 80 kHz. Average *pp* collisions, instead, have

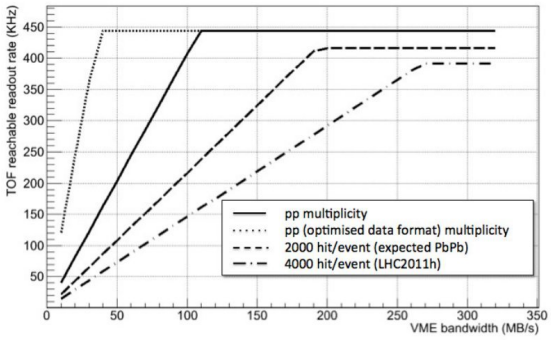

Figure 2.18: *TOF read-out rate as function of the VME bandwidth for four different running conditions as described in the legend [64].*

a lower hit multiplicity and the overhead of the data format amounts to $\frac{2}{3}$ of the total event size. The maximum read-out rate is then limited to about 160 kHz. By upgrading the firmware it should be possible to reduce the volume of the read-out control words and also to increase the data transfer rate up to 160 $MByte/s$. This would therefore remove all limits on the read-out rate from the VME.

The system analysis in 2012 and further measurements performed in 2013 showed that the read-out time of the HPTDC chips inside TRM cards sets a 250 kHz upper limit for the absolute maximum trigger rate that can be sustained by the TOF. This corresponds to the time needed to perform a full scan (see Sec. 3.1.3) of the 30 HPTDC housed in each TRM when there are no hits to be read out. Replacement of these cards (and of the HPTDC chips) is not planned in the ALICE LS2 upgrade.

Figure 2.19 illustrates the proposed new read-out scheme in the ALICE upgrade programme. The only possible hardware intervention to adapt the TOF to the upgrade environment is the production of a new DRM card, the DRM2. The current version of the DDL works at 1 Gb/s. A new link based on the ASIC GBTx chip developed at CERN with bandwidth up to 4.48 Gb/s will be deployed. The hardware upgrade will allow the use of the new GBTx link for DAQ and trigger, including a better handling of the busy signal. It is a radiation tolerant chip that can be used to implement multipurpose high speed bidirectional optical links for high-energy physics experiments [64, 83].

The upgrades discussed above are those planned to improve the TOF

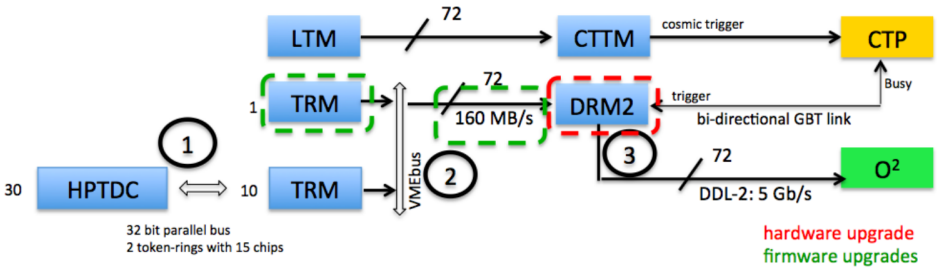

Figure 2.19: *New TOF read-out scheme, with upgraded components highlighted. The data segmentation will remain the same (i.e. the whole TOF is read-out via 72 DDL links, each corresponding to the read-out of one VME crate) [83].*

performances, according to [64], but they are not the only possible. In the following chapter, I will describe how also the TOF detector can achieve a continuous read-out. The importance of achieving a C-R/O also for the TOF detector is due to the possibility of better enlarge the statistical sample of data collected having all the three main detectors (ITS, TPC and TOF) participating. This will represent a key strength in the study of heavy-flavour particles and low-mass dielectrons.

Chapter 3

Proposal of a continuous read-out implementation in the TOF detector

Experiments in physics typically detect signals from many different events although in general they are focused on a small number of them. Triggering is therefore introduced to select a particular signal from the background and other competing events which occur almost simultaneously. To identify the interesting event, specific criteria (such as coincidence among two or more detectors, number of outgoing particles, etc.) have to be defined. When events satisfy these criteria, further operations in the detector are activated. To start its read-out, the electronic logic required for such selection is called *trigger*.

The read-out in the whole ALICE experiment was designed to be triggered. At each machine clock cycle ($\sim$25 ns), the Central Trigger Processor (CTP) evaluates trigger inputs from different detectors, elaborates the trigger decisions and eventually sends L0, L1 and L2 trigger signals as input to all the subdetectors. In particular, the L1 trigger needed to the onset of the TOF read-out is generated 260 LHC clocks ($\sim$6.5 μs) after L0. Such latency is due both to computation and propagation times. The L2 signal (for acceptance or rejection of the event) comes from the TPC in 88 μs. This delay is due to the intrinsic delay of the drift time for avalanches in the chamber.

In a *continuous* read-out scheme (C-R/O), instead, a single detector should be able to collect and read out all signals detected by the front-end electronics. In such conditions, the read-out is not dependent on an external trigger signal.

The enhancement of luminosities foreseen at the ALICE detector after the LS2 implies a significant increase of the number of events produced in the collider. The achievement of a continuous read-out may represent a great opportunity to collect large statistics, but it has to be possible to well discriminate signals of interest from the background in further steps.

The ALICE subdetectors well suit the present LHC conditions; the trigger and read-out rates do not affect single performances. Anyway, in the framework of the enhancement of luminosities foreseen for the LHC Operational Run 3, it is needed an increase of present read-out rates. Therefore, the TPC detector is upgrading to continuous read-out, while the read-out of the TOF detector is limited by the communication protocol between TRM and HPTDCs to 250 kHz.

Preliminary studies indicate that the ITS subdetector would not be able to read out at 1 MHz of interaction rate and that it could better perform at 500 kHz. Thus, the ALICE Collaboration could decide to run pp collisions at such interaction rate. It is important, therefore, to define at which conditions the TOF detector could work in continuous read-out at different frequencies of interaction rate and which would be the shortage of data collected in case it is decided to continue with the triggered R/O.

In this chapter, the possibility of achievement of a continuous read-out for the TOF detector is explored and results of data analysis and simulations performed are reported.

3.1 Front-end and read-out electronics

A schematic view of the electronics design of the ALICE-TOF detector is shown in Figure 3.1.

Front-end electronics (FEE) for the ALICE-TOF detector was designed to comply with the basic characteristics of the MRPC detector, i.e. very fast differential signals from the anode and cathode read-out pads and intrinsic time resolution better than 40 ps, with an efficiency close to 100%. The ALICE-TOF FEE has to be fast enough to collect signals from each of the 153000 MRPC pads. Front-end cards are placed inside each module of the detector. They are based on a custom Application Specific Integrated Circuit, the NINO ASIC, with 8 channels, that implements a fast amplifier and discriminator [84]. The FEE base unit is the Front-End Analogue (FEA) card (Fig. 3.2) that connects to MRPC interfaces via a Printed Circuit

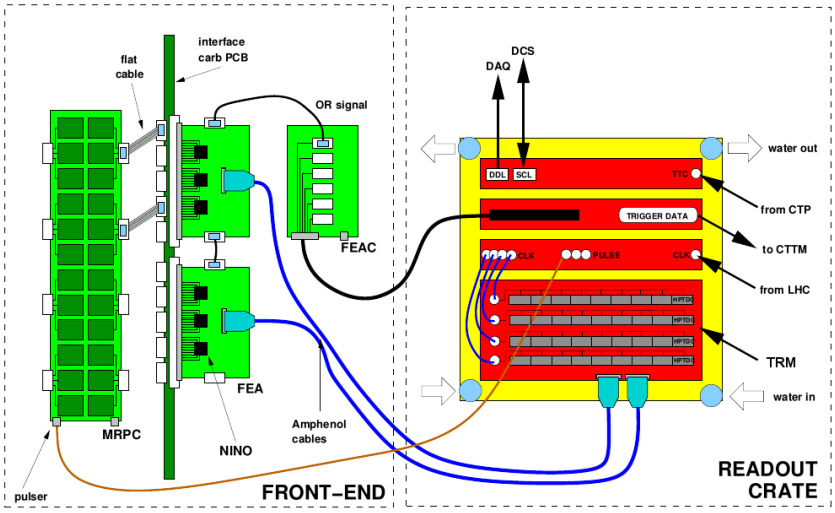

Figure 3.1: *A depiction of the electronic scheme of the ALICE-TOF detector.*

Board (PCB) connector.

Read-out electronics is located in custom crates at both ends of each supermodule in the ALICE-TOF detector and consist of 9 or 10 (right or left side crate, respectively) TDC Read-out Modules (TRMs) cards (see Sec. 3.1.3) and one Data Read-out Module (DRM) in each crate.

The DRM receives the trigger information (Level 1, Level 2-accept, Level 2-reject) from the Central Trigger Processor (CTP) via the Timing Trigger and Control receiver (TTCrx) chip and performs a slow-control func-

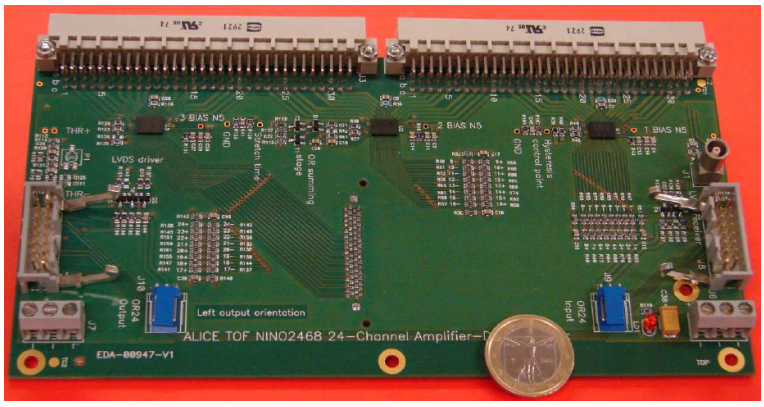

Figure 3.2: *A Front-End Analogue card. The three NINO ASIC chips are visible on the card.*

tion with a dedicated FPGA. Data from TRM are read by DRM and sent to the DAQ via the DDL optical link.

3.1.1 MRPC signal conversion

The differential signal produced on the MRPC is read, amplified and discriminated by the corresponding NINO ASIC (Application Specific Integrated Circuit) chip, hosted on a FEA card. The output from the FEA meets the Low Voltage Differential Signal (LVDS) standard. Afterwards, the LVDS signal is sent to the High Performance Time To Digital Converter (HPTDC) inside the TRM.

The amplitude of analog signal produced in the MRPC by the incident particle is related to the induced charge from the avalanche. This analog signal is converted by the NINO ASIC in a digital one (LVDS), whose width corresponds to the amplitude of the signal from the MRPC, above a certain threshold. The leading edge of the converted signal defines the time of the hit, while the time difference between leading and trailing edges defines the Time Over Threshold (TOT) and it is proportional to the amplitude of the analog signal.

When two different analog signals start at the same instant, they will exceed the threshold at two different times, not appearing simultaneous as they are (*time slewing*). By digitizing both the rising and the falling edges in

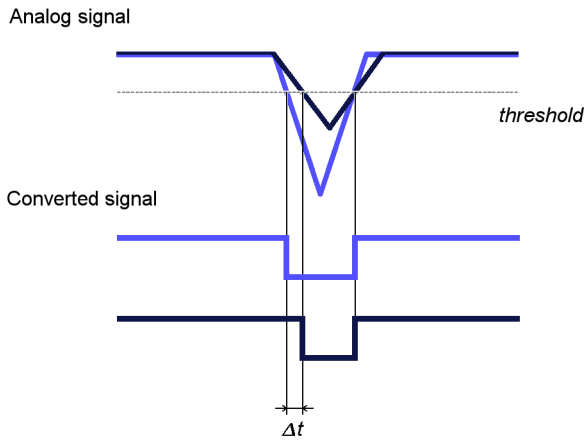

Figure 3.3: *Scheme of signal conversion and time slewing effect. The signal with lower amplitude, even if simultaneous to the other one, appears delayed by* Δt.

a HPTDC, the TOF can provide time slewing corrections without requiring an ADC per channel.

3.1.2 High Performance TDC (HPTDC)

The High Performance TDC ASIC was developed by the CERN/EP Microelectronics group for LHC applications and designed as a general purpose TDC for LHC experiments with multi-hit and multi-event capabilities. The HPTDC is said *free-running*, since data can be recorded inside its internal buffers without stopping acquisition. The HPTDC block scheme is showed in Fig. 3.4. The HPTDC uses a 40 MHz clock to fit with the LHC bunch

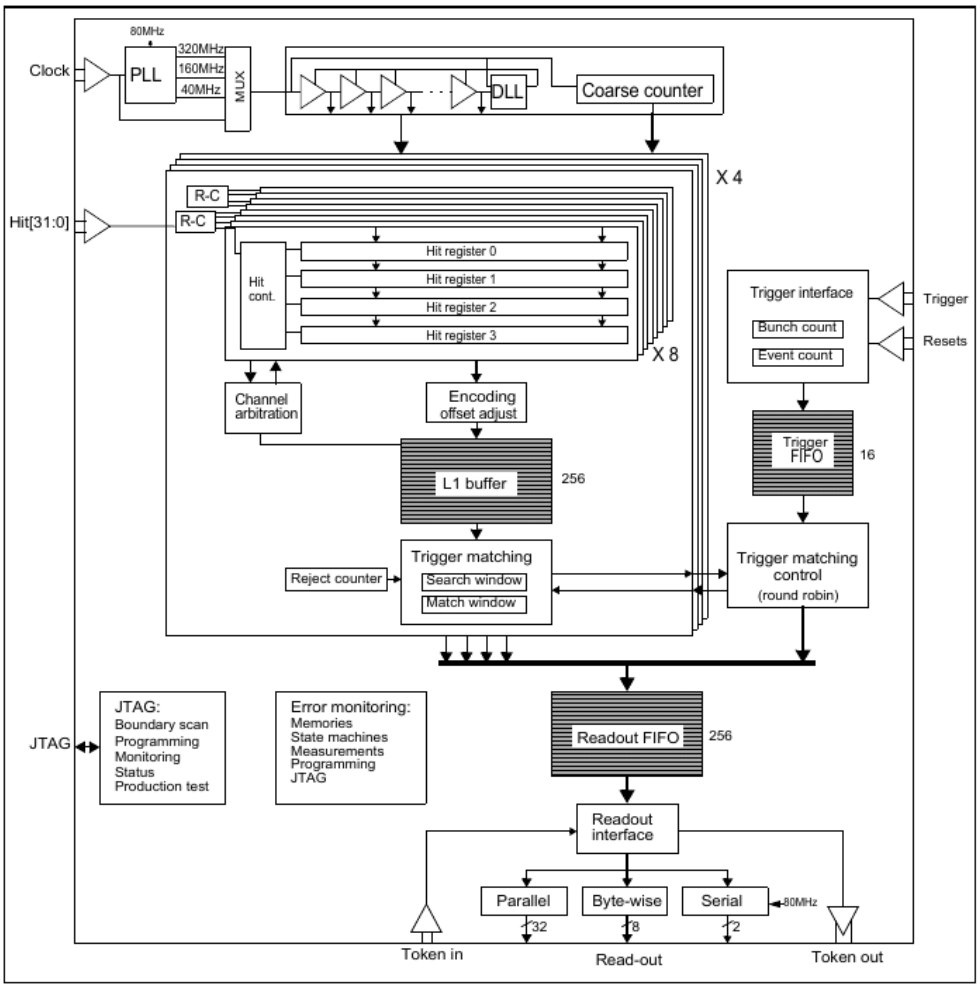

Figure 3.4: *Architecture of the HPTDC [85].*

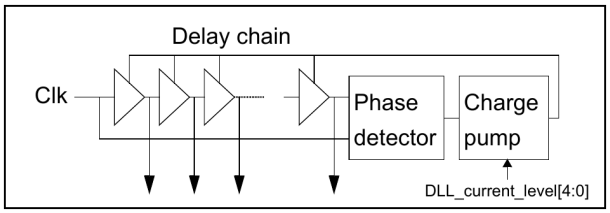

Figure 3.5: *DLL with its main components [85].*

crossing rate and it disposes of four different resolution modes obtained from the 40 MHz clock, i.e. 25 ns, 200 ps, 100 ps and 25 ps. It handles up to 32 channels, but in Very High Resolution Mode (VHRM), that corresponds to a resolution of 25 ps, the HPTDC has 8 channels only. This fits with the ALICE-TOF electronic scheme, since also the NINO ASIC handles 8 channels. Hence, each HPTDC is coupled with a NINO ASIC chip. HPTDCs store hits for each channel. Each channel can buffer 4 measurements until they are written into a 256 words deep level 1 buffer shared by a group of 8 channels. The individual channel buffers work as small derandomizer buffers before the merging of hit measurements into the L1 buffer. Measurements stored in the L1 buffer can be passed directly to a common 256 words deep read-out FIFO, or a trigger matching function can select events related to a trigger. The trigger information consisting of a trigger time tag and an event ID can be stored temporarily in a 16 words deep trigger FIFO. A time window of programmable size is available for the trigger matching to accommodate the time spread of hits related to the same event.

The 8 HPTDC channels measure the time at which the signal starts i.e. the falling edge of the LVDS square signal or *leading edge*, and the instant at which the signal ends, i.e. the rising edge or *trailing edge*. Exploiting the proportionality between the total charge and the induced signal it is possible to correlate time and charge improving the accuracy.

The operating of the HPTDC is based on a Delay Locked Loop (DLL) unit (Fig. 3.5). The time digitization is based on a clock synchronous counter and a DLL interpolator. An external 40 MHz clock is internally multiplied by a Phase Locked Loop (PLL) to feed properly the DLL to reach the required resolution. The DLL generates the basic timing signals to obtain the required time resolution and it consists of three major components:

- chain of 32 delay elements in which the delay can be adjusted by a

control voltage;

- phase detector measuring the phase error between the clock and the delayed clock from the delay chain;
- charge pump and filter capacitor generating the control voltage to the delay elements based on the measured phase error from the phase detector.

The programmable delay element replicates the digital input to the digital output with a delay related to the analog input voltage. The DLL acts like a shift register which makes a full circular shift in one clock cycle. The phase detector and the integrating circuit are implemented to lock the shift to the input clock, using a feedback principle.

3.1.3 ALICE-TOF HPTDC read-out

Figure 3.6 shows a TRM card. Each TRM is a VME slave card and houses 30 ASIC HPTDC chips, i.e. 240 channels, operating in VHRM.

The read-out for the TOF detector is completed within the first two trigger levels, as introduced in Sec. 2.2.2. In the first phase of the read-out,

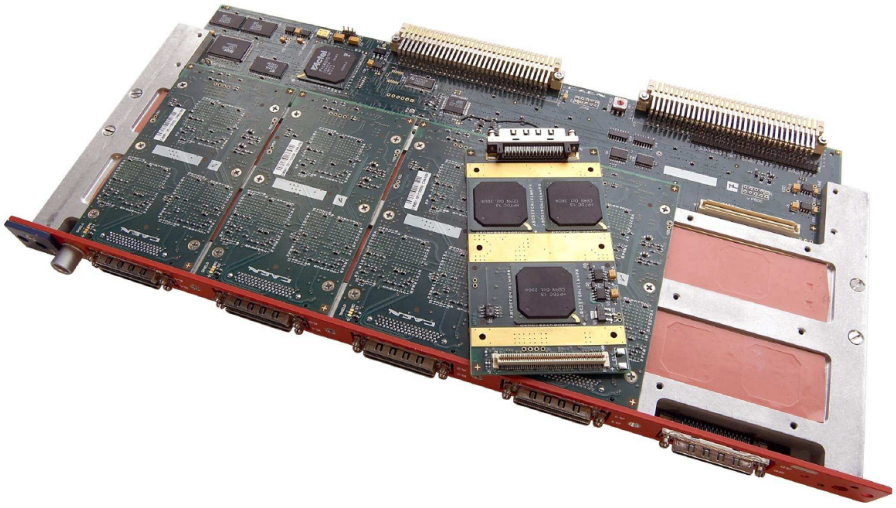

Figure 3.6: *The TDC Read-out Module (TRM). A piggy-back hosting three HPTDC chips (removed from its board) is also visible. The cooling system of the board fills the midplane of the board.*

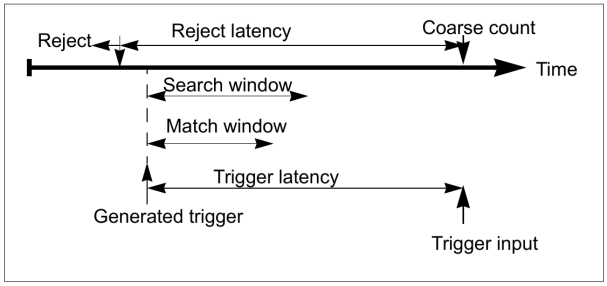

Figure 3.7: *Trigger, trigger latency and trigger window related to hits on channels [85].*

hits stored in HPTDCs are shipped to TRMs. The HPTDCs currently used by the TOF save in their internal memories all hits received from MRPC pads up to a *latency window* of 8.3 μs. The working scheme of the HPTDC read-out is shown in Fig. 3.7. When a L1 signal is received, HPTDCs set a pointer at the beginning of the latency window and check if signals are stored in their buffers by shifting them in a read-out FIFO.

Only events stored in a time window of programmable duration, the *matching window* are shifted to the read-out FIFO. The time duration of the matching window is set to 600 ns in the present R/O settings. This represents a good balance between an acceptable number of hits collected and having enough time before and after the event to be considered. More than a single L1 signal trigger can be received during a latency window. Hits occurred in the past beyond the start of the latency window expire and they are deleted if no trigger signal arrived and no matching is executed.

At the second trigger level, data are read from TRMs and moved to DRM cards. There are two possible kinds of signal for the second trigger, L2-accept and L2-reject. On arrival of a L2-reject, the event is deleted from the TRM buffer; with a L2-accept the information is transmitted to the DRM and then the event is removed from the TRM buffer. At this stage, all taken data are stored into DRM cards and they have to be sent to the central DAQ. At present, this is done via DDL links. The whole time for the VME read-out and Local Data Collector (LDC) transfer requires $\sim$15 μs per crate, that limitates the read-out rate at 65 kHz. The time for data transfer can be improved upgrading the VME protocol to VME2eSST and upgrading the optical link to GBTx as planned as already planned to happen during

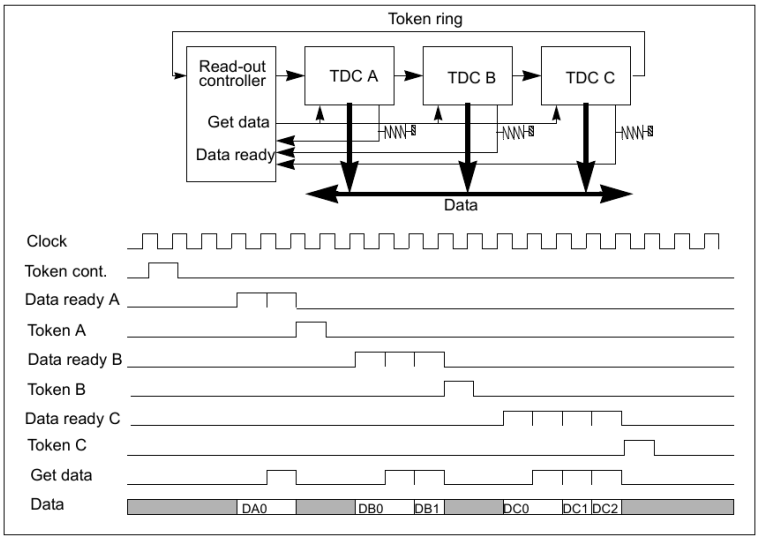

Figure 3.8: *Token based parallel read-out with all TDCs configured as slaves controlled by an external controller [85].*

the LS2.

The read-out interface used by the HPTDC for different applications depends strongly on the physical location of TDCs inside the detector on the VME boards and on the data bandwidth required. A 32 bit parallel read-out interface is available for high bandwidth read-out and it was implemented for TRMs. Read-out data are formatted in 32 bit words with a 4 bit type identifier. The communication protocol between a read-out controller such as an FPGA and HPTDC interfaces is designed as a token-passing mechanism in which a signal called token is passed between the chips. The chips are authorized to communicate at the token passage. Up to 15 chips can be chained using a clock synchronous token-passing scheme to perform local event building. The FPGA master sends the token to the first slave chip in the chain that starts to send its data. The event data from each chip typically consists of a single chip event header, accepted time measurements, error flags (if any error is detected for event being read out) and finally a single chip event trailer (if enabled). The token is then passed on to the following slave TDCs in the chain until it finally arrives at the master. The scheme of the token passing in the ALICE-TOF TRM cards is shown in Fig. 3.8. Read-out of parallel data from the TDC is performed via a clock synchronous bus. In the TRM, TDCs share one read-out bus controlled by the

circulating token.

According to [85] and to measurements performed by the Bologna ALICE-TOF group, the time needed for the token to circulate in a single chip is $\sim$100 ns. In addition, 100 ns for the access to each HPTDC chain in TRMs have to be taken into account. Therefore, considering all the 30 HPTDCs, the whole time needed for a single reading is $\sim$3.2 μs. Additional $\sim$100 ns have to be added for each hit to be read, considering both leading and trailing edges. Actually this time does not affect the TOF read-out time, due to the large latency between L1 and L2a, but it would be the dominant term during Run 3 and it cannot be reduced. It is possible to summarize the time needed for a full check of all HPTDCs with the relation that follows,

$$t \simeq 3.2\ \mu s + n_{hit} \cdot 100\ ns. \tag{3.1}$$

Assuming $n_{hit} = 8$ (3% occupancy, see Sec. 3.2), this implies a maximum read-out rate of roughly 250 kHz.

3.2 Towards a continuous read-out for the TOF

The ALICE-TOF electronics was conceived with the idea that the read-out should be synchronous depending on signals from Central Trigger Processor, as already introduced.

The enhancement of luminosities and the resulting increase of the number of events inside the collider can produce a considerable enlargement of the statistics in data collected due to expected interaction rates, that are 50 kHz and 1 MHz for *Pb-Pb* and *pp* collisions, respectively.

According to [64] and [83], once completed all the scheduled upgrades the target read-out rate for the ALICE-TOF detector will be 200 kHz, while replacement of the TRM cards would be instead unaffordable both for hardware and budget reasons. Such read-out rate is largely appropriate for future 50 kHz *Pb-Pb* collisions, but it would be advisable to improve it for *pp* and *p-Pb* collisions. Actually, the TOF would be able to collect up to just a fifth of the rate coming from all *pp* interactions in the collider. Although this would be a significant improvement with respect to current capabilities of the detector, it would be desirable to get more.

Once all the planned upgrades in the ALICE experiment were completed, the ITS detector will operate at high rate (triggered) and the TPC detector will operate with continuous read-out and the introduction of the GEM

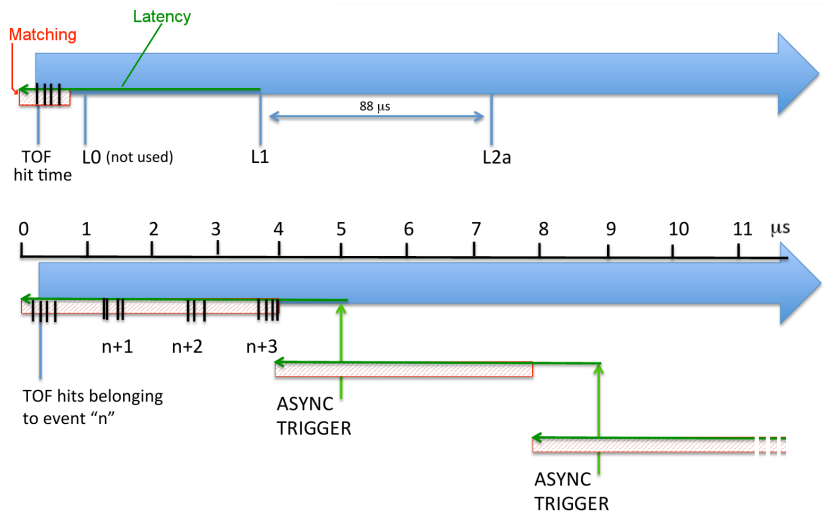

Figure 3.9: *A comparison between working schemes of HPTDC readouts. The upper part of the picture indicates the current read-out scheme, while the lower part the continuous read-out idea.*

tecnology in the TPC will cut down the latency for the L2 trigger arrival. The bottleneck in the read-out rate for the TOF detector will be given by the read-out cycle of all the 30 HPTDC chips needed at each L1 trigger arrival, which sets the maximum available rate at 250 kHz, according to the Eq. (3.1). Hits, by themselves, can be read in a relatively short time, better than the actual approximately 4 μs per cycle. In this chapter, I explored whether it is possible to separate the read-out of the hits collected, also belonging to more than one event, taking full advantage of the internal HPTDC buffers.

Figure 3.9 shows a comparison between the read-out scheme currently in use and an example of a TOF continuous read-out scheme, at 1 MHz interaction rate using a 250 kHz asynchronous[1] trigger rate. An asynchronous trigger is sent each 4 μs and the duration of the latency window is set to 5 μs. At the arrival of each trigger, a matching window of the duration of 4 μs starts 'backwards' in L1 HPTDC buffer and matches *all* the stored hits. In this way the trigger sent to HPTDC at fixed time intervals (4 μs) makes a snapshot of all the registered hits. The asynchronous matching window will contain on average all the hits belonging to 4 real events. The duration

[1]the word "asynchronous" is used here meaning a trigger not synchronized with a real event following a collision.

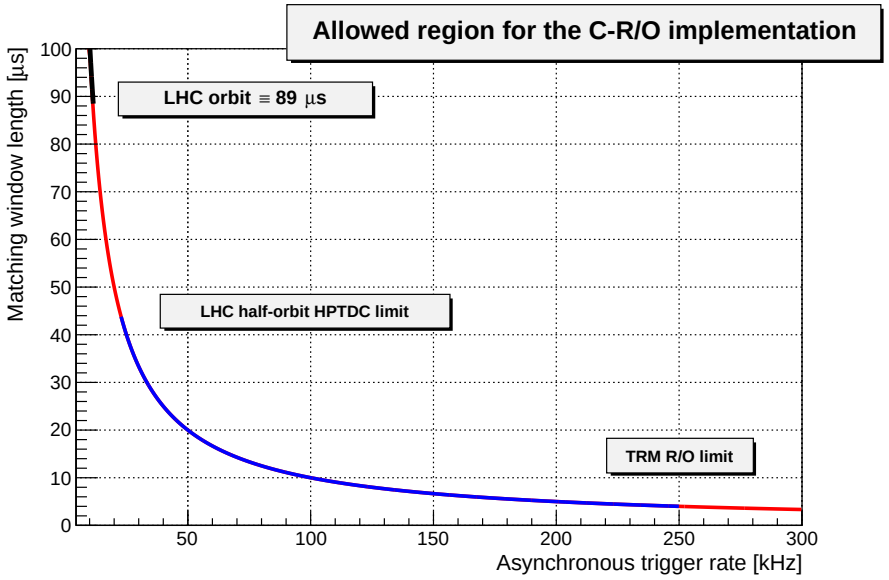

Figure 3.10: *Limitations to consider in the determination of the continuous read-out working conditions. The hyperbole is obtained from the Eq. (3.2). The allowed C-R/O region is highlighted in blue. The black region is forbidden due to the time needed by the particles for the revolution orbit inside the collider.*

of latency and matching windows and the asynchronous trigger frequency are adjustable. A critical parameter to monitor will be then the *occupancy*, i.e. the number of hits registered in a given matching window in the single TRM module. The *hit multiplicity* per event corresponds to the n_{hit} term in the Eq. (3.1). If such term becomes *too* large for the matching window considered, another bottleneck could be encountered due to the bandwidth of the bus between the HPTDCs and the TRMs. This will be better discussed in Sec. 3.2.2. Thus, the best working point of continuous read-out scheme will depend on the actual occupancy and on the number of interactions per window.

In a generalized scheme, the asynchronous trigger frequency (f_A) and the matching window duration (M_W) have to comply to the following relation

$$M_W \cdot f_A = 1, \tag{3.2}$$

also shown in Fig. 3.10, to allow the continuous read-out of the hits in the detector. The limitations to consider for such conditions to remain valid

are the maximum asynchronous trigger rate i.e. the TRM read-out limit (250 kHz) and the LHC orbit time per particle (89 μs). Due to limitation in the matching algorithm of the HPTDC, in fact, it is not possible to read backwards in buffers over a time equivalent to more than a half of the LHC orbit. The working point for continuous read-out in the proposed scheme will stay therefore on the hyperbole drawn by the relation in the Eq. (3.2) between 44 μs and 4 μs or equivalently between 22.73 kHz and 250 kHz.

3.2.1 Data characterization of events recorded in the ALICE-TOF detector

In the current read-out scheme, matching windows are very tight (only 600 ns) and comprehend solely one interaction event with an almost flat background[2]. This situation is very different with respect to the framework of the proposed C-R/O scheme and of the interaction rates expected from LHC Operational Run 3. At 1 MHz pp collisions, with a typical 10 μs matching window, the interactions expected would be 10 per matching window.

Figure 3.11 shows the time distribution of the hits in a TOF matching window from a run of the LHC10d data taking (run number: 126432; pp collisions) at $\sqrt{s} = 7\,TeV$. The interactions were triggered with a minimum-bias trigger, that is a very minimal requirement (1 hit in the SPD or in the V0 detector) corresponding to at least 1 particle in the central barrel region of the detector. In the triggered read-out scheme, the hits belonging to the triggered event occur within 200 ns and occupy the time between 200 ns and 400 ns after the beginning of the matching window. This defines an *interaction window*, used then for the simulation (see Sec. 3.3). A *background window*, instead, is defined by considering signals arriving in the final 200 ns. Such signals are due only to the background and their particularly regular shape corresponds to *noisy* hits synchronized with the main LHC clock. In the upper part of Figure 3.13 it is shown the pattern for signals collected, while backgrounds taken for sampling in the simulation are reported on the lower part of the figure.

The multiplicity observed in background and interaction windows are used to construct the TOF multiplicity for a given interaction rate and a

[2]Already during Operational Run 2, however, due to the increase of the filling scheme of the beams at the LHC it is possible to have additional interactions within the current matching window.

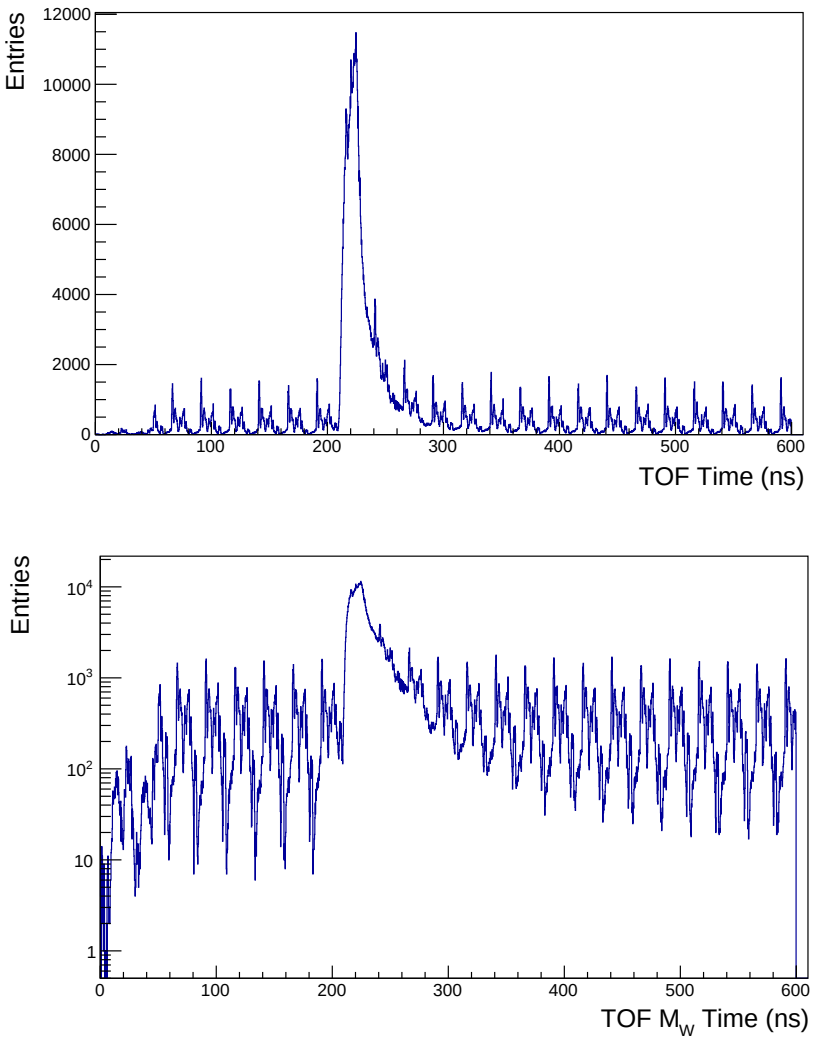

Figure 3.11: *Data taken by the TOF in a* 600 ns *matching window in the current read-out scheme, in linear scale (on the top) and in log scale (on the bottom) (data from run 126432, LHC10d period).*

given matching window length in the simulation performed. Figure 3.12 shows (on its top) the total TOF multiplicity measured in the LHC10d run considered so far. The TOF multiplicity for interaction signals and the TOF multiplicity for signals composing the background are also shown. While the result for the background window may vary depending on the noise conditions in the detector, the result for the interaction window is quite

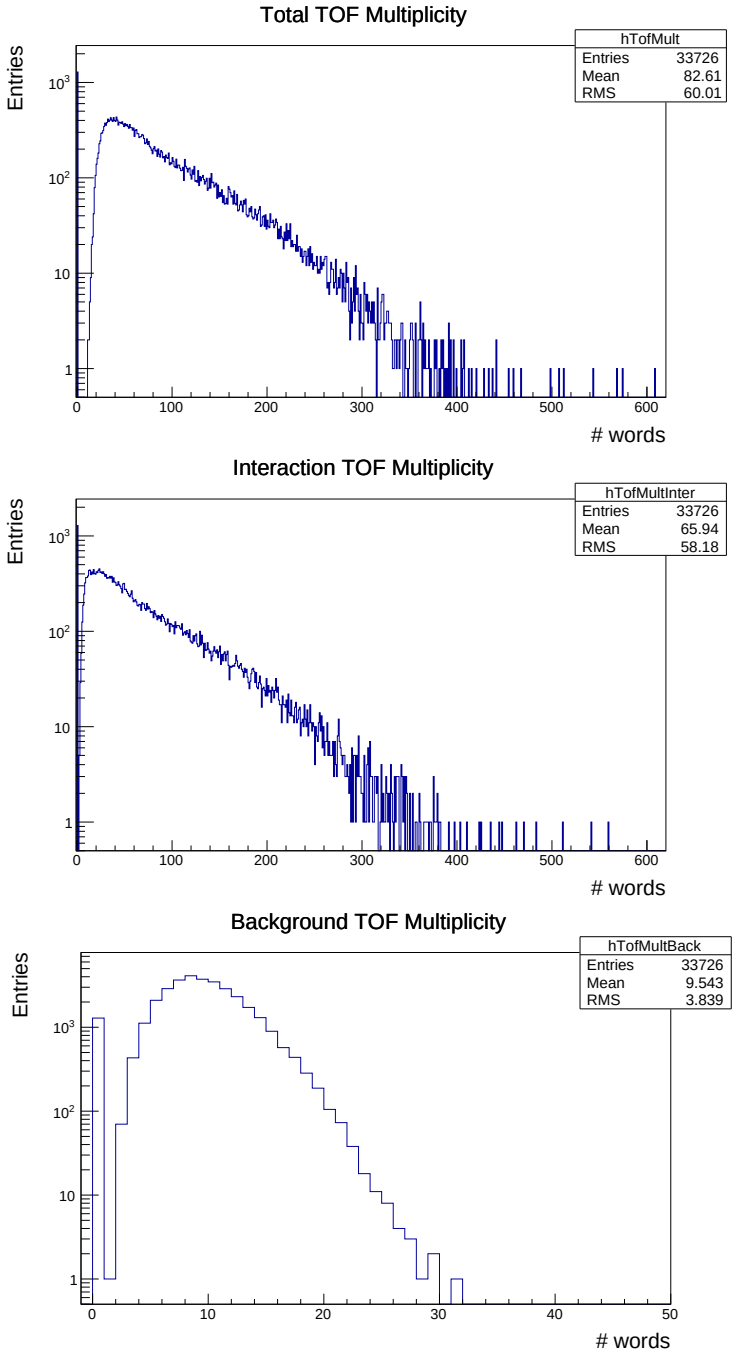

Figure 3.12: *The total multiplicity measured in the TOF detector (on the top). The total multiplicity in the interaction window and in the background window are also shown on the middle and on the bottom (data from run 126432, LHC10d period).*

constant and driven by the physics, that is by the multiplicity of the *pp* interaction triggered with a minimum bias trigger.

Histograms in Figure 3.12, like others that follow, do not simply represent the physical hits detected in the TOF, but all signals arriving from the TRMs including the noise and eventually other criticalities. In the ALICE-TOF R/O scheme, data are formatted in 32 bit words. An event to be detected will comprehend several hits, each containing a leading and a trailing edges. Such signals are encoded in 32 bits, i.e. in a single word each. A physical hit includes therefore two words. Noisy signals can include a different number of words, that is a leading without a corresponding trailing and viceversa. The study that I present is made by considering the single

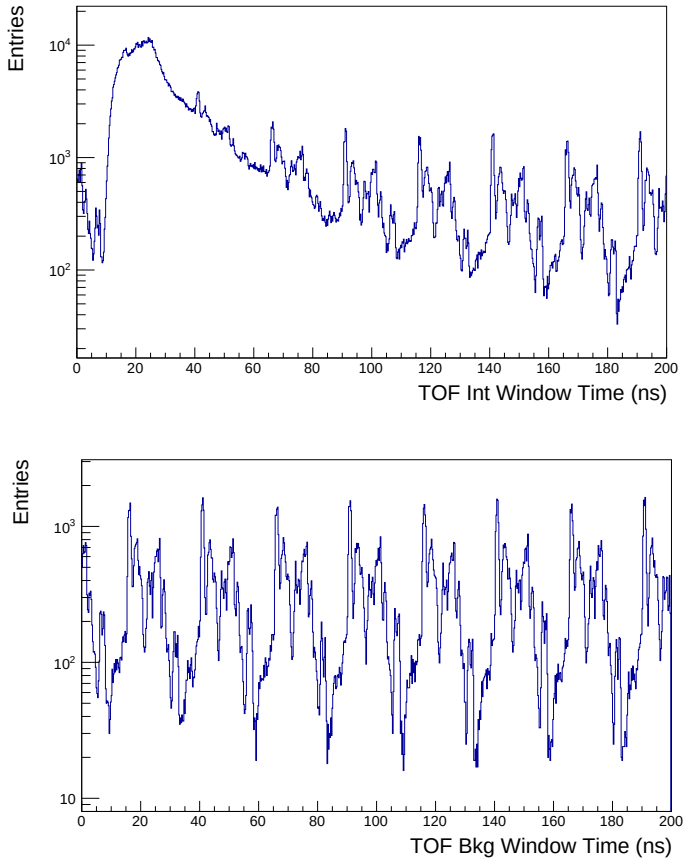

Figure 3.13: *Hit time distribution of the signals registered in the interaction window (top) and the in the background window (bottom) (data from run 126432, LHC10d period).*

words coming from the HPTDCs rather than just the full hits detected in order to better study the bandwidth occupancy in the TOF R/O electronics and, as a consequence, in order to perform a more reliable simulation.

3.2.2 Preliminary considerations

As already introduced, a crucial limitation to the read-out is represented by the bandwidth for communications in crates and inside TRMs. In this section I will present some estimations to check if the proposed scheme of continuous read-out seems affordable.

Crate bandwidth

An implementation of the 2eSST VME standard specifications, in the TRM slave cards showed that the maximum speed allowed on the bus is 160 MB/s [86]. This sets in turn a limitation to the number of bytes that can be transferred per event in the crate, N_{Cr}, as

$$(240[B] + N_{Cr}[B]) \cdot f[kHz] < 160 \left[\frac{MB}{s}\right], \tag{3.3}$$

where f indicates the rate of events expected. The 240 bytes set as an offset represent the header and trailer data (generated by each TRM) per crate that are transferred in each event. Each TRM generates 6 words (i.e. 24 bytes) for each event, also in case of empty events. Since the TRMs are 10, the offset is 240 bytes. Considering 32 bit words it is possible to write the previous relation as

$$N_{Cr}^{words} < \frac{40}{f} \cdot 10^3 - 60, \tag{3.4}$$

where the term N_{Cr}^{words} indicates the maximum number of words able to be transferred in the crate, given the maximum VME bandwidth. This sets also the limitation for the maximum number of hits allowed per event and depending on the event rate f, since each HPTDC produces two 32 bit words for each hit. Considering different frequencies it is then possible to obtain the maximum number of hits (per crate) to be handled as showed in Table 3.1.

f	50 kHz	100 kHz	200 kHz
N_{Cr}^{words}	740	340	140

Table 3.1: *The number of transferred words allowed per crate at different event rates.*

For a typical matching window of 10 μs, interactions and background can occupy up to 340 words per crate, that corresponds to 170 hits allowed per crate per matching window. Figure 3.14 (on the upper part) shows the crate multiplicity for the same LHC10d run previously analyzed for both interaction and background windows. For matching windows of 600 ns, the mean number of hits transferred per crate is ∼1.2. If one condiders a continuous read-out with 10 μs of asynchronous trigger rate, the number of hits to be transferred per crate becomes ∼20, that is very far with respect to the estimated bandwidth limit from Eq. (3.4) and numbers derived in Table 3.1.

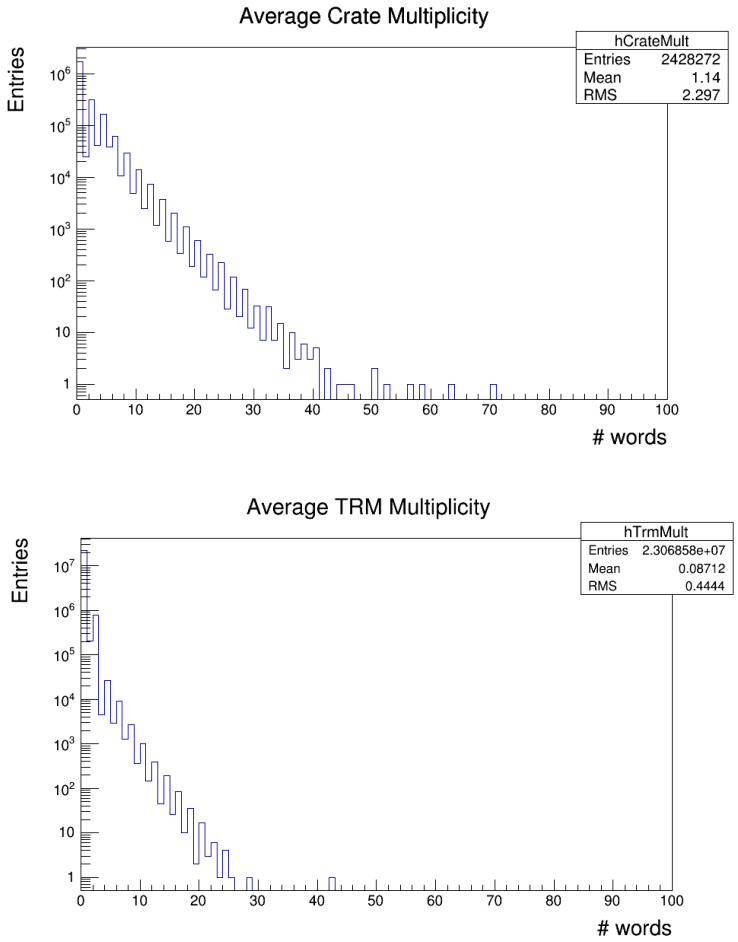

Figure 3.14: *On the top: the crate multiplicity for a single matching window. On the bottom: the TRM multiplicity (data from run 126432, LHC10d period).*

TRM bandwidth

Analogue considerations can be done for the bus for data transfer between the HPTDCs and the TRMs. The time for the HPTDC read-out is 3.2 $\mu s +$ (50 $ns \cdot word$). Therefore, the maximum number of words to be transferred per TRM in a time corresponding to the M_W will be given by the following relation

$$N_{TRM}^{words} < \frac{(M_W - 3.2\ \mu s)}{50\ ns} \cdot 10^3, \tag{3.5}$$

where M_W is the length of the matching window in microseconds and 3.2 μs is the time needed for the token ring inside HPTDCs. Considering different matching window durations, it is possible to determine an estimation of the number of words allowed to be transferred inside a TRM as shown in Table 3.2.

The plot on the lower part of Fig. 3.14 shows the multiplicity of hits per TRM. Again, considering a typical matching window of 10 μs, the number of words allowed to travel in the bus is 136, which corresponds to 68 hits. The mean number of hits per TRM (Fig. 3.14, on bottom), instead, is ∼0.1 with $M_W = 600\ ns$. Scaling this number to a M_W of 10 μs, one obtains ∼1.7 hits per TRM, that is widely contained in the limit of 136 words (Tab. 3.2).

From these preliminary considerations, the C-R/O scheme seems therefore sustainable. I will discuss as I implemented a simulation to further test the model, in Sec. 3.3.

3.2.3 Multiplicity estimate for the LHC Runs 3 and 4 at $\sqrt{s} = 14\ TeV$

In this work I will present results obtained from several simulations of data taking in a C-R/O scheme. Such results are based on real data taken from runs at the LHC and corresponding to different centre-of-mass energies for pp collisions, at 7 TeV, 8 TeV and 13 TeV. However, pp collisions at 14 TeV centre-of-mass energy are expected for the LHC Run 3, in 2020.

f	20 μs	10 μs	5 μs
N_{TRM}^{words}	336	136	36

Table 3.2: *The number of travelling words allowed per TRM at different matching window lengths.*

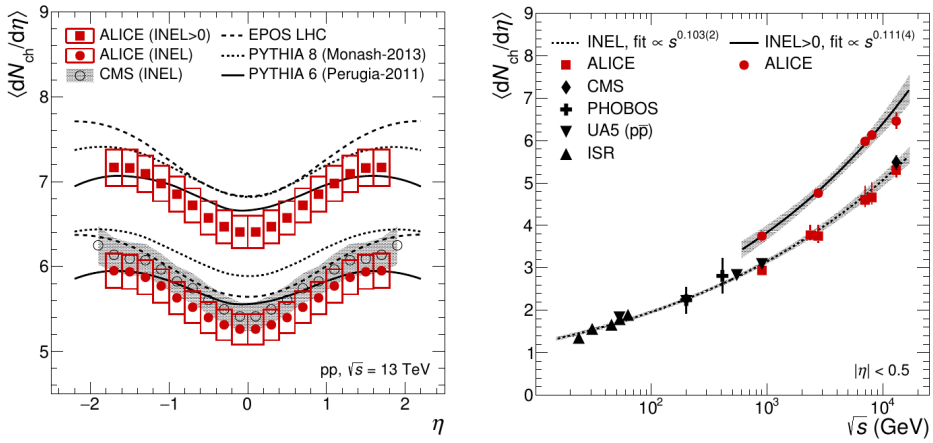

Figure 3.15: *Average pseudo-rapidity density of charged particles as a function of η (on the left) and charged-particle pseudo-rapidity density measured in the central pseudo-rapidity region $|\eta| < 0.5$ (on the right) for events produced in* pp *collisions at $\sqrt{s} = 13\ TeV$ for INEL and INEL>0 event classes and compared to Monte Carlo calculations. In both sides, the uncertainties are the quadratic sum of statistical and systematic contributions. The shaded regions in the right side plot represent the standard deviations from the fits [87].*

From the considerations made in Sec. 1.3.1 about the multiplicity for pp collisions, the number of particles produced does not increase proportionally to the centre-of-mass energies of the collision, but it scales as $ln(s)$ [25]. This leads to the following rough extimation

$$\left.\frac{dN_{ch}}{d\eta}\right|_{[14\ TeV]} = \frac{ln[14\ TeV]^2}{ln[13\ TeV]^2} \cdot \left.\frac{dN_{ch}}{d\eta}\right|_{[13\ TeV]} \approx \left.\frac{dN_{ch}}{d\eta}\right|_{[13\ TeV]}, \qquad (3.6)$$

whereby the increase of particles produced with the increase of the centre-of-mass energy from 13 TeV to 14 TeV would be negligible ($\sim$0.5%).

Figure 3.15 shows results recently published [87] by the ALICE Collaboration at $\sqrt{s_{\rm NN}} = 13\ TeV$. The multiplicity per unit of pseudo-rapidity as a function of the pseudo-rapidity and its dependence on the centre-of-mass energy are shown. Results are presented for two event classes: inelastic events (INEL) and events with at least one charged particle in the pseudo-rapidity range $|\eta| < 1$ (INEL>0), that is the class of importance for the TOF detector.

The left side of the Figure shows the average pseudo-rapidity density of charged particles in the pseudo-rapidity range $|\eta| < 1.8$, corresponding to the entire barrel. The average value for the pseudo-rapidity range $|\eta| < 0.5$

is reported and it is

$$\left.\frac{dN_{ch}}{d\eta}\right|_{|\eta|<0.5,\ [13\ TeV]}^{INEL>0} = 6.46 \pm 0.19, \tag{3.7}$$

where the total uncertainty is determined by adding in quadrature all the contributes.

The TOF covers the $|\eta| < 0.9$ pseudo-rapidity range. One can assume as the maximum possible value for the average pseudo-rapidity density of charged particles in the INEL>0 event class the value

$$\left.\frac{dN_{ch}}{d\eta}\right|_{\eta=0.9,\ [13\ TeV]}^{INEL>0} \approx 6.9, \tag{3.8}$$

that be can be extimated by interpolation in the plot in the left side of the Fig. 3.15. If the uncertainty on such number can be calculated like in the Eq. (3.7), the maximum density of charged particles i.e. the higher value in the uncertainty range[3] for pseudo-rapidity unit for the TOF at $\sqrt{s_{\rm NN}} = 13\ TeV$ will be

$$\left.\frac{dN_{ch}}{d\eta}\right|_{\eta=0.9,\ [13\ TeV]}^{INEL>0,\ [up]} \approx 7.1. \tag{3.9}$$

In the right side of Figure 3.15, it is shown the evolution with centre-of-mass energy for pp collisions at different collider experiments for charged-particle pseudo-rapidity density measured in $|\eta| < 0.5$ for the INEL and INEL>0 results. The energy dependence of $\langle \frac{dN_{ch}}{d\eta} \rangle$ is parameterised by the power law as^b fitted to data, where a and b are free parameters and s is the first Mandelstam's variable. The fit results assume that the uncertainties at different centre-of-mass energies are independent, which is not strictly the case. The obtained value for b in the INEL>0 class is

$$b = 0.111 \pm 0.004, \tag{3.10}$$

while a can be extimated from the central value in the Eq. (3.7) and it is

$$a = 0.789. \tag{3.11}$$

The pseudo-rapidity density of charged particles expected in 14 TeV collisions for the pseudo-rapidity range $|\eta| < 0.5$ can be thus extimated from the

[3] A superscript $[up]$ will be used from here in advance to indicate the higher value in an uncertainty range.

power law from the fit in the right side of Fig. 3.15 as

$$\left.\frac{dN_{ch}}{d\eta}\right|_{|\eta|<0.5,\ [14\ TeV]}^{INEL>0} = 6.57. \tag{3.12}$$

This number represents the mean for the pseudo-rapidity density in the range $|\eta| < 0.5$, expected at $\sqrt{s_{\rm NN}} = 14\ TeV$. Besides the scaling in energy, another adjustment is needed i.e. the scaling to the maximum value of charged particles per pseudo-rapidity unit for the TOF detector. If the ratio between the values in Eq. (3.9) and Eq. (3.7) in the case of 14 TeV collisions is the same than for 13 TeV collisions as it is expected, i.e.

$$r^{INEL>0} = \frac{\left.\frac{dN_{ch}}{d\eta}\right|_{\eta=0.9,\ [13\ TeV]}^{INEL>0,\ [up]}}{\left.\frac{dN_{ch}}{d\eta}\right|_{|\eta|<0.5,\ [13\ TeV]}^{INEL>0}} = 1.099, \tag{3.13}$$

this will be also the ratio between the values in $|\eta| < 0.5$ and $\eta = 0.9^{[up]}$ at 14 TeV collisions. Therefore, the maximum value for the pseudo-rapidity density of charged particles expected in the TOF will be

$$\left.\frac{dN_{ch}}{d\eta}\right|_{\eta=0.9,\ [14\ TeV]}^{INEL>0\ [up]} = r^{INEL>0} \cdot \left.\frac{dN_{ch}}{d\eta}\right|_{|\eta|<0.5,\ [14\ TeV]}^{INEL>0} = 7.22. \tag{3.14}$$

To validate the C-R/O scheme that I present in this work for the LHC Operational Runs 3 and 4, it is necessary to understand if the multiplicity is expected to significantly increase given the centre-of-mass energy. As discussed before and given the functional dependence ($\propto ln(s)$), this should not be the case. To verify this, the scaling factor F for the event class INEL>0 can be defined and easily calculated via

$$F = \frac{\left.\frac{dN_{ch}}{d\eta}\right|_{\eta=0.9,\ [14\ TeV]}^{INEL>0,\ [up]}}{\left.\frac{dN_{ch}}{d\eta}\right|_{\eta=0.9,\ [13\ TeV]}^{INEL>0,\ [up]}} = 1.017. \tag{3.15}$$

This indicates an enhancement of multiplicity between 13 TeV and 14 TeV collisions less than the 2%, almost negligible as expected.

3.3 Simulation of the C-R/O in the TOF detector

Once completed all the preliminary studies, I conducted a more in-depth analysis on the feasibility of switching to a continuous read-out for the ALICE-TOF detector. The simulation was performed using the `AliRoot` package. The foreseen occupancy was obtained adopting different asynchronous trigger rates and corresponding matching windows. The core of the simulation (see Sec. 3.3.3) has been developed in a specific macro, while other macros were written for the analysis of raw data from runs and further analyses and controls.

As preliminary operations, raw data files corresponding to physics runs collected by ALICE were given as input to a first `AliRoot` macro. Such macro was written to produce a single `.root` file extracting the time distribution and the word multiplicity for the whole detector, in the crates and for the TRMs. The word multiplicity in the interaction and background windows (as they were defined in Sec. 3.2.1) at these three levels were also inspected. At this step, an accurate analysis on time and multiplicity distributions of single crates was done (see Sec. 3.3.1). In addition, an analysis of multiplicity of single TRMs was implemented and its results are reported in Sec. 3.3.2.

As an input parameter of the macro, a variable was set to require the connection to the Online Conditions DataBase (OCDB). The OCDB contains calibration and alignment data to analyze ALICE data and, in particular, maps of hits judged noisy following post-data taking analysis. It is important to remark that this analysis was performed twice for each run considered, i.e. considering the channels with and without noise suppression optimized by connecting to the OCDB. While the use of the OCDB allowed to study the differences between noisy and filtered signals, the analysis of non filtered signals allowed to treat the whole amount of data from the detector and to fix more realistic modelization of the data amount to be transferred.

3.3.1 Single crate analysis

As it was already introduced, part of preliminary studies and some considerations on the simulation have been carried out by considering that the behaviour of a single crate could be estimated as the average behaviour

of all the crates. The ALICE-TOF crates are disposed at both ends of each supermodule and they contain the R/O electronics, as described in Sec. 2.2.2.

The whole number of crates is 72, numbered from 0 to 71. In the ALICE reference system the side close to the Muon Absorber is named C-Side and the one in the opposite direction is named A-Side. In each supermodule, 2 crates are on A-Side and 2 crates are on C-Side.

The `Root` macro described above produces a `.root` file containing informations from raw data such as the total multiplicity at the three depth levels and time and distribution multiplicity for single crates. As a result, two histograms per crate were produced. This allowed to monitor the response of each crate for each LHC physics run analyzed and to validate the approximation assumed so far.

As an example, in Figure 3.16 the multiplicity for two different crates in the LHC10d run so far considered is shown. The crate #10 showed a very regular behaviour, while the crate #17 showed some noisy issues. Background noise in crates can be due to several factors. Faulty contacts in the electronics, or a random instability in high voltage supply or electrical contacts from groundings of different subdetectors, for example, can produce electrical discharges. Such discharges may propagate along the whole frame of the detector and travel to interfere with the electronics of single subdetectors. As a result, multiplicity distribution for some crates show in correspondance unregolar shapes and the unexpected mean value on the multiplicity distribution. It is also possible to see that lots of leading edge signals are generated without the corresponding from trailing edges. Figure 3.17 shows the time distribution for a crate with regular signals and for a crate presenting a large amount of noise. It can be seen that the time distribution for a crate affected by noise is almost flat, while in noise-free cases the hits are condensed in the interaction region, with just few hits contributing to the background.

In the considerations made so far, I showed results from only two crates and for a single run (see Sec. 3.2.1). However, an analysis on all the 72 crates was also performed for three runs from three different data taking periods, i.e. LHC10d, LHC12d and LHC15f, all corresponding to *pp* collisions[4] and

[4]In the notation used at ALICE to indicate different periods of data taking, the two numbers indicate the year while the final letter indicates approximately the month.

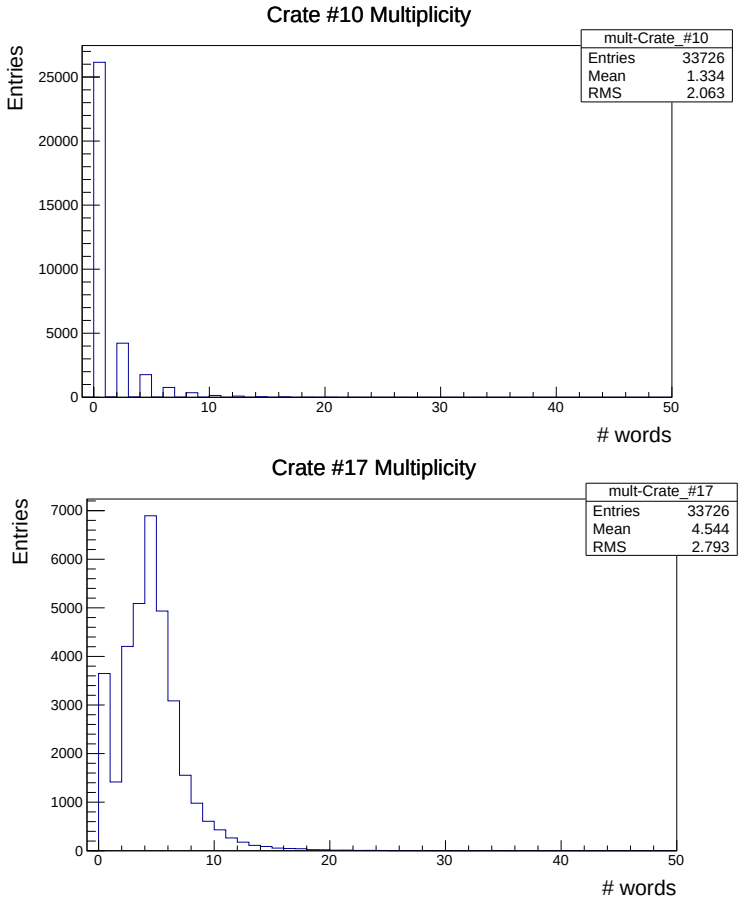

Figure 3.16: *Crate multiplicity from the analysis of a LHC10d run without noise subtraction. Two different cases are shown: a crate presenting a regular behaviour (on the top) and a crate with some noisy signals (on the bottom).*

with increasing energies, i.e. with $\sqrt{s}[2010] = 7\ TeV$, $\sqrt{s}[2012] = 8\ TeV$ and $\sqrt{s}[2015] = 13\ TeV$. In the figures that follow in this section, the mean multiplicity values for all the crates are showed. Sometimes it could be happened that some crates have been turned off during the data taking. Such crates are therefore not reported in figures, nor taken into account for all further calculations, e.g. for the determination of the average multiplicity value of all crates.

In Figure 3.18, the mean values for all the active crates in a OCDB unfiltered LHC10d run are shown. Error bars are obtained by calculating the standard error, i.e. $err = \frac{\sigma}{\sqrt{N}}$. The study for the multiplicity of single

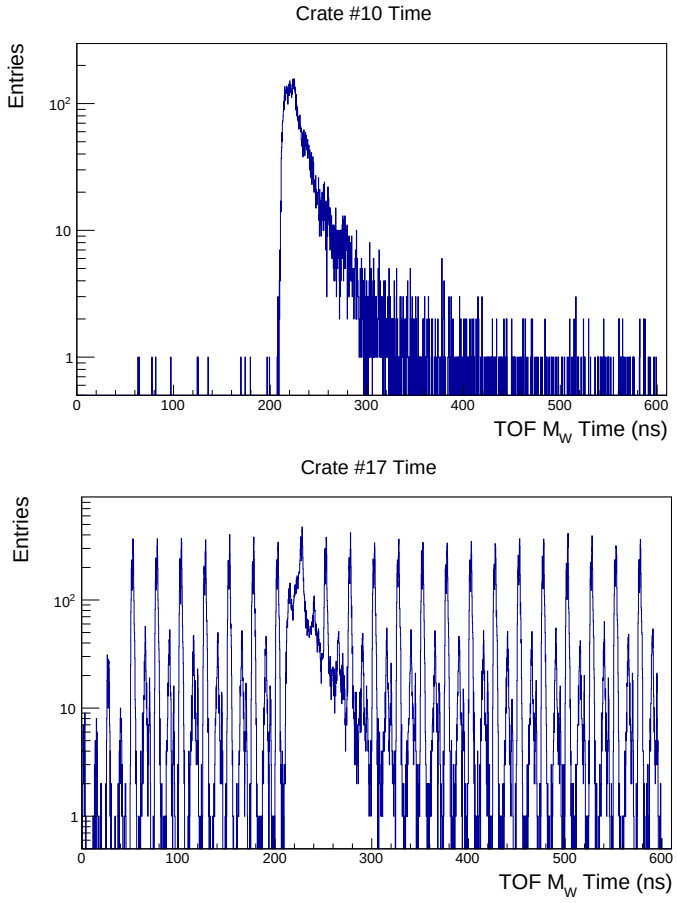

Figure 3.17: *Time distribution from the analysis of the same LHC10d run and the same crates as in Fig. 3.16.*

crate for each side of the detector is also reported. The difference between the multiplicity of the single crates and the average of all the values is widely acceptable, although the average multiplicity differs appreciably (from 0.94 to 1.38) between A-Side and C-Side crates. This is due to the presence of the front absorber of the Muon Spectrometer close to the C-Side part of the TOF. The absorber is designed for the absorption of pions in the forward region, but it also produces backscattering towards the barrel region. The analysis on the multiplicity of single crate has been carried out also for OCDB filtered data from the same LHC10d run considered so far. Such results for the same LHC10d run are shown in Figure 3.19. Furthermore, the same analysis on single crate multiplicity was performed also for data

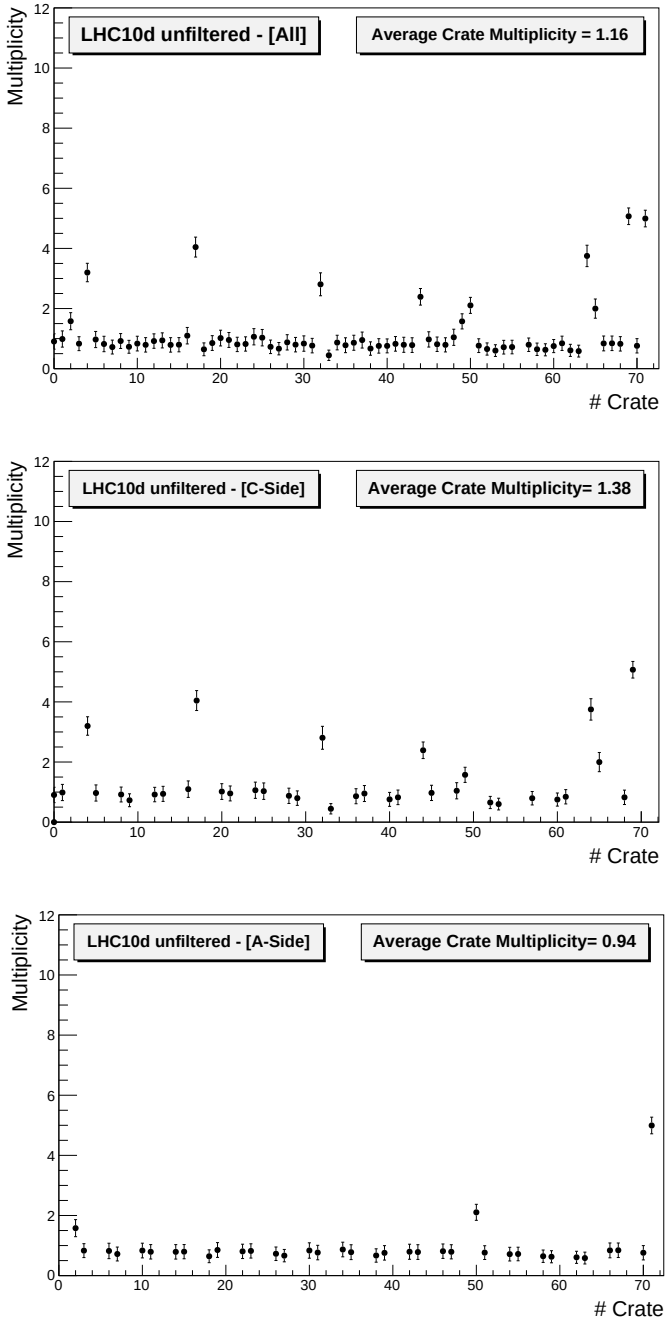

Figure 3.18: *Average multiplicity for all the active crates in a LHC10d run without the noise subtraction. The red line indicates the arithmetic mean of the multiplicity of all the active crates. In the middle and in the bottom parts, the average multiplicity for C-Side crates and for A-Side crates are shown.*

from LHC12d and LHC15f runs. The analysis between the two sides of the detector for data from all other runs considered confirmed the considerations above, and corresponding plots are not reported here.

Figures 3.20 and 3.21 show the average crates multiplicity for the LHC12d and LHC15f runs, both with and without use of the OCDB. It is possible to note a significant difference between the OCDB data filtering in the three different periods. In LHC10d, the filtering seems almost ineffective, while in LHC15f the noise suppression looks particurlary efficient and multiplicity of filtered data appear rather low. The average value for the multiplicity seems somehow low also for the the 2015 unfiltered data when compared to previous runs in 2010 and 2012. This is likely due to the maintenance efforts of the detector during the 2013÷2014 Long Shutdown 1 (LS1) which reduced the noise contributions to the signals. The maintenance campaign included reworking of defective HV connectors for example. The *raw* detected multiplicity is not completely indicative of the physics of the interactions occurring within the detector, although the expected multiplicity due to hit matched to physical tracks has to increase with the energy of the collisions, as said above. The detected multiplicity in fact can be affected by several effects of noise or background. However, for the study on the feasibility of the transition to a continuous read-out also for the TOF detector, it is important to study the multiplicity of data as they are detected.

From the figures showed in this section, it is possible to observe that the assumption made on the average seems reasonable for the crates. Sometimes there are crates which take unusual high values, even three or four times larger than the average, often in the case of non filtered data, as it is shown for the LHC15f data. The point corresponding to the crate #45 in LHC12d unfiltered data seems to correspond to a highly unlikely situation, with several channels extremely noisy. Of course, the value for such point was reduced by the OCDB filtering. In Figure 3.22 details on time distribution and multiplicity are showed. The time distribution confirms that the hits collected are heavily affected by noise. This suggests an infrequent malfunction of the electronics or the MRPC, which in any case must be avoided during future data takings. In the whole process of the ALICE data acquisition, signals like those evidenced are typically discarded *offline* by control systems such as querying the OCDB and, where necessary, filtered during the software analysis. Channels detected as noisy repeatedly during

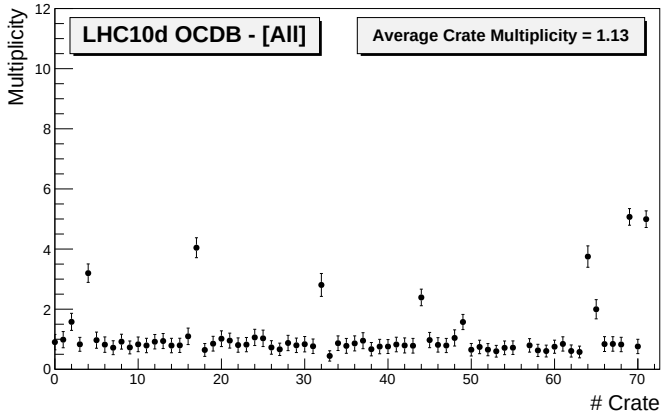

Figure 3.19: *Average multiplicity for all the active crates with noise subtraction for the LHC10d run already considered in Fig. 3.18.*

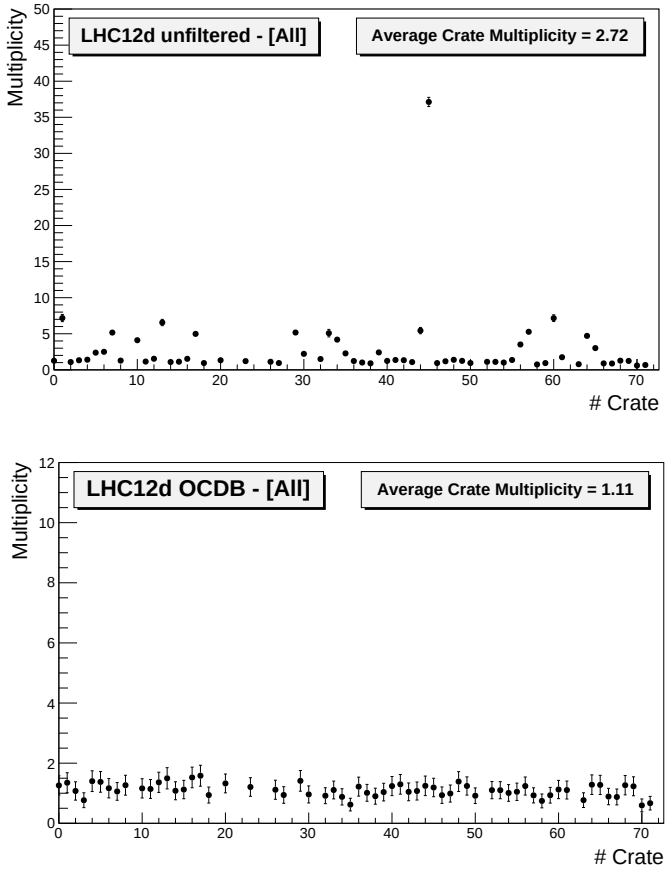

Figure 3.20: *Average multiplicity for all the active crates with and without noise subtraction for a LHC12d run.*

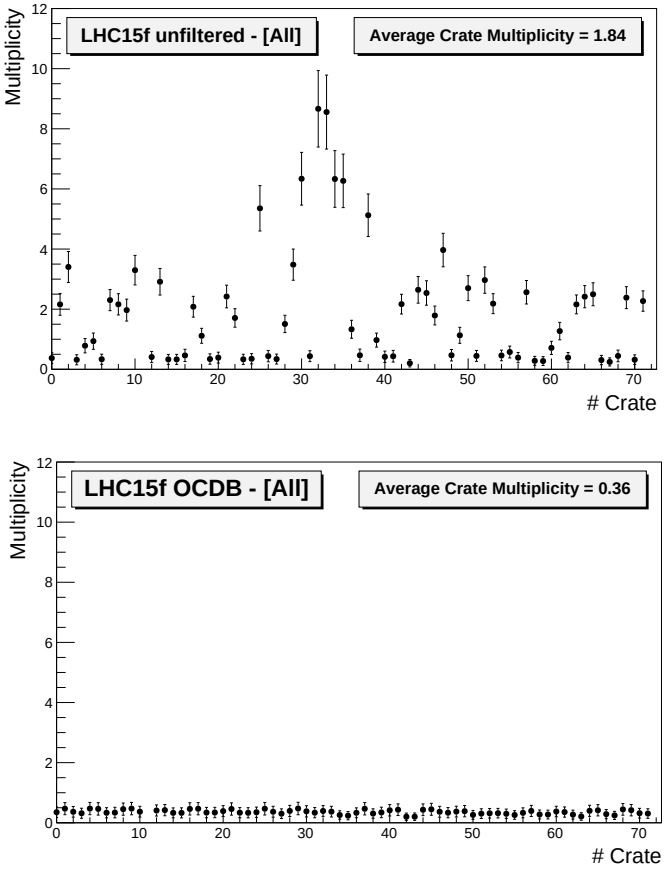

Figure 3.21: *Average multiplicity for all the active crates with and without noise subtraction for a LHC15f run.*

a period are currently turned off. This is possible acting on HPTDC configuration. In the framework of a continuous read-out, the crates affected by noise or that produce completely irregular signals could overcome their allowed bandwidth in buses before the offline data filtering system could act. It would be therefore desirable to implement an *online* data filtering system for noisy chambers able to quickly disable those channels if they show up.

3.3.2 Single TRM analysis

The electronics of the TOF detector was introduced in the Chapter 2 and detailed at the beginning of the present Chapter 3. The signal form the HPTDC is read by the TRM, i.e. the TDC Read-out Module. Each

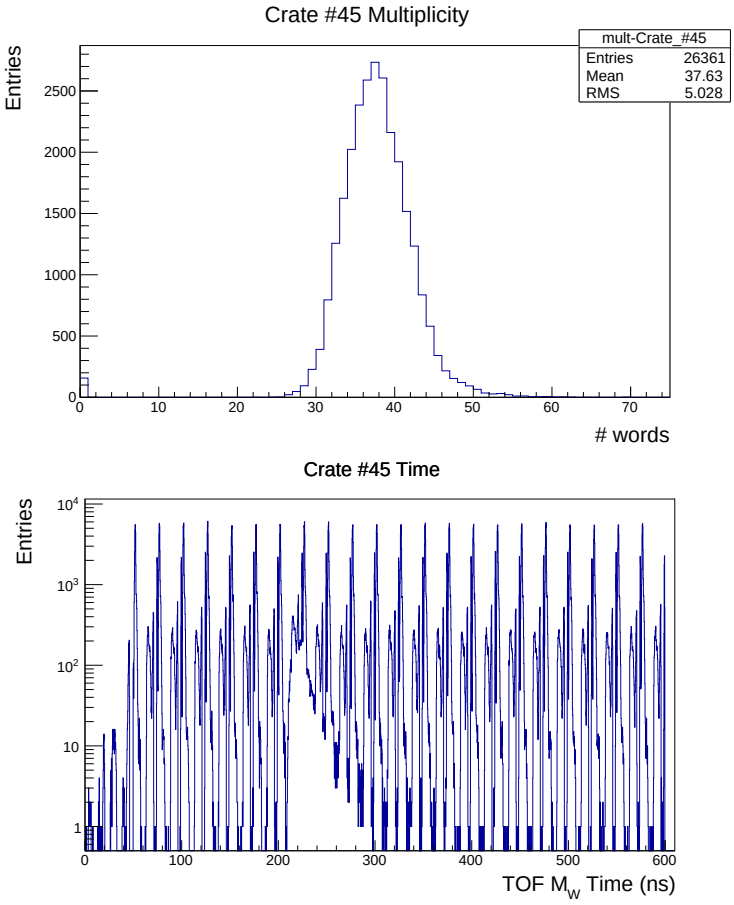

Figure 3.22: *Details on the crate* #45 *in the LHC12d run.*

crate includes 12 slots, numbered from 1 to 12. The slot #1 of each crate contains the Data Read-out Module (DRM), and the #2 the Local Trigger Module (LTM). There is a Clock and Pulser Distribution Module (CPDM) for each side of each supermodule, that corresponds to one crate on two. Therefore, the slot #3 of all the right (i.e. odd numbered) crates contains a CPDM, while the same slot on left crates contains the its first TRM. For convenience, in each crate such TRM is labelled as $Trm\_\#3$. All the other slots in all the crates contain TRMs, numbered from #4 to #12. Therefore, there are 10 TRMs in each crate left and 9 TRMs in each crate right, and as a result, 19 TRMs for each side of each supermodule. The whole number of the slots in the crate considered for the study on TRMs is therefore 720, but only 684 of them actually contain a TRM card. In addition, the

installation of the PHOS detector in ALICE imply the non installation of TOF central modules in three supermodules (to avoid absorption of photons pointing to the PHOS). Correspondingly, the TRM_#12 is not installed in 6 supermodules (i.e. in crates from #52 to #63), moving the number of effective TRMs to 672.

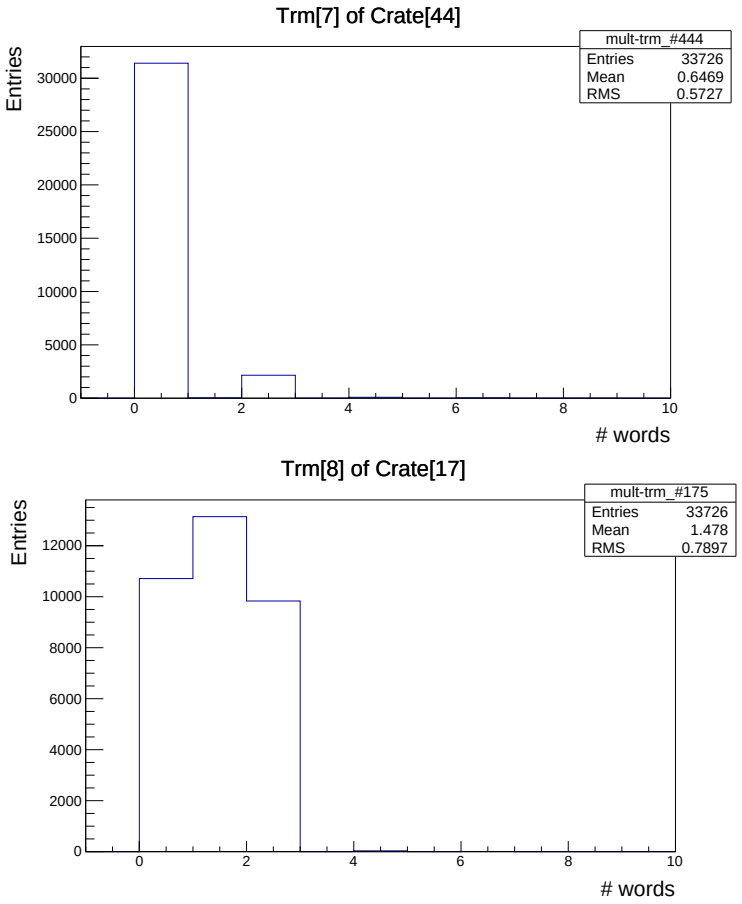

Figure 3.23: *Comparison between multiplicity of two TRMs from a LHC10d run. The signal of the TRM* #175 *is clearly affected by noise.*

Figure 3.23 shows the difference in the word multiplicity collected from two TRMs in the LHC10d run. In the bottom part of the figure it is reported the response from a TRM affected by noise. Noise signals are evident on the entries for a single word, which indicates the presence of many "orphanes" signals (a leading edge word without the corresponding trailing or viceversa). After the filtering, the shape of the distribution of such TRMs

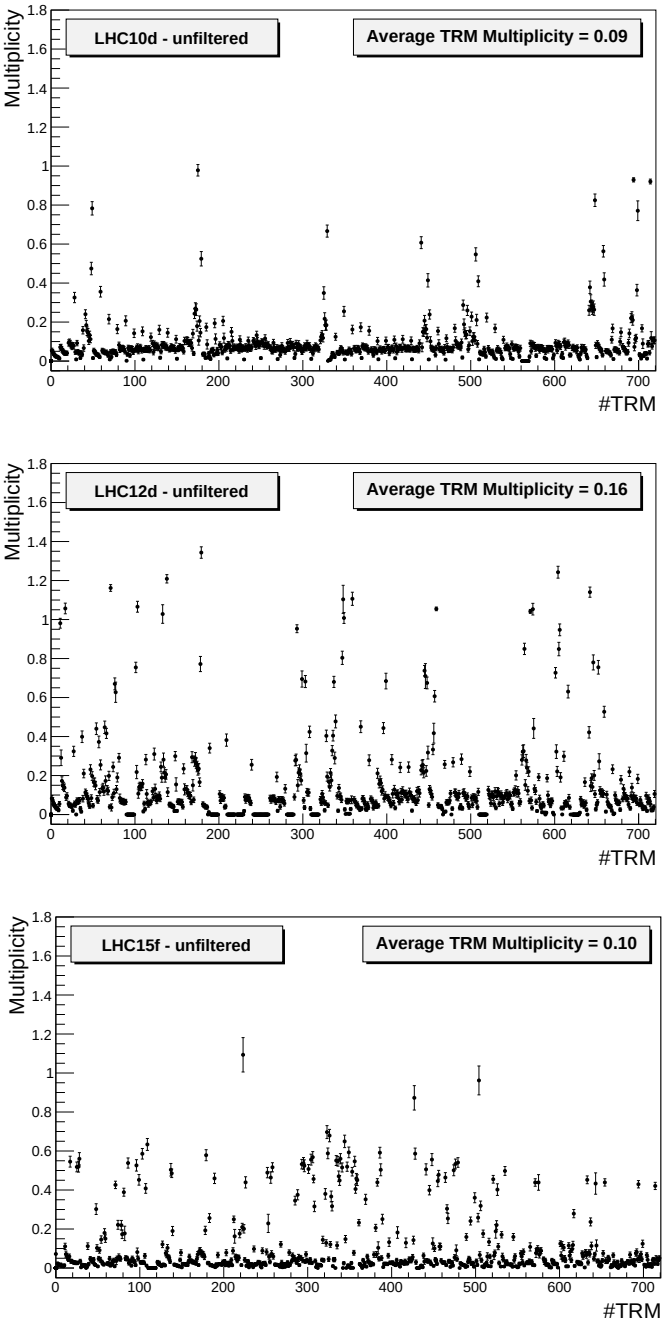

Figure 3.24: *Average multiplicity for all the active TRMs in all the three run periods considered without noise subtraction.*

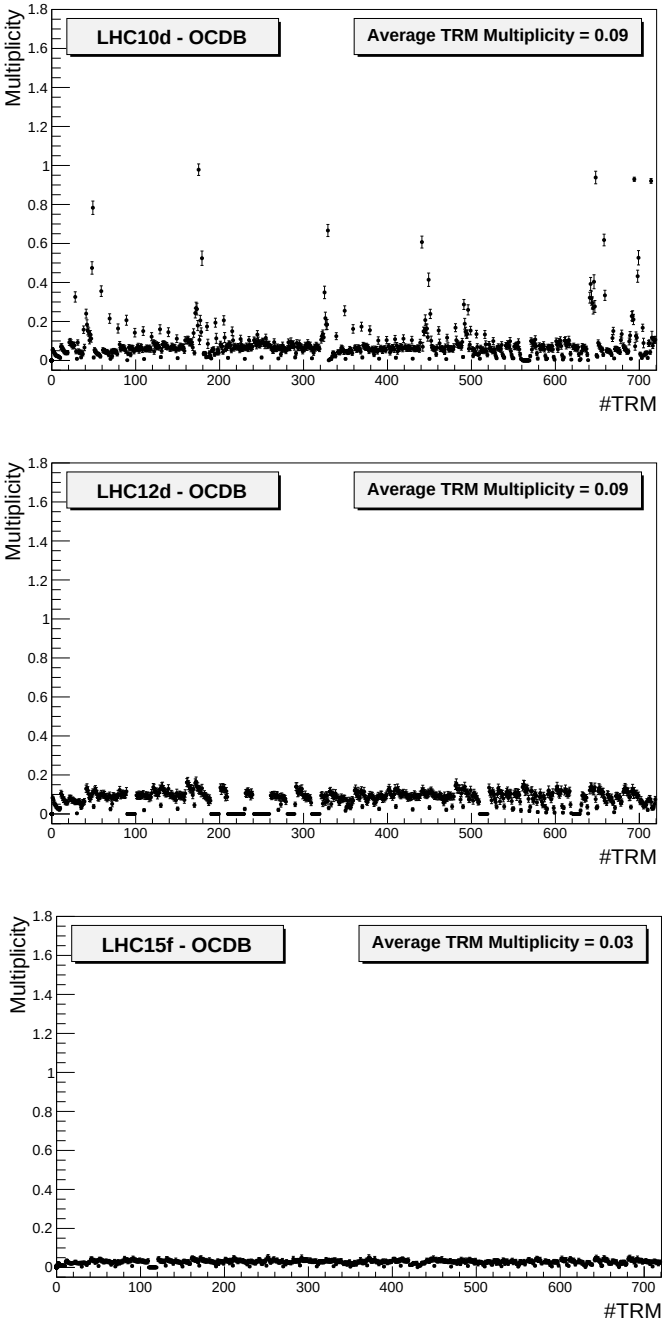

Figure 3.25: *Noise subtracted average multiplicity for all the active TRMs in all the three run periods considered.*

should approach a regular one, like that showed for the TRM #444. The different efficiencies in filtering already highlighted in the study for the crate are reflected in the study for the TRMs. Figures 3.24 and 3.25 show the multiplicity for all the active TRMs in the three run periods considered. Again, the error bar are obtained from standard errors. The numbering of TRMs is defined as `TRM_Id = 10*crate_Id + slotNumber - 3`. So, for example, the TRM in the slot #3 of crate 65 is labelled as 650.

Points corresponding to non existent TRMs (due to CPDM) or non installed ones (due to PHOS) are not reported, nor taken into account for calulations and further considerations. It can be seen from the figures that the assumption on the average values holds also for TRMs. However, this time it may happen that some TRMs take values considerably higher (also 10 or 15 times) than the average. This will be taken into account in further studies.

An important question, at this point, is if in the framework of continuous read-out at the energies expected from the LHC Run 3, the read-out system of the TOF could correctly read out the data coming from the MRPCs given the observed multiplicities in real data. Furthermore, it has to be considered what happens if some or *all* the TRMs or the crates take a multiplicity higher than the average of a factor like those found above.

3.3.3 Simulation of the C-R/O

The key part of the study on the proposed continuous read-out scheme is represented by the actual simulation of different matching windows in the framework of a continuous readout for the TOF detector. The macro was written to perform the simulation by considering as inputs:

- the TOF multiplicity distribution,
- the hit time distribution,

both for background and interaction windows from the output file of the macro described in Sec. 3.3. Other inputs to the macro are the parameters that follow:

- the matching window length M_W, defined as the inverse of the asynchronous trigger rate considered in the simulation, according to the Eq. (3.2),

- the interaction rate expected inside the detector,
- the number N of simulation windows to generate.

The basic idea of the simulation consists in sampling the background multiplicity from an input file and distributing the hits simulated to happen at a specific moment of the matching window. The background hits will be uniformly distributed in the simulated matching window. Then, the interaction multiplicity for each interaction is sampled and the background subtracted in order to avoid double hit countings. This is because the interaction window distribution, as obtained, includes both the contributions from the interaction and from the background.

According to preliminary considerations made in Sec. 3.2.1, the duration of interaction and background windows are fixed to 200 ns, consistently with the analysis done. Dividing the required duration of the simulated window, passed as input, by the duration of the background windows, the simulated window is divided in n background winodws. For a typical duration of 10 μs, the simulation window will have 50 divisions.

A number N of simulation windows is generated and analyzed in a loop. At the beginning of each iteration, the number of interactions and the number of the hits generated inside the previous simulation window are set to zero. Each iteration in the loop embraces two fundamental operations i.e. create the background and generate the interactions.

- **Background**
  At this step, the k^{th} simulation window (with $k = 1 \div N$) has been partitioned into a number of background divisions. The background is sampled from the background window in the input file, via the `GetRandom` library, but sampled hits have to be assigned to a particular division. This is made in another loop, from zero to the number of divisions, by sampling the time distribution from the input file and using a variable that takes into account the position in the simulation window. Background hits in background windows are typically few and it is possible that different divisions have no background hits. Anyway, at this point, there are $n_{hit}^{bkg}[k]$ hits and still no interaction ones, in the k^{th} simulation window of the loop.
- **Interactions**
  Interaction events are generated by sampling from the interaction win-

dow of the input file via the `GetRandom` library. The timing is generated by considering that for events happening with a constant rate, the frequency between subsequent events is given by the *exponential distribution of outcomes*, that can be simulated by computing the following relation

$$f \sim \left(\frac{1}{t_{evt}[i]}\right) log[\xi], \tag{3.16}$$

where the term $\frac{1}{t_{evt}[i]}$ is the rate of the considered events and ξ indicates the output of a random uniform function [88]. The time position for the i^{th} interaction event is

$$d_i = \sum_i \left[\left(\frac{t_{evt}[i]}{25}\right) \cdot 25\right] \; ns, \tag{3.17}$$

where i indicates the events 'collected' (simulated) so far in the simulation window. Rounding the time positioning of events like in the Eq. (3.17), (the variable which indicates the $t_{evt}[i]$ term has to be defined as an `integer`) one considers that the events can occur only at times which are multiple of 25 ns since collisions happen in sync with the rising edge of the LHC clock. This is in accordance with the LHC machine clock and with the structure of the bunches inside the collider. When d overcomes the duration length of the simulation window, the interaction cycle occurs in a `break` instruction and the analysis of all the collected hits in the simulation windows starts. Otherwise the macro goes on reading further statements in the loop and the interaction multiplicity corresponding to the time position earlier defined is sampled from the input file. This number indicates the total number of hits at that time, which also comprehends the background. To avoid double countings, background multiplicity is sampled again and then subtracted from the interaction multiplicity. Hence, for each of the i interaction events collected in the simulation window, a number $n_{hit}^{evt=i}$ of corresponding hits, depending on the subtracted multiplicity, is generated by sampling $n_{hit}^{evt=i}$ times from the multiplicity interaction distribution.

Finally, for the k^{th} of the N simulation windows generated, the total hit number will be

$$n_{hit}^{tot}[k] = n_{hit}^{bkg}[k] + \sum_i n_{hit}^{evt=i}[k]. \tag{3.18}$$

The macro finally stores the histograms generated. For each iteraction, the number of the interactions and the total number of hits generated in the k^{th} simulation window are stored in two histograms. At the end of all the iterations, the histograms will have N entries and they will give the average number of interactions and the average number of hits per simulated matching window. In the whole procedure the sampling is made from the total TOF multiplicity, the crate multiplicity and the TRM multiplicity, filling the corresponding simulated distributions. In addition, other histograms are created to control signals generated, i.e. for the background, for the interaction and for the generation of subsequent events.

The results that will be presented in this work are obtained from simulations performed by keeping 100,000 interaction windows and by considering the worst case possible inside the detector, i.e. by fixing 1 MHz of interaction rate. Simulations with lower interaction rates would be obviously more favourable with respect to the occupancy (and corresponding needed bandwidth) to be evaluated. I have therefore tested first the more challenging case, that is the 1 MHz interaction rate.

The plots in Figure 3.26 show a matching window produced as a result of the simulation. It can be seen how the time positions of interaction and background signals are randomly distributed along the entire matching window, instead than in the case of triggered read-out, in which signals from interactions were enclosed in the time window between 200 ns and 400 ns from the opening of the window.

For the standard 100 kHz of asynchronous trigger rate (corresponding to a 10 μs matching window) taken as example up to now, there are 10 interactions expected per matching window. The result of the simulation is in agreement with this prediction, as shown in Figure 3.27, demonstrating the correctness of the sampling procedure. Figure 3.28 shows the whole simulated TOF multiplicity for the same situation considered.

The crate multiplicity and the TRM multiplicity resulted from the simulation are showed in Figures 3.29 and 3.30. The distributions found for the interaction windows reflect the behaviour for crate and TRM data collection with low noise signals, while for the backgrounds they are almost undefined, as expected.

These results were obtained by sampling from the distributions for the interaction and the background windows in the input file and correspond

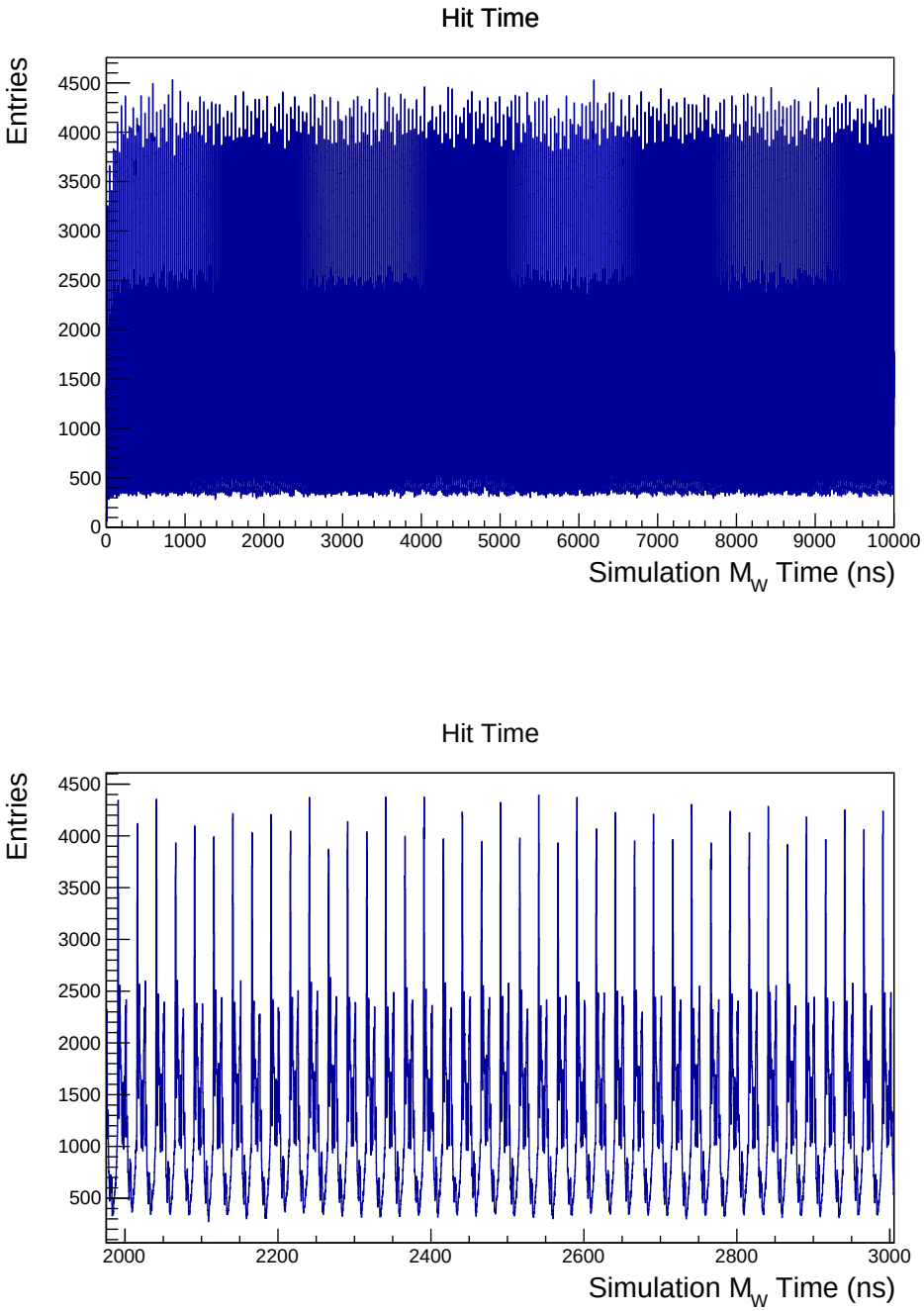

Figure 3.26: *On the top: the time window generated. On the bottom: a detail of the time window distribution*

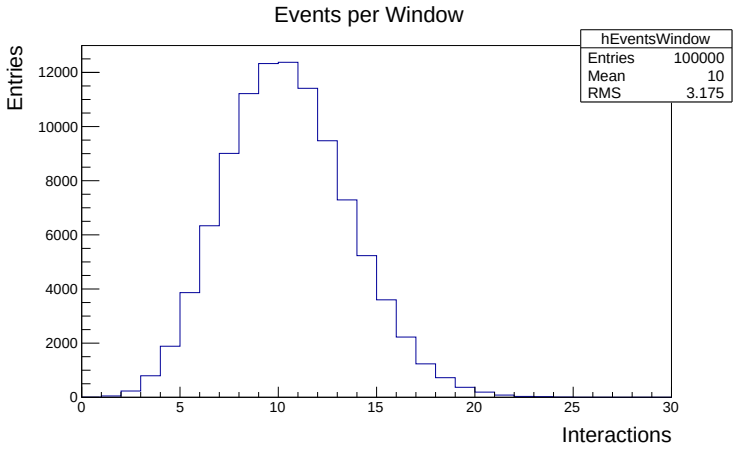

Figure 3.27: *The average number of events generated in the simulation windows for an asynchronous trigger rate of* 100 kHz *with input.*

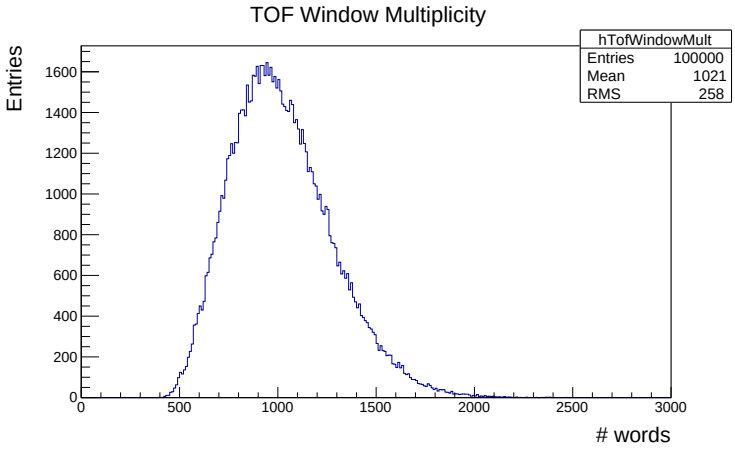

Figure 3.28: *The TOF window multiplicity simulated for an asynchronous trigger rate of* 100 kHz *with input based on a LHC10d run (no noise filtered).*

to the real response of the all the crates and of all the TRMs. In this way the simulation does not take into account the various issues on single components in the runs considered for the sampling but it looks to the *average* behaviour of single crates and single TRMs, i.e. the assumption on the average. This allows a more realistic simulation, unrelated to single noisy crates or casual malfunctioning found, making possible to give a reliable indication for the implementation on the continuous read-out for the TOF detector. As it was demonstrated in previous sections, the assumption on

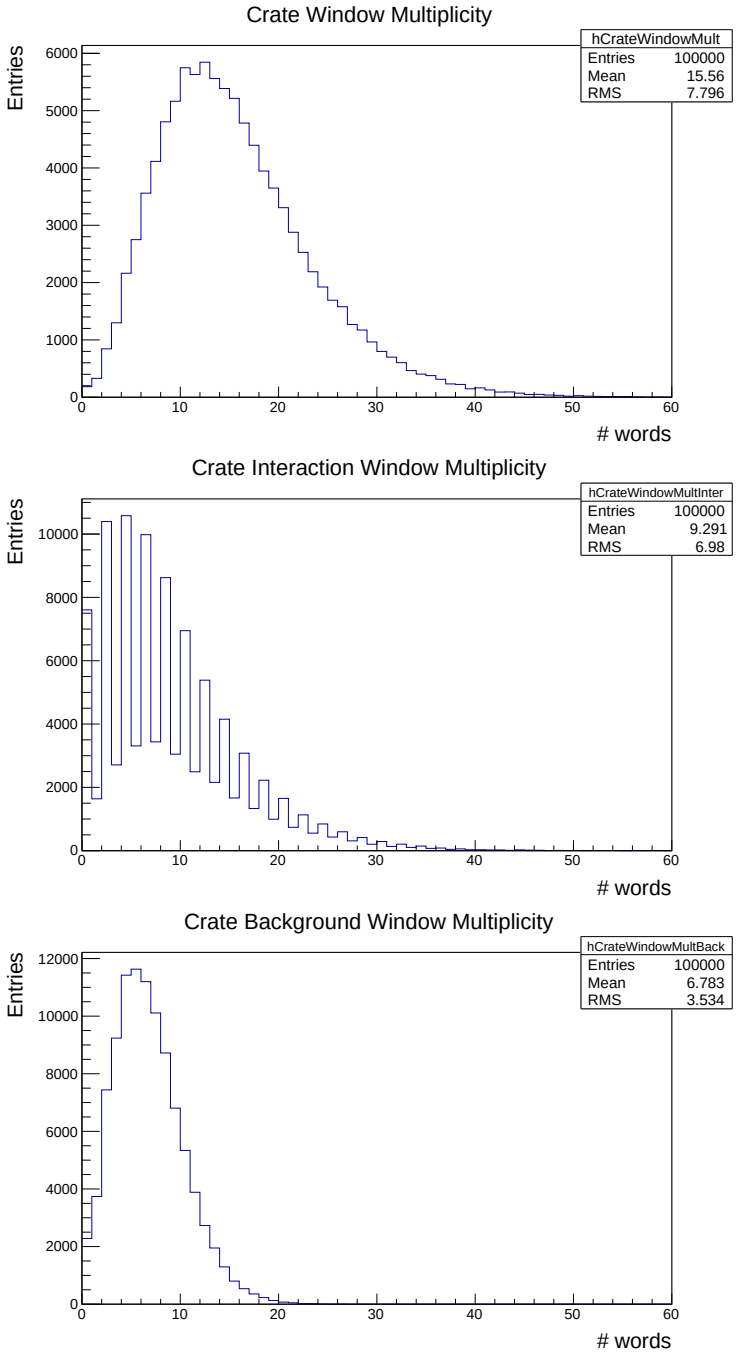

Figure 3.29: *Crate multiplicity for the simulated matching window from LHC10d data. Interaction and background windows are also showed.*

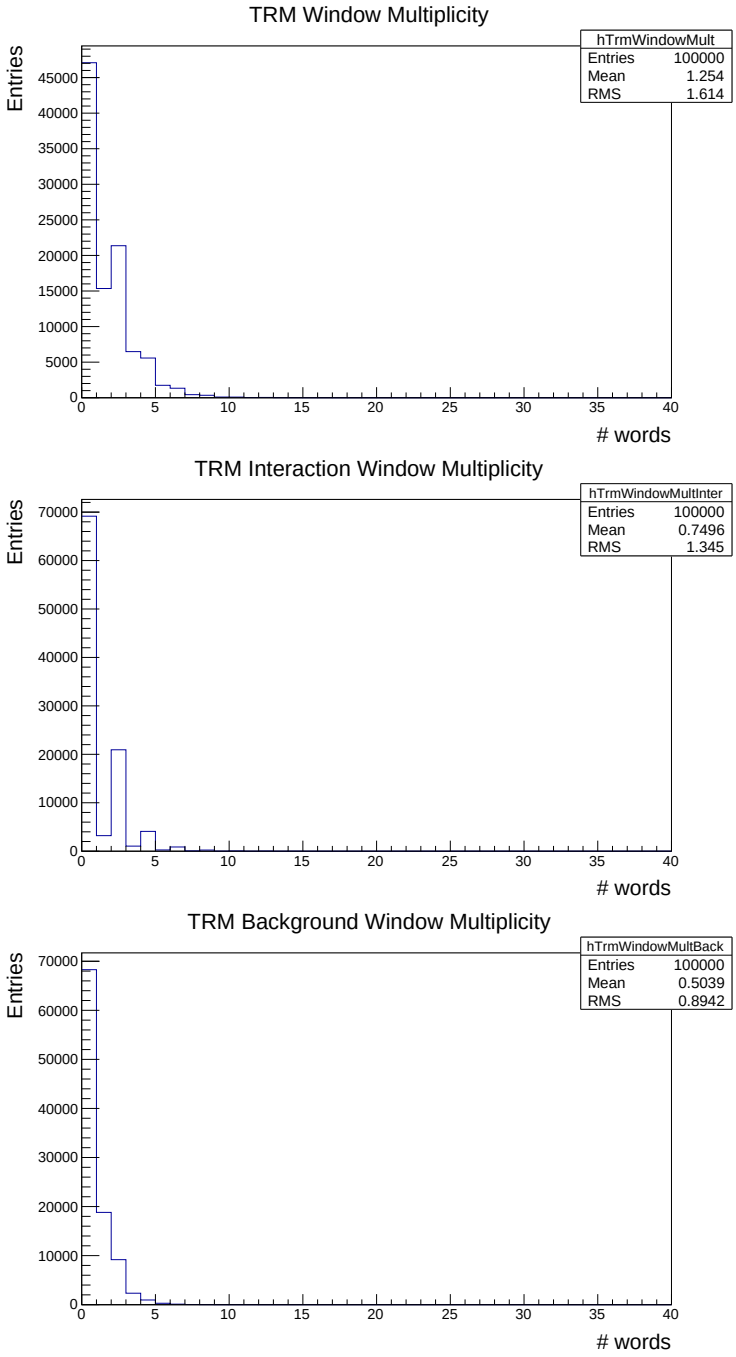

Figure 3.30: *The multiplicity for the TRMs in the simulated matching window from the LHC10d data considered so far. Interaction and background windows are also showed.*

average values is acceptable and it is correct to consider the sampling from general distributions, provided that the potential criticalities fall within the safe zones or that an online system of to quickly turn off excessively noisy channels is implemented.

Result showed so far were obtained from data from a single run and for a single asynchronous trigger frequency given as a input. The simulation was performed for all the runs considered and for several matching windows durations inside the range of frequencies found in Sec. 3.2.

3.4 Results

First results from a single run and for a single matching window duration were introduced in Sec. 3.3.3. In this section, I present the result of the simulation for different rates of asynchronous trigger by considering as input data from three different *pp* runs.

The simulations were performed for different matching window durations, from $M_W = 4\ \mu s$ to $M_W = 44\ \mu s$, which corresponds to asynchronous trigger rates from 250 kHz to 22.73 kHz, respectively. Results reported in Figures 3.31 and 3.32 are obtained by considering an interaction rate in *pp* collision of 1 MHz, as initially foreseen for the LHC Run 3 and in order to test the most unfavorable conditions.

The results are organized in the six plots reported in the following and they are compared with corresponding *bandwidth safe zone*. Safe zones for crate bandwidth and for TRM bandwidth are obtained from Eqs. (3.4) and (3.5), respectively and they are represented as the shaded regions in the figures.

Red and blue curves indicate the results of the simulations based on OCDB filtered and without noise suppression, respectively. All the simulations show good behaviours, both for crate and for TRM bandwidths. All the values obtained for the different trigger frequencies and for the three run periods are contained within the bandwidth safe zones. Results from LHC10d data reflect the uneffective noise detection and as a consequence the two lines, both for crate and TRM bandwidths are almost superimposed. In 2012 the data filtering improved and results from the simulations show correspondingly a difference between the two simulated situations. Simulation results to take in major account are probably those coming from LHC15f data, since they can give a better anticipation of the Run 3. In fact, in 2015

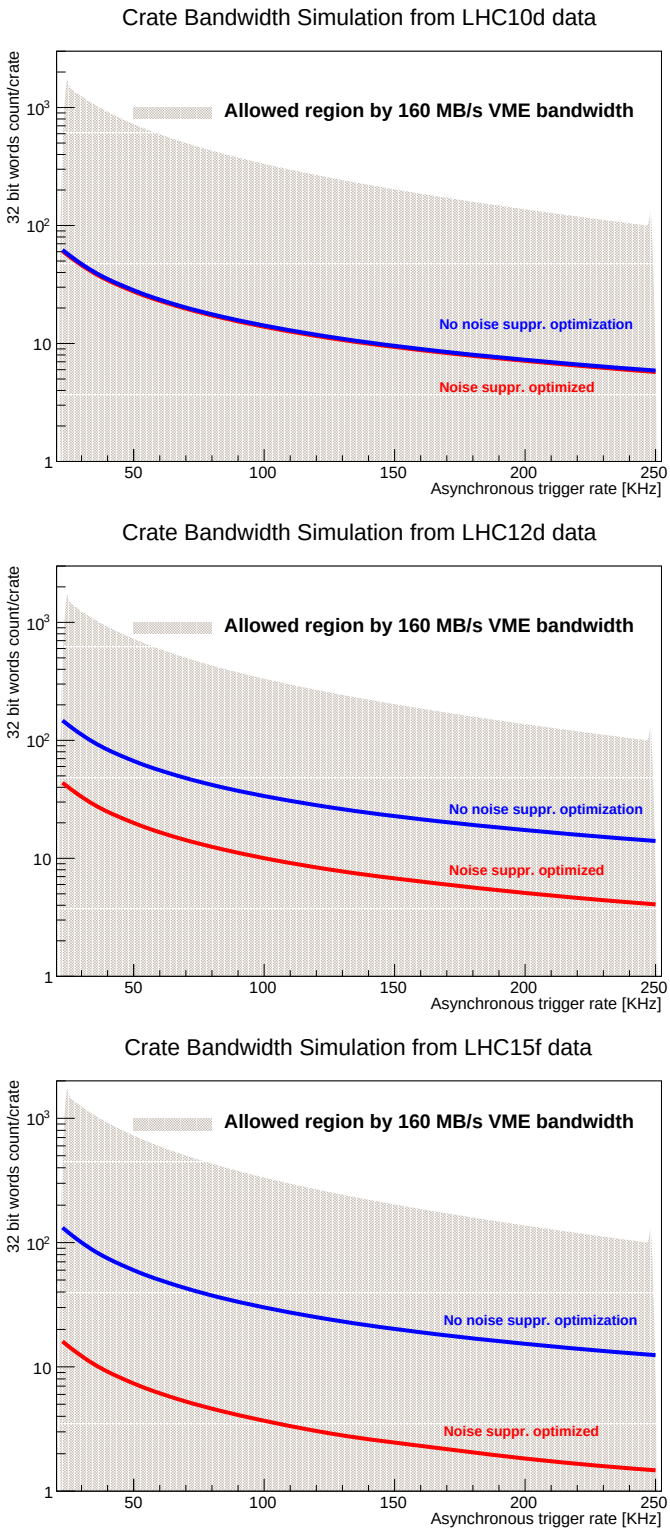

Figure 3.31: *Results of the simulations for the crate multiplicity form the three run periods considered. It is possible to compare the results (red and blue lines) with allowed bandwidth zones, represented by the shaded regions.*

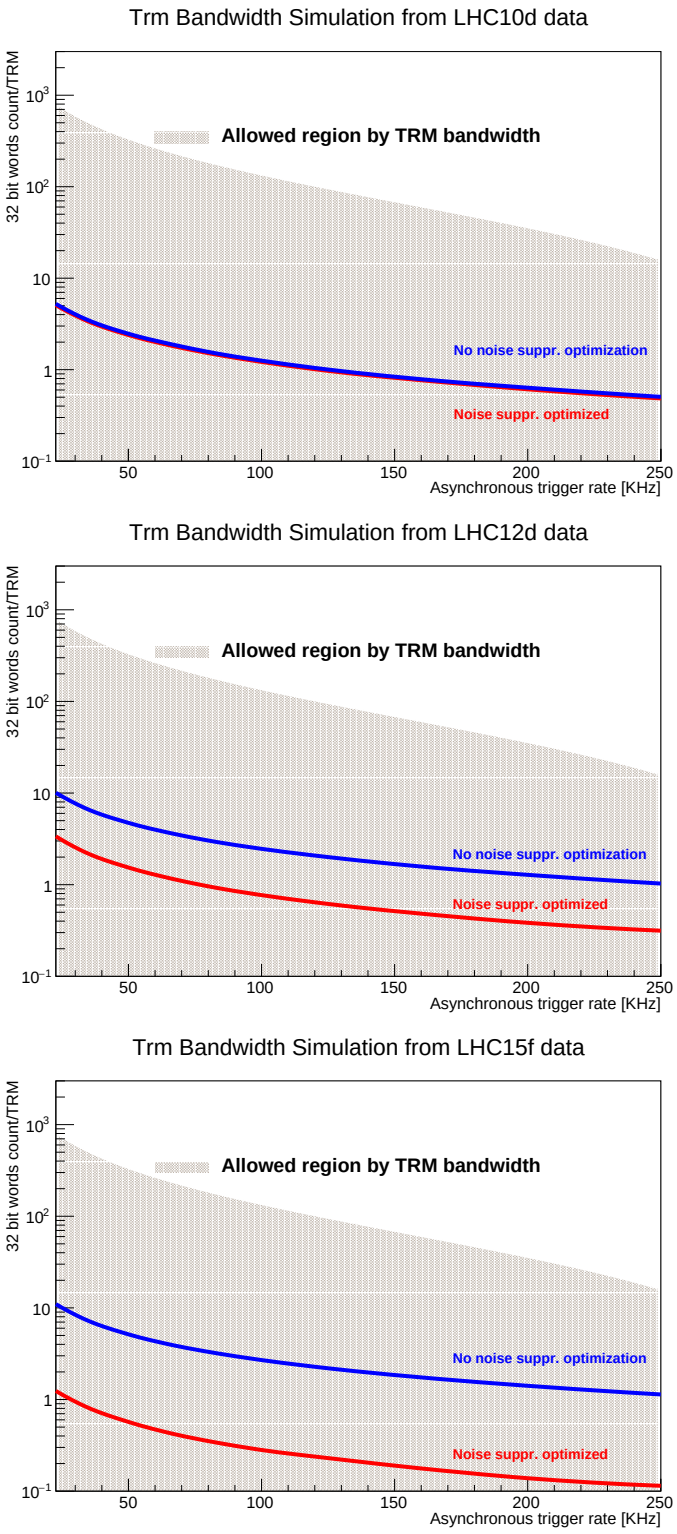

Figure 3.32: *Results of the simulations for the TRM multiplicity form the three run periods considered. TRM bandwidth safe zones are also reported and indicated as the shades regions.*

the protons collide at $\sqrt{s} = 13\ TeV$ and the enhancement of multiplicity due to the increase of the centre-of-mass energy to $\sqrt{s} = 14\ TeV$ is quite negligible, as inferred in Sec. 3.2.3.

At this step it is important to remember that the results obtained from the simulation come from the assumption on the average. The results from tha analyses of single crates and of single TRMs (Secs. 3.3.1 and 3.3.2), showed that it is possible that the multiplicity take unexpected values for some crates or some TRMs. Such values were estimated as four or five times larger than the average, for the crates, and even ten or fifteen times larger than the average for TRMs. If one considers as the worst case possible the situation in which *all* the crates or all the TRMs in a run take such values, the lines in Figures 3.31 and 3.32 should be shifted upward to values five times higher for crates and fifteen times higher for TRMs. Although this seems strongly unlikely, it can be observed from figures that in such situation unfiltered data would be still within the allowed zone, both for crates and TRMs and for all the three periods considered. It is any case advisable if a system of *online* detection of noisy channel would be implemented. Such a system should detect the noisy channels *in real time* and then acting on the electronics configuration to turn them off, lowering the multiplicity to the levels of OCDB filtered data.

In a more realistic case, it can happen sometimes that some single TRM (and the corresponding crate) would take an unexpected high values. As it was remarked, the HPTDCs are free running. This means that each module stores in its buffer data from MRPCs. and no hits are lost even if the readout, occasionally, might take more than the duration of a matching window to complete in a single event. The problem with the noise arises if such delay becomes systematic and the read-out can no cope with the whole amount of data (that is internal buffers are saturated).

I previously mentioned that the ALICE Collaboration could choose to run *pp* collision at interaction rates of 500 kHz. Figure 3.33 shows the results of the simulation from LHC15f data at such interaction rate. At the present this seems the most likely situation for LHC Run 3 due to limitations in the ITS read-out. It can be observed in the figure that the multiplicity levels are obviously lower with respect to the simulation made at 1 MHz of interaction rate.

Based on the studies and results reported in this chapter, the proposed

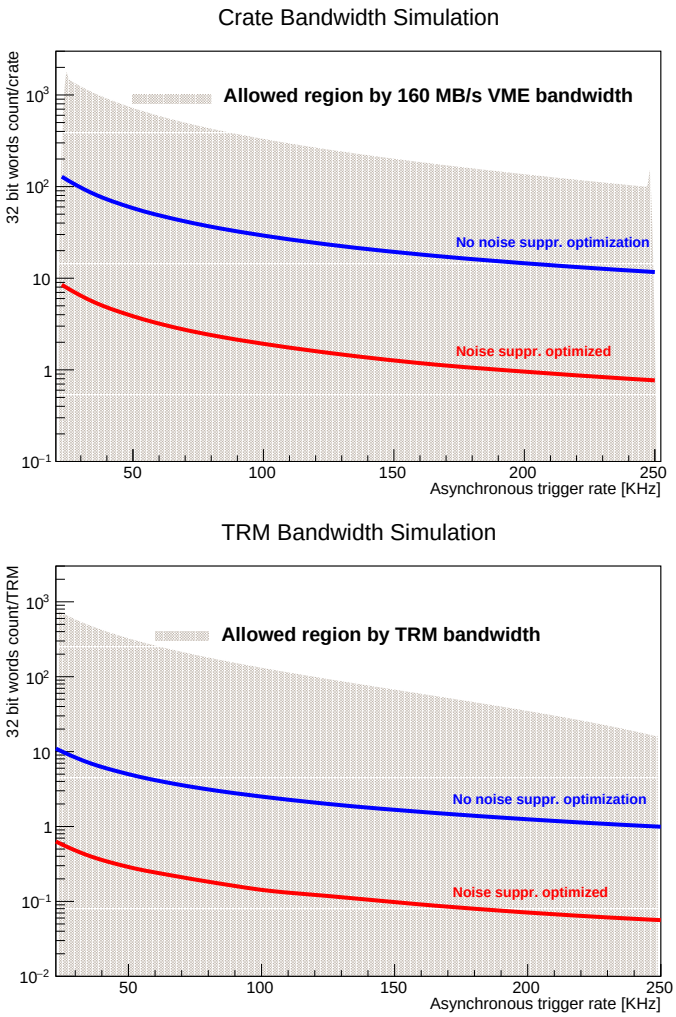

Figure 3.33: *Simulation performed at* $500\ kHz$ *of interaction rate from LHC15f data. At the present, this seems the most likely perspective for the LHC Run 3. It is worty to note that the scale on the y axis differs from other figures in this section.*

continuous read-out scheme seems a viable option for the ALICE-TOF detector during the LHC Runs 3 and 4.

Conclusions

The Master's Degree thesis work that I present was carried out under the upgrade programme of the ALICE experiment, in order to fully exploit the scientific potential of the LHC for fundamental studies of QCD.

I discussed the physics of relativistic heavy-ion collisions by focusing on the QCD and on the characterization of the quark-gluon plasma. To do this, some attention was paid on the search of the QGP observables and on results obtained so far. I also described the ALICE experiment, with a focus on the TOF detector. Furthermore, I discussed the ALICE upgrade programme and its main physics goals.

As a part of the ALICE upgrade programme I studied if it is possible to implement a data read-out for the TOF detector which allows to register hits at the interaction rate of 1 MHz foreseen for pp interactions after the 2018, by using the electronics currently available. To check such proposal I analyzed data from LHC data taking at three different energies and luminosities and I studied the occupancy experimentally observed. By studying the characteristics of the electronics of the detector, I identified a method of data acquisition which *de facto* implements a continuous read-out also for the TOF detector within the framework of the ALICE experiment.

To validate the proposal, I studied first how the presence of noisy channels impacts on hit multiplicity. Currently this is not critical, especially because the read-out is triggered and a small matching window (just 600 ns) is used. This keeps the amount of recorded hits from noisy channels to a low level. In such case, in fact, the incidence of channels affected by noise is very low, due to the design of the HPTDCs and the matching window used. In the framework of a continuous read-out, instead, channels presenting a great amount of noisy signals can overcome the TRM and crate bandwidths, since it must hold the relation

$$f \cdot M_W = 1$$

described in the chapter 3.

I also evidenced how it would be therefore better to implement also an online system to detect and turn off excessively noisy channels during the data taking.

In the Operational Run 3 a centre of mass energy of $\sqrt{s} = 14\ TeV$ is foreseen for pp collisions. Data available at the present for the simulation comes form $\sqrt{s} = 7\ TeV$ to $\sqrt{s} = 13\ TeV$. Therefore, I perfomed a study on the scaling of the detected multiplicity with the increasing of the centre-of-mass energy based on theoretical considerations and data observations collected so far. As a result, I found that no significant effects are expected in the increasing of the multiplicity due to the increasing of the energy.

All the studies performed and discussed in this thesis confirm that the proposed continuous read-out scheme is a viable option for the ALICE-TOF detector during Run 3 and Run 4.

Bibliography

[1] E. V. Shuryak. *Physics of strongly coupled Quark-Gluon Plasma.* Prog. Part. Nucl. Phys., **62**: 48-101, (2009).

[2] U. Heinz, M. Jacob. *An Assessment of the Results form the CERN Lead Beam Programme.* (2000). [arXiv:nucl-th/0002042v1].

[3] J. Letessier, J. Rafelski. *Hadrons and Quark–Gluon Plasma.* Cambridge monographs on Particle Physics, nuclear Physics and Cosmology, (2002).

[4] M. Herrero. *The Standard Model.* (1998). [arXiv:hep-ph/9812242].

[5] C. Quigg. *Gauge Theories of the Strong, Weak and Electromagnetic Interactions.* Addison–Wesley Publishing Company, (1997).

[6] F. Halzen, D.H. Martin. *Quarks and Leptons: an Introductory Course in Modern Particle Physics.* John Wiley & Sons, (1984).

[7] G. M. Garcìa. *Advances in Quark Gluon Plasma.* (2013). [arXiv:nucl-ex/1304.1452v1].

[8] W. Greiner, S. Scram, E. Stein. *Quantum Chromodynamics - Second Edition.* Springer, (2002).

[9] R. S. Bhalerao. *Relativistic Heavy–Ion Collisions.* (2014). [arXiv:nucl-th/1404.3294v1].

[10] Z. Fodor, S. D. Katz. *Critical point of QCD at finite T and μ, lattice results for physical quark masses.* JHEP, 0404, (2004).

[11] F. Karsch. *Lattice Results on QCD Thermodymamics.* (2001). [arXiv:hep-ph/0103314v1].

[12] S. Ejiri, *et al. Study of QCD thermodynamics at finite density by Taylor expansion.* Prog. Theor. Phys. Suppl., 153, (2004).

[13] A. Bazavov, *et al. Nonperturbative QCD simulations with 2+1 flavors of improved staggered quarks.* Review of Modern Physics, **82** (2), (2010).

[14] D. J. E. Callaway, A. Rahman. *Microcanonical Ensemble Formulation of Lattice Gauge Theory.* Phys. Rev. Lett., **49** (9), (1982).

[15] D. J. E. Callaway, A. Rahman. *Lattice gauge theory in the microcanonical ensemble.* Phys. Rev. D, **28** (6), (1983).

[16] P. Petreczky. *Lattice QCD at non-zero temperature.* Journal of Physics G, **39**, (9) 093002, (2012).

[17] F. Karsch, E. Laermann and A. Peikert. *Quark Mass and Flavour Dependence of the QCD Phase Transition.* (2001). [arXiv:hep-lat/0012023].

[18] E. V. Shuryak. *Two Scales and Phase Transitions in Quantum Chromodynamics.* Phys. Lett. B, **107**, (1981).

[19] P. Petreczky, *et al. Static quark-antiquark free energy and the running coupling at finite temperature.* (2008). [arXiv:hep-lat/0406036v1].

[20] R. Gupta. *Introduction to Lattice QCD.* (1998). [arXiv:hep-lat/9807028v1].

[21] L. McLerran. *The Color Glass Condensate and Small x Physics: 4 Lectures.* (2001). [arXiv:hep-ph/0104285v2].

[22] H. Weigert. *Evolution at small x_{bj}: The Small Color Glass Condensate.* (2005). [arXiv:hep-ph/0501087].

[23] K.J. Eskola, K. Kajantie, P.V. Ruuskanene and K. Tuominen. *Scaling of transverse energies and multiplicities with atomic number and energy in ultrarelativistic nuclear collisions.* Nucl. Phys. B, **570**, (2000). [arXiv:hep-ph/9909456].

[24] The ALICE Collaboration. *Centrality determination of Pb-Pb collisions at $\sqrt{S_{NN}}$ = 2.76 TeV with ALICE.* (2014). [arXiv:hep-ex/13014361].

[25] K. Yagi, T. Hatsuda, Y. Miake. *Quark–Gluon Plasma - From Big Bang to Little Bang.* Cambridge University Press, (2005).

[26] R. J. Fries and B. Müller. *Heavy ions at LHC: Theorethical issues.* *Eur. Phys. J.*, C **34**, (2004). [arXiv:nucl-th/0307043].

[27] A. Andronic. *An overview of the experimental study of quark-gluon matter in high-energy nucleus-nucleus collisions.* (2014). [arXiv:nucl-ex/1407.5003].

[28] The ALICE Collaboration. *Charged-particle multiplicity measurement in proton-proton collisions at* $\sqrt{S_{NN}} = 7\ TeV$ *with ALICE at LHC.* (2010). [arXiv:hep-ex/1004.3514].

[29] The ALICE Collaboration. *Charged-particle multiplicity density at mid-rapidity in central Pb-Pb collisions at* $\sqrt{S_{NN}} = 2.76\ TeV$. (2011). [arXiv:nucl-ex/1011.3916].

[30] The ALICE Collaboration. *Centrality dependence of the charged particle multiplicity density at mid-rapidity in central Pb-Pb collisions at* $\sqrt{S_{NN}} = 2.76\ TeV$. (2011). [arXiv:nucl-ex/1012.1657].

[31] J.D. Bjorken. *Highly relativistic nucleus-nucleus collisions: The central rapidity region.* *Phis. Rev. D*, Vol. **27**, No. 1, (1983) 140-150.

[32] The CMS Collaboration. *Measurement of the pseudorapidity and centrality dependence of the transverse energy density in PbPb collisions at* $\sqrt{S_{NN}} = 2.76\ TeV$. (2012). [arXiv:nucl-ex/1205.2488].

[33] A. Toia for the ALICE Collaboration. *Bulk properties of Pb-Pb collisions at* $\sqrt{S_{NN}} = 2.76\ TeV$ *measured by ALICE.* (2011). [arXiv:nucl-ex/1107.1973].

[34] The STAR Collaboration. *Systematic measurements of identified particle spectra in pp, d+Au, and Au+Au collisions at the STAR detector.* (2009). [arXiv:nucl-ex/0808.2041].

[35] U. Heinz. *Concepts of Heavy-Ion Physics.* (2000). [arXiv:hep-ph/0407360].

[36] L. Milano (for The ALICE Collaboration). *Identified charged hadron production in Pb-Pb collisions at the LHC with the ALICE Experiment.* (2013). [arXiv:hep-ex/1302.6624].

[37] The STAR Collaboration. *Experimental and Theoretical Challenges in the Search for the Quark Gluon Plasma: The STAR Collaboration's Critical Assessment of the Evidence from RHIC Collisions.* (2005). [arXiv:nucl-ex/0501.1009v3].

[38] P. Braun-Munzinger, *et al. Paticle production in Heavy-Ion collisions.* (2003). [arXiv:nucl-th/0304013].

[39] A. Andronic, *et al. The thermal model on the verge of the ultimate test: particle production in Pb-Pb collisions at the LHC. J. Phys. G*, **38** 124081, (2011). [arXiv:nucl-th/1106.6321].

[40] The ALICE Collaboration. *Pion, Kaon, and Proton Production in Central Pb-Pb Collisions at* $\sqrt{S_{NN}} = 2.76\ TeV$. (2012). [arXiv:nucl-th/1208.1974].

[41] E. Schnedermann, J. Sollfrank, and U. Heinz. *Thermal Phenomenology of hadrons from 200A GeV S+S collisions. Phys. Rev. C*, **48** 2462, (1993).

[42] B. Bartke. *Relativistic Heavy Ion Physics.* World Scientific, (2009).

[43] S. Voloshin and Y. Zhang. *Flow study in relativistic nuclear collisions by Fourier expansion of Azimuthal particle distributions. Z. Phys. C*, **70** 665-672, (1996). [arXiv:hep-ph/9407282].

[44] The ALICE Collaboration. *Elliptic flow of charged particles in Pb-Pb collisions at* $\sqrt{S_{NN}} = 2.76\ TeV$. (2011). [arXiv:nucl-ex/1011.3914v2].

[45] Y. Kharlov, for the ALICE Collaboration. *Recent results from ALICE.* (2012). [arXiv:nucl-ex/1203.2420v1].

[46] The ALICE Collaboration. *Elliptic flow of identified hadrons in Pb-Pb collisions at* $\sqrt{S_{NN}} = 2.76\ TeV$. (2014). [arXiv:nucl-ex/1405.4632v2].

[47] F. Noferini (for the ALICE Collaboration). *Anisotropic flow of identified particles in Pb-Pb collisions at* $\sqrt{S_{NN}} = 2.76\ TeV$ *measured with ALICE at the LHC.* (2012). [arXiv:nucl-ex/1212.1292v1].

[48] J. Rafelski, B. Muller. . *Phys. Rev. Lett.*, **48**, 1066, (1982).

[49] The ALICE Collaboration. *Multi-strange baryon production at mid-rapidity in Pb-Pb Collisions at* $\sqrt{S_{NN}} = 2.76\ TeV$. (2013). [arXiv:nucl-ex/1307.5543].

[50] A. Adare, for the PHENIX Collaboration. *Enhanced production of direct photons in Au-Au collisions at* $\sqrt{s_{NN}} = 200\ GeV$ *and implications for the initial temperature.* (2008). [arXiv:nucl-ex/0804.4168].

[51] M. Wilde for the ALICE Collaboration. *Direct photon in pp and Pb-Pb Collisions at with ALICE.* (2012). [arXiv:nucl-ex/1412.7902].

[52] The ALICE Collaboration. *Suppression of Charged Particle Production at Large Transverse Momentum in Central Pb-Pb Collisions at* $\sqrt{S_{NN}} = 2.76\ TeV$. (2010). [arXiv:nucl-ex/1012.1004].

[53] The ALICE Collaboration. *Transverse momentum dependence of inclusive primary charged-particle production in p-Pb collisions at* $\sqrt{S_{NN}} = 5.02\ TeV$. (2015). [arXiv:nucl-ex/1405.2737].

[54] X.N. Wang, *et al. Concepts of Heavy-Ion Physics.* Phys. Rev. D, **51**, 3436, (1995).

[55] The ALICE Collaboration. *Measurements of jet suppression in central Pb-Pb Collisions at* $\sqrt{S_{NN}} = 2.76\ TeV$. (2015). [arXiv:nucl-ex/1506.01689].

[56] T. Matsui, H. Satz. . Phys. Lett. B, **178**, 416, (1986).

[57] The ALICE Collaboration. *J/ψ suppression at forward rapidity in Pb-Pb Collisions at* $\sqrt{S_{NN}} = 2.76\ TeV$. (2012). [arXiv:nucl-ex/1202.1383].

[58] The ALICE Collaboration. *Centrality, rapidity and transverse momentum dependence of J/ψ suppression in Pb-Pb Collisions at* $\sqrt{S_{NN}} = 2.76\ TeV$. (2014). [arXiv:nucl-ex/1311.0214v3].

[59] The ALICE Collaboration. ***D*** *Meson Elliptic Flow in Noncentral Pb-Pb Collisions at* $\sqrt{s_{NN}} = 2.76\ TeV$. Phys. Rev. Lett., **111**, (2013), 102301.

[60] I. Belikov, *et al.* (ALICE Collaboration). *K^0_S and Λ production in Pb-Pb collisions with the ALICE experiment.* (2011). arXiv:hep-ex/1109.4807.

[61] M. Aggarwal, *et al.* (STAR Collaboration). *Strange and Multi-strange Particle Production in Au+Au Collisions at* $\sqrt{S_{NN}} = 64.4\ GeV$. *Phys. Rev. C*, **83**, 024901, (2011).

[62] Y. Oh, C. M. Ko, S. H. Lee and S. Yaushi. *Heavy baryon/meson ratios in relativistic heavy ion collisions. Phys. Rev. Lett.*, **100**, 222301, (2008).

[63] M. He, R. J. Fries and R. Rapp. *D_s-Meson as Quantitative Probe of Diffusion and Hadronization in Nuclear Collisions.* (2012). `arXiv:hep-ex/1204.4442`.

[64] The ALICE Collaboration. *Upgrade of the ALICE Experiment: Letter of Intent. J. Phys. G*, **41** 087001, (2012).

[65] E. V. Shuryak. *Quantum Chromodynamics and the theory of superdense matter. Phys. Rep.*, **61**(2): 71-158, (1980).

[66] The ALICE Collaboration. *The ALICE experiment at the CERN LHC. Jinst - Journal of Instrumentation*, **3** S08002, (2008).

[67] The ALICE Collaboration. *Alignment of the ALICE Inner Tracking System with cosmic-ray tracks. Jinst - Journal of Instrumentation*, **5** P03003, (2010). `[arXiv:physics.ins-det/1001.0502]`.

[68] The ALICE Collaboration. *Technical Design Report of the Inner Tracking System (ITS).* (1999). `[https://edms.cern.ch/file/398932]`.

[69] W. R. Leo. *Tecniques from Nuclear Particle Physics Experiment.* Ed. Springer, (1987).

[70] The ALICE Collaboration. *Technical Design Report of the Time Projection Chamber (TPC).* (2000). `[https://edms.cern.ch/file/451098]`.

[71] The ALICE Collaboration. *Performance of ALICE Experiment at the CERN LHC.* (2014). `[arXiv:nucl-ex/1402.4476v4]`.

[72] The ALICE Collaboration. *Technical Design Report of the Transition Radiation Detector (TRD).* (2000). `[https://edms.cern.ch/file/398057]`.

[73] The ALICE Collaboration. *Technical Design Report of the High Momentum Particle Identification Detector (HMPID).* (1998). [https://edms.cern.ch/document/316545/1].

[74] The ALICE Collaboration. *Technical Design Report of the PHOton Spectrometer.* (2003). [https://edms.cern.ch/document/398934/1].

[75] The ALICE Collaboration. *Technical Design Report of the ElectroMagnetic Calorimeter.* (1996). [http://aliweb.cern.ch/Documents/TDR/EMCAL.html].

[76] The ALICE Collaboration. *Technical Design Report of the Dimuon Spectrometer.* (1999). [https://edms.cern.ch/document/470838/1].

[77] The ALICE Collaboration. *Technical Design Report of the Zero Degree Calorimeter (ZDC).* (1999). [https://edms.cern.ch/document/398933].

[78] The ALICE Collaboration. *Technical Design Report of the Photon Multiplicity Detector.* (1999). [https://edms.cern.ch/document/398931/ and https://edms.cern.ch/document/575585/].

[79] The ALICE Collaboration. *Technical Design Report of Forward Detectors: FMD, T0 and V0.* (2004). [https://edms.cern.ch/document/498253/1].

[80] The ALICE Collaboration. *Technical Design Report of Trigger, Data Acquisition, High-Leve Trigger and Control System.* (2004). [https://edms.cern.ch/document/456354/].

[81] [http://aliceinfo.cern.ch/Public/en/Chapter2/Chap2_TOF.html].

[82] The ALICE Collaboration. *Technical Design Report of the Time Of Flight (TOF).* (2000). [http://cds.cern.ch/record/430132].

[83] The ALICE Collaboration. *Technical Design Report of the Upgrade of the ALICE Read-out & Trigger System.* (2013). [https://cds.cern.ch/record/1603472?ln=it].

[84] F. Anghinolfi, *et al.* CERN/EP - MIC. *IEEE Trans. On Nucl. Science.* **5**, (2004).

[85] J. Christiansen CERN/EP - MIC. *HPTDC - High Performance Time to Digital Converter.* (2004). [http://tdc.web.cern.ch/tdc/hptdc/hptdc.htm].

[86] VITA Standard Organization. *2eSST Source Synchronous Transfer. ANSI/VITA 01.5-2003*, **S2014**, (2003).

[87] The ALICE Collaboration. *Pseudorapidity and transverse-momentum distributions of charged particles in proton-proton collisions at* $\sqrt{s} = 13\ TeV$. (2015). [arXiv:nucl-ex/1509.08734].

[88] C. M. Grinstead, J. Laurie Snell. *Introduction to Probability.* American Mathematical Society, (1997).